

**DOT/FAA/AR-97/47**

Office of Aviation Research  
Washington, D.C. 20591

# **Development of Advanced Computational Models for Airport Pavement Design**



PB99-104473

August 1998

Final Report

This document is available to the U.S. public  
through the National Technical Information  
Service (NTIS), Springfield, Virginia 22161.




**U.S. Department of Transportation  
Federal Aviation Administration**

REPRODUCED BY: **NTIS**  
U.S. Department of Commerce  
National Technical Information Service  
Springfield, Virginia 22161

## **NOTICE**

This document is disseminated under the sponsorship of the U.S. Department of Transportation in the interest of information exchange. The United States Government assumes no liability for the contents or use thereof. The United States Government does not endorse products or manufacturers. Trade or manufacturer's names appear herein solely because they are considered essential to the objective of this report.

1. Report No. DOT/FAA/AR-97/47	2. ( )  PB99-104473	3. Recipient's Catalog No.	
4. Title and Subtitle  DEVELOPMENT OF ADVANCED COMPUTATIONAL MODELS FOR AIRPORT PAVEMENT DESIGN		5. Report Date August 1998	
		6. Performing Organization Code	
7. Author(s)  David R. Brill		8. Performing Organization Report No.	
9. Performing Organization Name and Address  Galaxy Scientific Corporation 2500 English Creek Ave., Bldg. 11 Egg Harbor Twp., NJ 08234-5562		10. Work Unit No. (TRAIS)	
		11. Contract or Grant No.  DTFA03-95-D-0019	
12. Sponsoring Agency Name and Address  U.S. Department of Transportation Federal Aviation Administration Office of Aviation Research Washington, DC 20591		13. Type of Report and Period Covered  Final Report	
		14. Sponsoring Agency Code  AAR-410	
15. Supplementary Notes  FAA William J. Hughes Technical Center COTR: Xiaogong Lee			
16. Abstract  A three-dimensional finite element model of a rigid airport pavement that employs public domain software was developed and tested. The model computes linear elastic stresses and displacements in concrete airport pavements that are loaded by multiple-wheel aircraft gears. Numerous rigid pavement features were incorporated in the model, including finite-size slabs, linear elastic joints, multiple pavement layers, and contact surface modeling of the slab/base layer interface. Complex aircraft gears are handled by representing the individual wheels as separate loads. A computer program was written to automatically generate the three-dimensional finite element mesh. Finite element solutions were computed on a UNIX workstation using the NIKE3D public domain computer program. Sample finite element results are presented for edge and interior loading for aircraft types including the Boeing B-727 aircraft. Finite element stress solutions were compared to field data and to critical stresses obtained using the current Federal Aviation Administration (FAA) methods as specified in Advisory Circular 150 rigid pavement (Westergaard-based) and Layered Elastic Design/Federal Aviation Administration (LEDFAA) (layered elastic-based) pavement design methods. In contrast to rigid pavement models based on the Westergaard theory, the three-dimensional finite element model permits realistic analysis of stress behavior near joints and in elastic layers underlying the rigid slab. Analysis of edge stress solutions obtained using the developed model shows the effect of a high-stiffness, continuous base layer in promoting load transfer at joints. The effect of a cracked base layer was also analyzed. An appendix to the report contains details of finite element test runs, including actual computation times.			
17. Key Words  Modeling, Finite element, Advanced pavement design, NIKE3D, Backcalculation		18. Distribution Statement  This document is available to the public through the National Technical Information Service (NTIS), Springfield, Virginia 22161.	
19. Security Classif. (of this report)  Unclassified	20. Security Classif. (of this page)  Unclassified	21. No. of Pages  89	22. Price



## TABLE OF CONTENTS

	Page
EXECUTIVE SUMMARY	ix
INTRODUCTION	1
Background	1
Objectives	2
Developing a Three-Dimensional Discretized Numerical Model for Rigid Airport Pavements	2
Sensitivity Analysis and Validation of Model Performance	2
Identification of Testing Requirements for Model Validation	3
DESCRIPTION OF THE FINITE ELEMENT MODEL	3
Technical Requirements for the Three-Dimensional Model	3
Explicit Modeling of Individual Gear Tire Loads	3
Static Loading	3
Multiple Slabs of Finite Size	3
Linear Elastic Joints (Shear Spring)	4
Discretized Multiple Support Layers	4
Representation of Infinite Subgrade Condition	5
Layer Interface Models	5
Public-Domain Software	5
Preliminary Three-Dimensional Finite Element Model	5
Finite Element Software	5
Element Types	6
Joint Models	7
Interface Models	10
Foundation/Subgrade Models	11
Linear Solvers	15
AUTOMATIC FINITE ELEMENT MESH GENERATION	16
Windows-Based Interactive Front End	18
Mesh Generation Using INGRID	20
Symmetry Considerations	20
Base and Subgrade Layer Mesh	20

Slab Layer Mesh	22
Modeling the Aircraft Gear Loads	24
Determination of the Nodal Loads	24
Tire Pressure Distribution	25
Controlling the Mesh Design	27
Nodal Merging	30
Model Scaling	31
Cracked-Base Option	31
Winkler Foundation Option	33
SAMPLE FINITE ELEMENT RESULTS	34
Analysis of B-777 Edge Loading	34
Analysis of B-727 Edge Loading	40
Analysis of B-777 Interior Loading	42
MODEL SENSITIVITY ANALYSIS	43
Identification of Variables for Sensitivity Analysis	43
Benchmark Response for Analysis	44
Effect of Fine Mesh Density	45
Effect of Subgrade Cutoff Depth	45
Effect of Boundary Nodal Constraints	47
Joint Stiffness and Joint Efficiency	48
Effect of Base Layer	49
Test Runs Using B-777 Load	50
Test Runs Using B-727 Load	53
Effect of Load Geometry	55
MODEL VALIDATION	55
Validation by Comparison to Other Computational Methods	55
Model Validation With Instrumented Runway Data	57
Peak Strain Comparisons	58
Strain Distribution Comparisons	62
Slab Deflection Comparisons	63
Model Validation With Full-Scale Airport Pavement Test Machine	65

SUMMARY AND CONCLUSION	67
------------------------	----

REFERENCES	69
------------	----

## APPENDICES

- A–Summary of Test Run Data
- B–Formulas for Lobatto Integration
- C–Constants for NIKE3D Material Type 17
- D–NIKE3D Control Card Settings

## LIST OF FIGURES

Figure		Page
1	Arrangement of Slabs in Nine Slab Systems	4
2	Idealized Linear Joint	7
3	Preliminary Joint Model Using Discrete Beam Elements	8
4	Final Joint Model Using Orthotropic Solid Elements	9
5	Finite Element/Boundary Element Hybrid Model	12
6	Discretized Model for Run Time Estimates	13
7	Main Window Display for PreGrid	18
8	Pavement Structure Edit Window for PreGrid	19
9	Three-Dimensional Mesh for Base and Subgrade Layers (Edge Load Case)	21
10	Three-Dimensional Mesh for Base and Subgrade Layers (Interior Load Case)	22
11	Two-Dimensional Mesh for Slab Layer (Edge Load Case)	23
12	Detail of Slab Mesh With B-777 Main Gear Load	23
13	Nodal Load Distribution by Tributary Area Method	25
14	Nonuniform Tire Contact Pressure Distribution	26

15	Control Dimensions for Slab Mesh (Edge Load)	28
16	Detail of Invalid Slab Mesh Resulting From Incorrectly Chosen Parameters	29
17	Flowchart for Computing Control Dimensions in Automatic Mesh Generation Program (Edge Load)	30
18	Crack Location for Cracked-Base Model	32
19	Nodal Arrangement for Cracked-Base Option	32
20	Schematic of Winkler Foundation Showing (a) Foundation Nodes and Springs and (b) Nodal Tributary Area	33
21	Vertical Deflection of PCC Slab (B-777 Edge Load)	36
22	Principal Bending Stress in Bottom of PCC Slab (B-777 Edge Load)	37
23	Principal Strain in Bottom of PCC Slab (B-777 Edge Load)	38
24	Vertical Stress in Top of Subgrade Layer (B-777 Edge Load)	38
25	Slab-Base Separation at Joint (B-777 Edge Load)	39
26	Vertical Deflection of PCC Slab (B-727 Edge Load)	41
27	Principal Bending Stress in Bottom of PCC Slab (B-727 Edge Load)	41
28	Vertical Deflection of PCC Slab (B-777 Interior Load)	42
29	Principal Bending Stress in Bottom of PCC Slab (B-777 Interior Load)	43
30	Computed Critical Stress (Normalized) as a Function of Subgrade Cutoff Depth	46
31	Boundary Constraints for Test Problem (Edge Load Case)	48
32	Effect of Stabilized Base on Critical Stress in PCC Slab (B-777 Edge Load)	50
33	Effect of Stabilized Base on the Ratio of Maximum Stress in the Unloaded Slab to Maximum Stress in the Loaded Slab (B-777 Edge Load)	51
34	Effect of Stabilized Base on the Ratio of Maximum Deflection of the Unloaded Slab to Maximum Deflection of the Loaded Slab (B-777 Edge Load)	51
35	Effect of Stabilized Base on Percent of Load Transfer (B-777 Edge Load)	52



36	Comparison of Stress Distributions Along Slab Edge for Cracked and Continuous Base Layers (B-777 Loading)	53
37	Effect of Base Layer Cracking on Critical Stress in PCC Slab (DIA Test Runway, B-727 Load)	54
38	Effect of Base Layer Cracking on Percent of Load Transfer (DIA Test Runway, B-727 Load)	54
39	Strain Gauge Layout at DIA Test Runway	60
40	Denver International Airport Test Runway—Contours of Computed Strain in PCC Slab at 1-Inch Embedment Depth (B-777 Edge Load)	61
41	Distribution of Strain as Computed by Finite Element Model and as Recorded at Strain Gauge HB08 (B-777 Edge Load)	62
42	Distribution of Strain as Computed by Three-Dimensional Finite Element Model and as Recorded at Strain Gauge HB58 (B-777 Edge Load)	63
43	Single- and Multiple-Depth Deflectometer Locations at DIA Test Runway	64
44	Denver International Airport Test Pavement—Recorded Slab Deflections on Opposite Sides of a Transverse Joint (B-727 Load)	65

## LIST OF TABLES

Table	Page
1 Comparison of Operation Counts and Estimated CPU Times for Various Modeling Strategies	14
2 Effect of Nonuniform Tire Pressure Distribution and Load Patch Shape on Finite Element Computed Critical Stress for B-737 Single-Wheel Load	27
3 Layer Properties for B-777 and B-727 Edge Load Analyses	34
4 Load Data for Sample Finite Element Analyses	34
5 Mesh Data for B-777 Edge Load Problem	35
6 Summary of Results of Finite Element Analysis (B-777 Edge Load)	39
7 Mesh Data for B-727 Edge Load Problem	40
8 Summary of Results of Finite Element Analysis (B-727 Edge Load)	40
9 Mesh Data for B-777 Interior Load Problem	42
10 Summary of Results of Finite Element Analysis (B-777 Interior Load)	43
11 Variables Affecting Model Response	44
12 Effect of Finite Element Mesh Density (Slab Mesh)	45
13 Properties for Test Series in Figure 30	46
14 Edge Constraint Comparison	48
15 Effect of Joint Stiffness $k_{joint}$ on Computed Response	49
16 Computed Responses for Various Aircraft Loads	55
17 Comparison of Analysis Methods	56
18 Equivalent Modulus of Subgrade Reaction	57
19 Denver International Airport Test Runway—Properties for Finite Element Analysis	58
20 Denver International Airport Test Runway—Strain Due to Aircraft Load as Recorded In Situ and as Predicted by the Three-Dimensional Finite Element Model	61
21 Slab Deflections as Measured by LVDT Gauges and as Predicted by the Three-Dimensional Finite Element Model	65
22 Airport Pavement Test Machine Input Data for Three-Dimensional Model Validation	66

## EXECUTIVE SUMMARY

The recent introduction of the Boeing B-777 aircraft, and the planned development of even larger aircraft, will have significant effects on the nation's airport infrastructure. The Federal Aviation Administration (FAA) has undertaken a multiyear research effort aimed at developing new computer-based models for airport pavement design. Crucial to this effort is the development of a three-dimensional (3D) finite element model that is capable of accurately determining stresses in rigid pavements caused by aircraft with multiple-wheel landing gear configurations.

This report describes the development of a 3D pavement model using the finite element program NIKE3D. Some important features of the model described herein are:

- Explicit modeling of multiple-wheel aircraft gears
- Finite element representation of finite-size slabs
- Finite element representation of multiple structural layers and layer interfaces
- Incorporation of linear elastic joint model
- Rapid, automatic generation of three-dimensional finite element meshes. The procedure for computer-based mesh generation is described in detail.

The developed 3D model is capable of capturing special features of rigid airport pavements including slab sizes, joints, stabilized-base layer, and the interface effects between Portland cement concrete (PCC) slabs and base courses. The potentials of utilizing the 3D finite element method (FEM) to develop better design procedures for rigid airport pavements are well demonstrated.

A sensitivity analysis was performed to establish minimum values of model parameters such as mesh density and overall model dimensions. The results of the sensitivity analysis are discussed.

Examples are provided of rigid pavements analyzed using the developed finite element model. The sample finite element results include edge and interior aircraft loads. Model results are validated by comparison with other analysis methods, including the FAA Advisory Circular (AC) 150 design method for rigid pavements and Layered Elastic Design/Federal Aviation Administration (LEDFAA). In addition, some comparisons to field data from the Denver International Airport (DIA) Instrumented Pavement Project are included.

The report includes recommendations for further development of the 3D finite element model. It is suggested that efforts should be made to reduce run times by improving computational efficiency. It is also recommended that more validation of the finite element model be performed using field data from DIA and data from the full-scale National Airport Pavement Test Machine (NAPTM) currently under construction at the William J. Hughes Technical Center, Atlantic City International Airport, New Jersey.



## INTRODUCTION

As part of its ongoing effort to advance the state of the art in airport pavement design, the Federal Aviation Administration (FAA) began development of a new, three-dimensional discretized model for computing rigid pavement responses to aircraft loading. The specific requirements for the rigid pavement model are that it explicitly models the interactions caused by individual tires of multiple-wheel aircraft landing gears; that it incorporates multiple slabs of finite size; that it makes use of available public-domain software; and that it be adaptable to future advancements in joint, interface, and material models.

A three-dimensional finite element model meeting the above criteria was developed and implemented. Numerical computations are performed using the finite element program NIKE3D on a UNIX workstation platform. Finite element meshes for rigid pavements are generated automatically using a user-friendly mesh generation program that incorporates the public-domain program INGRID as a preprocessor.

This report covers the development, implementation, and testing of the three-dimensional finite element model for rigid pavements. The report is organized as follows: The first section covers the development of a preliminary numerical model and describes the various components that were included in the final model. The second section describes the computer program for mesh generation and presents examples of computer-generated meshes. In the third section, several examples of rigid pavement analyses using the three-dimensional finite element model are presented. Three-dimensional plots of stress and deflection caused by aircraft static loads are shown. The fourth section discusses the model sensitivity analysis and validation of the finite element model by comparison with other computational methods and with available field data. The last section highlights conclusions and recommends areas for possible further development. The work described in this report took place over a 20-month period between September 1995 and May 1997.

## BACKGROUND.

The recent introduction into commercial service of the Boeing B-777 aircraft has highlighted the need for new advanced design methods for airport pavements using advanced computer technology. As aircraft landing gears continue to get heavier and more complex, it has become increasingly clear that the traditional design models well known to pavement engineers are oversimplified and inadequate to assess the effect of the new aircraft designs on the nation's airport infrastructure. For rigid pavements, the problem is especially acute. The current FAA design standards for rigid airport pavements, as encompassed in FAA Advisory Circular (AC) 150/5320-6D, are largely based on a classical theoretical model (the Westergaard model) that fails to account for such factors as slab size and that characterizes the entire multilayer pavement structure below the slab by a single parameter (the modulus of subgrade reaction).

Rigid pavements are fundamentally different from flexible pavements in several ways. Unlike flexible pavements, rigid pavements are typically assemblages of jointed slabs, with various types of load transfer devices used to transmit loads from one slab to another. Because stresses occurring at the edges of rigid slabs are usually the critical stresses for design, the slab edges and

joints must be considered in any analytic model of rigid pavements. Slab size and joint spacing may also influence the pavement response to loads. Another important difference is that in rigid pavement slabs, the bending stresses dominate the response to loading to a significantly greater degree than in flexible pavement layers due to the higher stiffness of Portland cement concrete (PCC) materials relative to asphalt materials.

Flexible pavements can often be idealized as closed systems consisting of several linear elastic layers, with each layer both uniform in thickness and infinite in horizontal extent. This layered elastic approach to pavement modeling is unsuitable for rigid systems because it ignores the joint discontinuities. For rigid pavements, the three-dimensional finite element approach is superior since slabs of finite extent can be modeled, as well as joints, cracks, gaps, and other discontinuities. In addition, the finite element method frees the analysis from the restriction to linear elastic, isotropic material models that characterize the layered elastic theory. Currently, the biggest drawback to the three-dimensional finite element approach is that it is very time consuming. The solution to a single problem may require on the order of tens of hours of computer time. The time required for a finite element solution can be divided into two categories: model preparation and model execution. In the past, the model preparation phase (including mesh construction) accounted for a significant part of the total solution effort. However, with automated mesh generation algorithms, the preparation phase of the solution is no longer a significant time consideration. On the other hand, the numerical solution of large systems of finite element equations is still a time consuming process and will likely remain so pending major advances in computer processor technology.

## OBJECTIVES.

The project objectives were divided into three parts: development of the model, sensitivity analysis and model validation, and identification of testing requirements. The specific objectives of each part were as follows.

DEVELOPING A THREE-DIMENSIONAL DISCRETIZED NUMERICAL MODEL FOR RIGID AIRPORT PAVEMENTS. The main objective of this part of the project was to specify, implement, and test a discretized computational model for computing the response of rigid airport pavements to arbitrarily configured aircraft gears. The model should represent the correct stress behavior of rigid pavements subjected to loads from multiple-wheel aircraft gears and should be able to accommodate different types of rigid pavement construction, including stabilized bases. In order to achieve this objective it was necessary to consider the wide range of numerical analysis techniques available. A secondary objective related to the model specification was to design and implement a procedure for rapid, automatic generation of the discretized meshes required for the numerical model.

SENSITIVITY ANALYSIS AND VALIDATION OF MODEL PERFORMANCE. The objective of the sensitivity analysis was to identify variables affecting the finite element model response and to quantify the sensitivity of the critical model response to the different variables. Data collected in the sensitivity analysis will be used to further refine the model in future implementations. A second objective was to obtain numerical solutions using the developed

finite element model and to compare the finite element solutions to results obtained using standard FAA methodologies.

IDENTIFICATION OF TESTING REQUIREMENTS FOR MODEL VALIDATION. It is expected that model predictions will be compared to results of future response tests conducted at the National Airport Pavement Test Machine which is currently under construction at the William J. Hughes Technical Center. The last objective of the project was to identify test requirements to validate the finite element model. These requirements include installation of sensors at various locations in the test pavement to record pavement responses and performance of tests for characterization of pavement materials in the finite element model.

## DESCRIPTION OF THE FINITE ELEMENT MODEL

### TECHNICAL REQUIREMENTS FOR THE THREE-DIMENSIONAL MODEL.

Development of the three-dimensional computational model was guided by a set of technical requirements, all of which were met in the final model. A short description of each requirement and the reasons for its inclusion follows.

EXPLICIT MODELING OF INDIVIDUAL GEAR TIRE LOADS. One of the advantages of a true three-dimensional finite element model is that problems involving multiple loads and complex gear configurations are no more difficult to solve than those involving single loads. Therefore the equivalent single wheel concept has no particular advantage in the finite element method. By representing the tire loads individually and in their correct geometric relation, rather than lumping them together in an equivalent single load, it becomes possible to use the model to explore the tire interactions at various levels and locations within the structure. The ability to represent tire interactions was an explicit motivation for the development of a three-dimensional discretized model.

While the tires comprising the gear truck were modeled separately, the individual tire loads were assumed to be distributed uniformly on a rectangular load patch. Nonuniform pressure distributions and nonrectangular load patches were considered at the preliminary stage but were not used in the final model because preliminary studies indicated that the variation in the computed response due to these factors was negligible and did not justify the extra effort involved in defining the loads.

STATIC LOADING. The model considers static rather than dynamic loading since the maximum static response is normally used as the basis for design. For a particular aircraft, the static load is the maximum load transmitted to the pavement by the main gear under stationary conditions. For most aircraft types the maximum stresses occur when the gear acts at the slab edge (edge loading). However, for the twin-tridem B-777 main gear the interior load case may be more severe than the edge load case under certain conditions. For this reason, the model was designed from the outset for either edge loading or interior loading (see figure 1).

MULTIPLE SLABS OF FINITE SIZE. One of the objectives was to be able to model finite-size slabs and vary load transfer properties between adjacent slabs. For the preliminary model, 25 by

25 feet was chosen as a typical slab size for airport pavements. Nine slabs were arranged as shown in figure 1 to accommodate either edge loading or interior loading on the center slab.

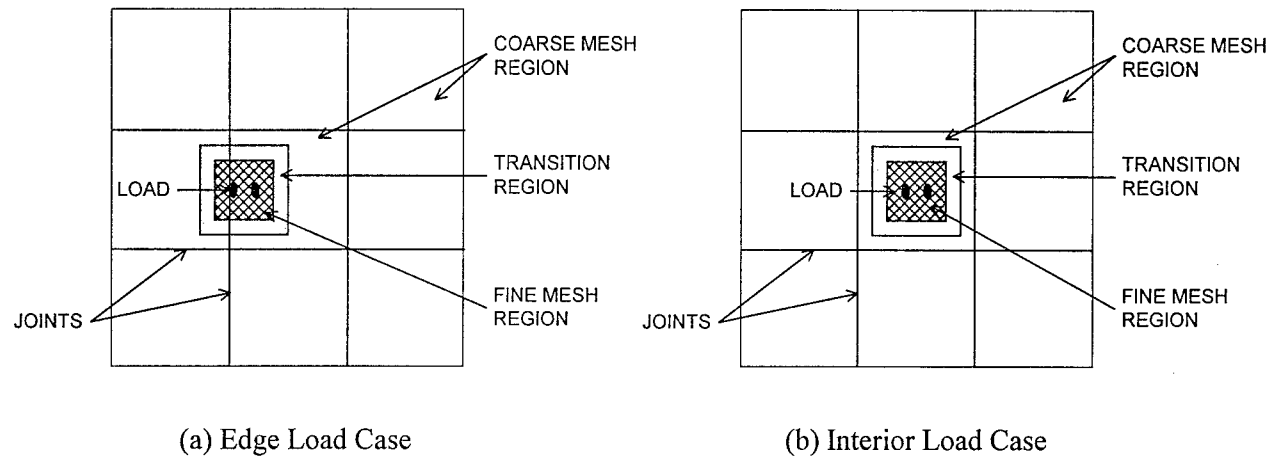


FIGURE 1. ARRANGEMENT OF SLABS IN NINE SLAB SYSTEMS

LINEAR ELASTIC JOINTS (SHEAR SPRING). In real pavements, loads are transferred across joints by means of dowels, keys, tie rods, or other load transfer devices. While the finite element method can be used to create detailed models of specific load transfer mechanisms, the development of advanced models for particular joint types was not within the scope of the current project. Hence, no attempt was made to model individual dowels or other load transfer devices explicitly. Instead, a simplified linear model was used that is broadly applicable to the range of load transfer devices used in practice.

The simplified model of joint behavior used in the finite element model assumes that the joints act as linear elastic springs, transmitting vertical loads between adjacent slabs in shear through the joint. The shear force is assumed linearly proportional to the relative vertical displacement between slabs (Hooke's law). The joint is characterized by an equivalent shear stiffness  $k_{joint}$ , expressed in units of force per relative vertical displacement per unit length of the joint. No moment stiffness is assigned to the joint, consistent with the widely accepted view that joints transfer loads primarily in shear and that the contribution of moment transfer is relatively small.

DISCRETIZED MULTIPLE SUPPORT LAYERS. Base and subbase layers for rigid pavements may be of various stiffnesses, either stabilized or unstabilized, and may resist loads in shear, bending, and vertical compression. To represent the correct stress behavior of different types of support layers, including stabilized base layers, it was essential that the model include full discretization of (at a minimum) the base and subbase layers. Full or partial discretization of the subgrade layer was also considered desirable. The final model was implemented with full discretization of base and subgrade layers, but with an option to substitute a spring foundation for the discretized subgrade layer.



REPRESENTATION OF INFINITE SUBGRADE CONDITION. Typical design procedures for rigid airport pavements assume an infinite depth of subgrade. While it is possible to use infinite elements to model an unbounded domain in the finite element method, more commonly an artificial boundary is imposed on the computational domain. The artificial boundary, or fixed base, is located at a depth so that the solution does not differ too much from the solution for the original (infinite) problem. In practice, the location of the fixed base is a matter of judgment.

LAYER INTERFACE MODELS. Horizontal interfaces in the three-dimensional model meet the requirements of a full unbonded interface between the slab and base course and a full bond at all other horizontal interfaces. No attempt was made to implement advanced interface models, such as partial bond or friction models, in the current model.

The standard of a fully (100%) unbonded interface between the concrete slab and the base layer and 100% bond at the other horizontal interfaces is based on Parker et al. [1] In addition to satisfying this requirement, the model includes partial layer separation between the slab and base course.

PUBLIC-DOMAIN SOFTWARE. The model incorporates existing software to perform numerical calculations. Existing programs in the public domain were strongly preferred over commercial programs for inclusion in the model. A major consideration that led to the requirement for public software was the need to have access to the source code during model development.

#### PRELIMINARY THREE-DIMENSIONAL FINITE ELEMENT MODEL.

The first stage of the work involved specification of a preliminary finite element model primarily for testing and evaluation of the various model components and numerical options. In this stage, potential model components and options were evaluated in terms of their effect on the overall speed and efficiency of the model operation and on the consistency of the predicted response. Based on the conclusions of the preliminary analysis, components were either included or not included in the final model.

#### FINITE ELEMENT SOFTWARE.

The finite element method was chosen as the basis of the discretized model because of its versatility, proven reliability, and the availability of tested, public-domain software. The finite element package used for the computations was the package of public-domain codes developed by the Lawrence Livermore National Laboratories, which includes the codes DYNA3D, NIKE3D, and INGRID. DYNA3D is a general finite element code based on explicit time integration intended for solving highly dynamic structural problems such as those involving explosions or impacts or wave propagation. The companion program, NIKE3D, is a finite element code based on implicit time integration and suitable for either dynamic or quasi-static structural analysis. [2] For the problem of rigid pavements under quasi-static loading, it was evident that NIKE3D is the more suitable program, so it was adopted as the computational engine for the preliminary model.

INGRID, [3] the preprocessor program, is a companion program to NIKE3D and DYNA3D. It generates a three-dimensional mesh and input file for NIKE3D. In order to use INGRID, it is necessary to write an instruction file in a unique programming code. To eliminate the necessity for the user to learn the INGRID code, a front-end computer program was developed for INGRID. Automatic mesh generation procedures will be discussed in the following section.

For handling contact, the NIKE3D code has a library of interface models including tied surfaces, sliding surfaces with separation prevented, and sliding surfaces with gap formation allowed. The sliding surfaces are based on a penalty formulation. The principal disadvantage of NIKE3D as a code is its limited library of element types. NIKE3D supports just three element types: 8-node solid (hexahedron) elements, 4-node shell elements, and 2-node beam elements. Consequently, all finite element models submitted to NIKE3D for solution must contain only these three types of elements. This difficulty was overcome in the final model, which uses 4-node shell and 8-node solid elements only.

### ELEMENT TYPES.

Two-dimensional shell elements are used to represent the slab layer and three-dimensional solid elements (hexahedrons) for all other layers. Hexahedral elements in NIKE3D have eight nodes, located at the element corners. Element stresses are computed at the  $2 \times 2 \times 2$  Gauss integration points. The numerical integration scheme for solid elements in NIKE3D is fixed and cannot be changed by the user. Shell elements have four nodes located at the corners. Similar to solid elements, numerical integration in the plane of the shell is based on a Gauss  $2 \times 2$  integration scheme that cannot be user modified. However, integration through the shell thickness can be controlled by the user at the input level. A five point Lobatto integration scheme (see appendix B) was substituted for the default two point Gauss scheme, enabling the program to compute the stresses directly at the upper and lower surfaces of the shell. For concrete slab analysis the computed stresses at the top and bottom surfaces are of greatest interest since these represent the extreme fiber stresses in the slab.

The ability to compute stresses directly at the surface, rather than extrapolate to the surface from an interior integration point, is a clear advantage of using NIKE3D shell elements to represent the slab. Another advantage is that, compared to hexahedral elements, fewer elements are needed to model the slab. This is because a single layer of shell elements is able to represent the bending behavior of the slab while a reasonable approximation of bending using the NIKE3D hexahedral elements requires a minimum of four layers.

A third advantage of shell elements over hexahedral elements is tied to geometric considerations in the slab. Good mesh design requires that aspect ratios of the finite elements be controlled. In the case of hexahedral elements, horizontal dimensions should not greatly exceed vertical dimensions, and thin, platelike elements should be avoided if possible. Given a slab of thickness  $t$ , the slab should be divided into  $n$  layers of hexahedrons such that the height of the hexahedral element is  $t/n$ . In order to preserve a reasonable aspect ratio, the horizontal side of hexahedral elements throughout the slab mesh should be limited to some multiple of the slab thickness, say  $6t/n$ . This restriction results in excessively dense meshes away from the load, increasing the

element count beyond what considerations of engineering accuracy alone would require. The same restriction does not apply in the case of shell elements. Since shell elements are two-dimensional, the ratio of element side to shell thickness can be as large or small as required. This property of shell elements permits a good deal more flexibility in meshing.

One-dimensional beam elements were used in connection with the first joint model developed (see Joint Models).

### JOINT MODELS.

Joint modeling presents special difficulties in NIKE3D. The ideal spring connection, as shown in figure 2, would be one that provides a vertical spring force proportional to the relative vertical displacement between adjacent slab edges but does not constrain movement in any other direction. Unfortunately, NIKE3D does not support such a spring connection.

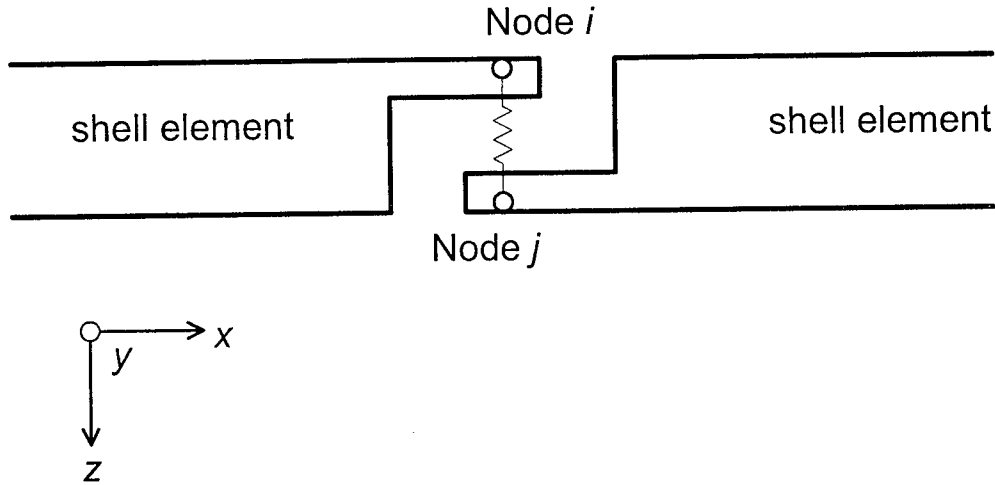


FIGURE 2. IDEALIZED LINEAR JOINT

The preliminary model used short NIKE3D beam elements to approximate a shear spring connection. A schematic of this model is shown in figure 3. It should be emphasized that, although beam elements were used, the intention of the preliminary was not to model the joint as a beam mechanism nor to model the individual dowel bars. Consequently, the spacing of the beam elements shown in figure 3 does not correspond to the actual spacing of dowel bars nor does the short span length  $\delta$  correspond to the actual gap between pavement slabs.

In figure 3, nodes  $j$  and  $k$  are constrained to act together in both the  $y$  and  $z$  directions while relative horizontal motion in the  $x$  direction is unconstrained. Relative rotational movement is also permitted in all directions. From elementary mechanics, the relative displacement  $\Delta z$  induces a shear force  $V$  in the beam, as well as a moment  $M$  at node  $i$ . For the statically determinate beam, the induced moment is given by

$$M = V\delta$$

Since the beam span length  $\delta$  does not correspond to an actual gap width, it can be made arbitrarily small. It should be chosen small enough to make the value of  $M$  negligible. In the preliminary model a value of 0.1 inch was used for  $\delta$ . For the shear beam, the equivalent stiffness of joint per unit length of joint is given by

$$k_{joint} = \frac{5EI}{(1 + \mu)\delta h^2}$$

where  $h$  is the height of the beam element and  $\mu$  is Poisson's ratio for the beam material. The required beam stiffness  $EI$  (per unit length of joint) is calculated for the individual beam element from the assumed value of  $k_{joint}$ .

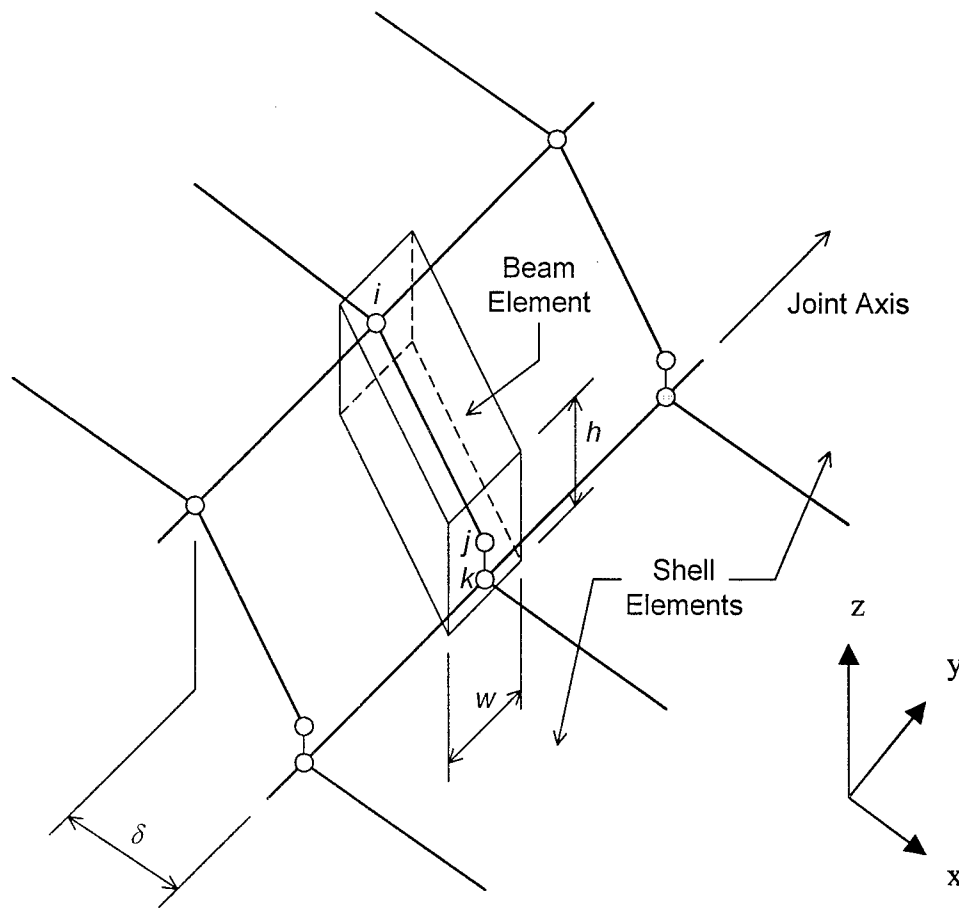


FIGURE 3. PRELIMINARY JOINT MODEL USING DISCRETE BEAM ELEMENTS

After the preliminary finite element model was developed, it was discovered that the beam elements in the above joint model are not compatible with the preconditioned conjugate gradient (PCG) solver in NIKE3D (see Linear Solvers). In order to make use of the PCG option, a joint model with 3D elements was developed (figure 4) and implemented in the final model. The final joint model uses three-dimensional solid elements with linear elastic, orthotropic material properties. As opposed to the previous model where discrete beam elements were placed at the nodes, here the solid elements form a continuous joint.

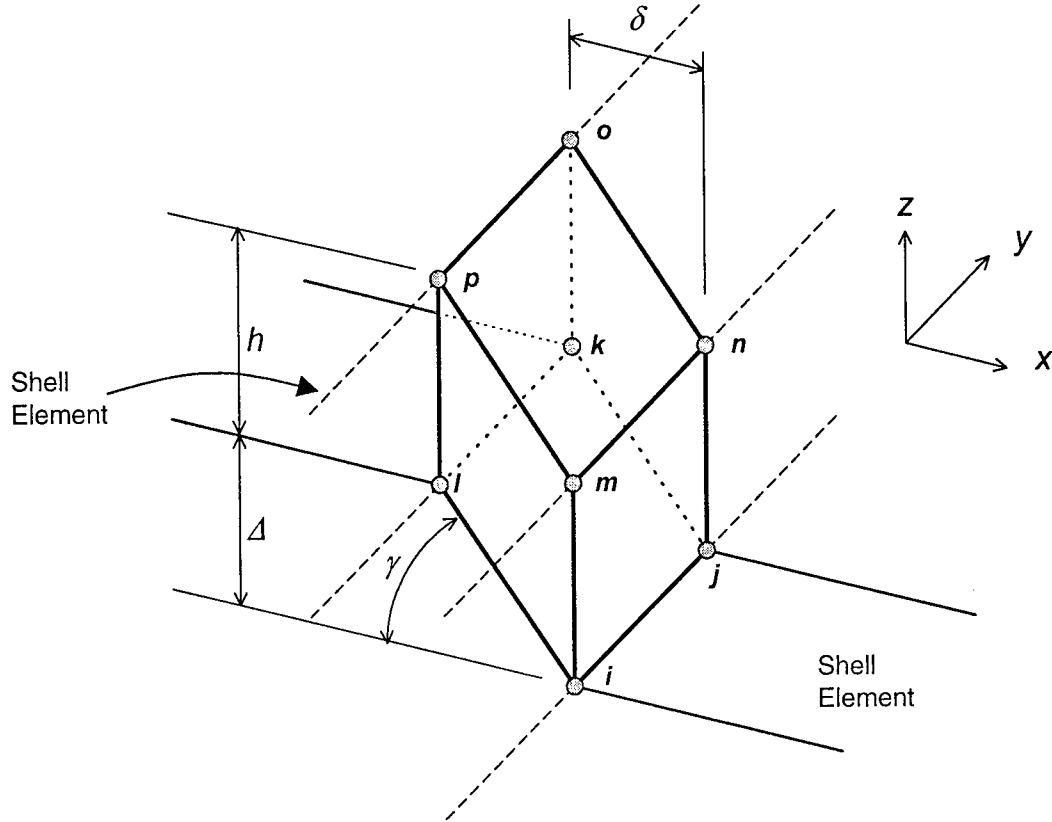


FIGURE 4. FINAL JOINT MODEL USING ORTHOTROPIC SOLID ELEMENTS

Orthotropic materials have different elastic properties in orthogonal directions. Stress-strain behavior is defined in the material model by nine independent elastic constants: Young's moduli  $E_X$ ,  $E_Y$ ,  $E_Z$ ; shear moduli  $G_{XY}$ ,  $G_{YZ}$ ,  $G_{ZX}$ ; and Poisson's ratios  $\mu_{XY}$ ,  $\mu_{YZ}$ ,  $\mu_{ZX}$ . The subscripts  $X$ ,  $Y$ , and  $Z$  refer to local coordinate axes that may or may not correspond to the global axes  $x$ ,  $y$ , and  $z$ . In NIKE3D, orthotropic elastic solids correspond to material type no. 2.

In figure 4, the joint is parallel to the  $y$  axis, so the local axes are taken to coincide with the global axes. A shear modulus  $G_{xz}$  for the joint element can be calculated from the assumed joint stiffness  $k_{joint}$ . The shear modulus is defined as the ratio of shear stress  $\sigma_{xz}$  to shear strain  $\gamma_{xz}$  where the shear strain  $\gamma_{xz}$  in figure 4 can be calculated as the angle defined by the relative

displacement  $\Delta$  divided by the element length  $\delta$ . The shear stress  $\sigma_{xz}$  in the element can be related to the joint shear stiffness per unit length by

$$\sigma_{xz} = k_{joint} \frac{\Delta}{h}$$

where  $h$  is the element height. Using the definition of shear modulus gives

$$G_{xz} = \frac{\sigma_{xz}}{\gamma_{xz}} = \frac{k_{joint} \delta}{h}.$$

As with the beam model, the joint element side length  $\delta$  does not correspond to the actual gap between the slabs, so it can take on any convenient value. It is most convenient to assign the same numerical value to  $\delta$  and  $h$  so that  $G_{xz}$  has the same numerical value as  $k_{joint}$ . All of the numerical examples in this report were computed using the values  $h = \delta = 1.0$  in. The 1-inch dimension was chosen to provide a suitable aspect ratio for the 3D solid joint elements. While a smaller dimension, say  $\delta = 0.1$  in., may be closer to a realistic estimate of the gap width, it was found that the resulting high aspect ratio leads to numerical problems in the finite element solution. In particular, the stresses computed using  $\delta = 0.1$  in. do not differ significantly from those computed using 1.0 in., but due to the thinness of the joint elements, the required solution time is much longer (cf. runs no. 9 and 63 in appendix A for a comparison of run times).

The other elastic constants were assigned appropriate values. In particular,  $E_x$  was assigned a low nominal value ( $E_x = 100$  psi) to allow independent horizontal movement of the slabs on opposite sides of the joint. Poisson's ratio was 0.3 in all directions.

The nodes in the upper layer that are not connected to the shell elements must be constrained to prevent rotation of the joint elements and to force the joint elements to deform in shear, as shown in figure 4. This is accomplished in the model by constraining node  $m$  to have the same vertical and horizontal displacements as node  $i$ , and similar constraints are applied to the node pairs  $(j, n)$ ,  $(k, o)$ , and  $(l, p)$ .

## INTERFACE MODELS.

Horizontal interfaces that were completely bonded required no special treatment in the finite element method. For other interfaces, in particular for the interface between the bottom of the slab and the top of the base layer, NIKE3D provides a number of built-in options. The available interface models are:

Type 1 - Tied. No separation or sliding is permitted. (This option is practically equivalent to a completely bonded interface, but allows the mesh to be discontinuous across the interface. It was not used in the current model.)

Type 2 - Sliding only. Allows frictionless sliding of contact surfaces with full contact maintained between surfaces.

Type 3 - Sliding with gaps (see below).

The last option, sliding with gaps (Type 3), is the general contact option available within NIKE3D. Designated slide surfaces may be in contact or fully or partially separated. The final contact surface is obtained by equilibrium iterations and does not have to be known *a priori*. This option is particularly useful for modeling gap formation in rigid pavements where surfaces initially in contact may become partially separated under the application of load. As with Type 1 and Type 2 interfaces, the mesh can be discontinuous across the interface.

For rigid pavements in edge loading, it is common for the slab on the unloaded side of the joint to become separated from the base layer. This condition is modeled by defining the interface between slab and base as a Type 3 slide surface (sliding with gaps).

Another feature of Type 3 sliding surfaces in NIKE3D is the ability to treat sliding friction. It is possible to designate both static and kinetic friction coefficients applicable to the whole slide surface. These options were not used in the current model due to the static nature of loading and because to include friction would be to depart from elastic theory.

All of the NIKE3D contact models are based on a penalty formulation. This means that in all problems involving contact, a small but finite amount of penetration between the contacting surfaces must occur in order to develop the penalty forces. In NIKE3D it is possible to control the degree of penetration by adjusting the “penalty stiffness scale factor” for penalty forces, although penetration can never be reduced to zero. In NIKE3D the default value of the penalty stiffness scale factor is 1.0. From repeated trials of the pavement models it was found that NIKE3D’s default settings led to excessive penetration at the slab-base interface, and a factor of 10.0 was needed to reduce the penetrations to acceptably low values. The cost associated with increasing the penalty stiffness scale factor is slower convergence of the numerical solution.

#### FOUNDATION/SUBGRADE MODELS.

The numerical options available to model the infinite subgrade were analyzed. The following alternatives were identified and studied:

1. Artificial fixed base. In this option the subgrade is discretized using finite elements to an arbitrary cutoff depth. The contribution of the subgrade below the cutoff depth is ignored.
2. Compliant foundation. The discretized subgrade is replaced by a compliant mat foundation. The base layer of nodes is not fixed but is assigned a stiffness based on the theoretical response of a dense liquid (Winkler foundation) or a semi-infinite elastic solid (Boussinesq foundation). The three-dimensional discretization of the base and subbase layers is retained.
3. Infinite elements. Infinite elements are special finite elements that are extended to infinity in one or more directions by using nonlinear shape functions whose value decays

to zero at infinity. Because they do not increase the node count, but simply contribute an additional stiffness to nodes at the base, infinite elements may actually be thought of as a kind of compliant foundation.

4. Finite element/boundary element hybrid model. By coupling boundary elements to standard finite elements it is possible to produce a numerical model encompassing the entire subgrade region. A schematic of such a hybrid model is shown in figure 5. The model in figure 5 is based on a special boundary element formulation (the Mindlin formulation) for which the fundamental solutions are the solutions for a linear elastic half space. [4] The advantage of a hybrid technique is that a relatively small region is discretized, yielding substantially fewer equations than a comparable finite element mesh. In figure 5, only the slab and base layers are discretized. Also, the boundary region, which is not discretized, automatically accounts for the infinite extent of the problem domain. A major disadvantage is a lack of qualified public-domain software to handle boundary element or hybrid problems.

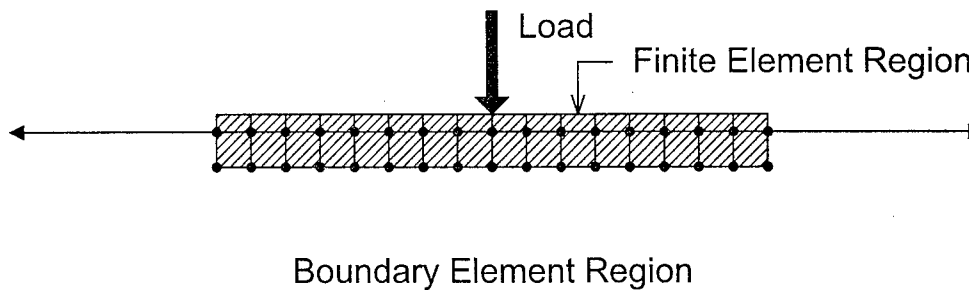


FIGURE 5. FINITE ELEMENT/BOUNDARY ELEMENT HYBRID MODEL

The comparison consisted of three steps. First, node and element counts were made based on a hypothetical model of a rigid pavement consisting of nine slabs and a base layer supported on an infinite subgrade. For simplicity, joints and sliding interface elements were not considered in the calculations, nor were equilibrium iterations considered. Next, estimates were made of the total number of mathematical operations (additions, multiplications, root extractions) required to completely solve the linear system produced by each of the above alternatives using a direct method of solution. Finally, these estimated operations counts were converted to estimated run times on a work station computer. Because all of the steps were done on paper, there was no need to actually implement the various models and time them.

The hypothetical model used for the comparison is shown in figure 6. The slab layer consists of 1,940 4-node shell elements for a total of 2,137 nodes. The base layer consists of a single layer of 8-node solid elements for a total of 900 solid elements and 1,922 nodes. For the artificial fixed base option, a discretized subgrade consisting of 10 layers of solid elements in a regular mesh was used. The total number of additional elements in the discretized subgrade is 9,000 and



the total number of additional nodes is 9,610. The option of using higher order, 20-node serendipity elements for the discretized subgrade was also considered.

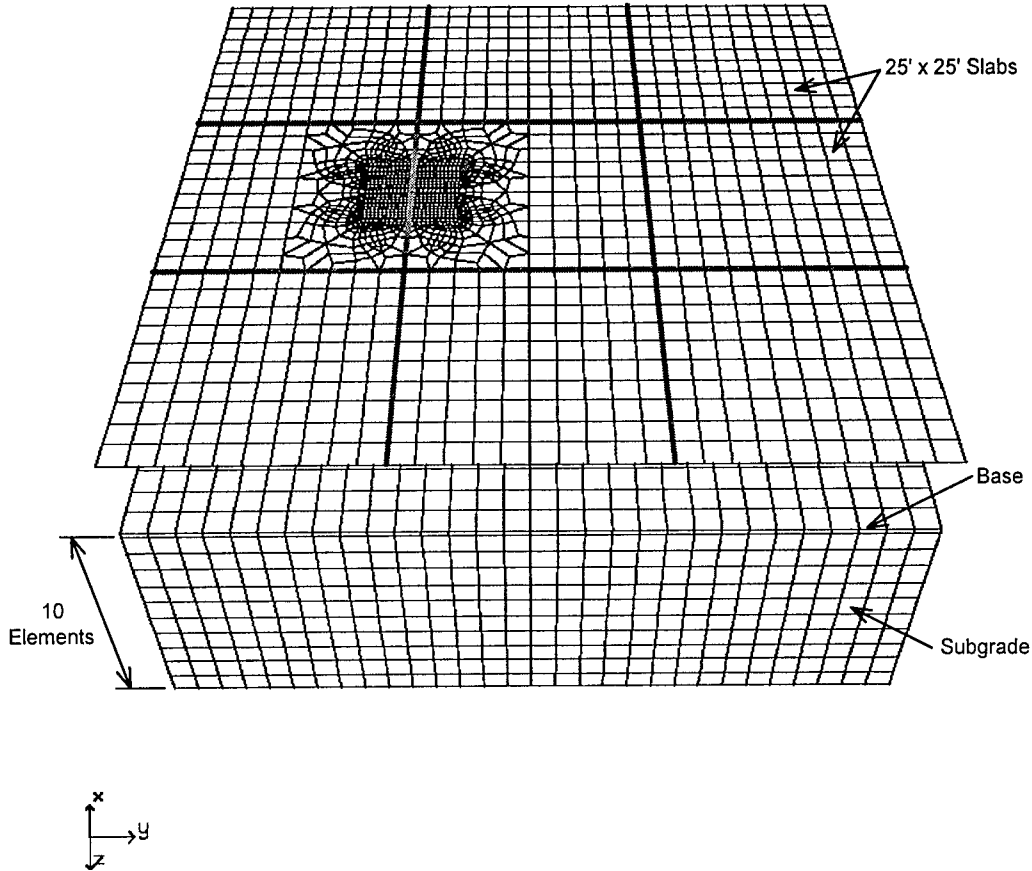


FIGURE 6. DISCRETIZED MODEL FOR RUN TIME ESTIMATES

Table 1 lists nodal counts for the various numerical options as well as estimates of the number of equations, operation counts, and central processing unit (CPU) solution times. Except as noted below, operation counts assume that the system of linear equations is solved directly using a banded Cholesky procedure ( $LDL^T$  decomposition). The Cholesky method applies to banded, symmetric, positive-definite matrices and is more efficient than standard Gauss elimination for these problems. The number of operations (flops) needed to solve the system is given approximately by the formula [5]

$$OC = np^2 + 8np + n$$

where  $OC$  is the operations count,  $n$  is the number of equations (i.e., the number of unconstrained degrees of freedom in the system), and  $p$  is the half bandwidth of the stiffness matrix.

Cholesky decomposition cannot be used for the finite element/boundary element hybrid method because the matrices produced by this method are not symmetric. Banded, nonsymmetric systems can be solved directly using Gauss elimination (*LU* decomposition and back-substitution), for which the approximate operations count is given by the formula [5]

$$OC = 2np^2 + 4np$$

with  $n$  and  $p$  as defined above. Estimates of run times are based on an assumption that the microprocessor performs calculations at a rate of 10.7 megaflops per second ( $10.7 \times 10^6$  operations per second). This rate was based on observations of the actual performance of an SGI Indigo<sup>2</sup> work station with 128 megabytes of random access memory (RAM) programmed to perform repetitive multiplications. The run times in table 1 represent only the solution time for the linear system. However, for problems of the size considered here, the linear solution phase can be expected to account for in excess of 90 percent of the total CPU time charged.

TABLE 1. COMPARISON OF OPERATION COUNTS AND ESTIMATED CPU TIMES FOR VARIOUS MODELING STRATEGIES

Description	Nodes	No. of Equations (Estimated Bandwidth)	Operation Count, MFlops	Estimated CPU time, hours
Discretized subgrade, fixed base (8-node elements)	13681	44607 (5860)	$1.53 \times 10^6$	39.7
Discretized subgrade, fixed base (20-node elements)	9797	35886 (4715)	$7.99 \times 10^5$	20.7
Compliant foundation, Winkler subgrade	4071	18660 (4310)	$3.47 \times 10^5$	9.0
Compliant foundation, Boussinesq	4071	18660 (4310)	$3.47 \times 10^5$	9.0
Infinite elements	4071	18660 (4310)	$3.47 \times 10^5$	9.0
Finite element/ boundary element hybrid	4071	18660 (3243)	$3.93 \times 10^5$	10.2

From table 1, it is apparent that the discretized subgrade with a fixed base is the most expensive foundation option in terms of run time. However, it is also the simplest to implement and requires only that the fixed base be located at a sufficient depth to yield accurate results. If 20-node elements are substituted for 8-node elements (based on one higher-order element replacing eight linear elements) then a CPU time savings of nearly 50 percent is achieved. However, as mentioned above, these higher-order elements are not included in the standard NIKE3D element library. The various compliant foundation options, including the infinite elements option, are all virtually equivalent in terms of run time, and the choice should therefore be based on considerations of accuracy and ease of implementation. The estimate for the finite

element/boundary element hybrid does not reflect the extensive numerical integration needed to form the boundary element stiffnesses. If this extra computational effort is added in (approximately  $3.3 \times 10^4$  Mflops) then the estimated CPU time total for that option increases to 11.0 hours.

The final model uses the option of a discretized subgrade with fixed bases. An alternative model was developed that substitutes a Winkler spring foundation for the discretized subgrade layer (but retains the discretized finite thickness base layers). This alternative model, which is discussed in the section on Automatic Finite Element Mesh Generation, uses NIKE3D material type 17 (Foundation Boundary Spring) to represent the Winkler foundation.

The finite element/boundary element hybrid option was not pursued. It was felt that the moderate time savings did not justify the considerable programming effort involved in developing and qualifying a program to handle mixed three-dimensional FE/BE computations, especially in view of the fact that greater potential time savings are available with a compliant foundation approach.

### LINEAR SOLVERS.

The estimates in table 1 are based on a direct solution algorithm. While direct algorithms such as Gauss or Cholesky decomposition are the best known, they are not necessarily the most efficient solution tools. In particular, the family of PCG solvers may provide much faster solutions where large numbers of equations are involved. In addition, PCG solvers afford considerable data storage savings as compared to direct methods.

A full description of PCG methods is beyond the scope of this report, but reference is made to Atkinson [6] and Hughes and Belytschko [7] for a fuller treatment. Basically, the conjugate gradients are a set of  $n$  independent vectors, or search directions,  $p_i$ , satisfying the orthogonality property [6]

$$\mathbf{p}_i^T \mathbf{A} \mathbf{p}_j = 0 \quad 1 \leq i, j \leq n \quad i \neq j$$

with respect to  $A$ , where  $A$  is the real, symmetric, positive definite matrix of stiffness coefficients, and  $n$  is its rank. If the vectors  $p_i$  are used as the search directions in an iterative scheme, it can be proved that the solution must be found in a maximum of  $n$  iterations, and generally convergence is far faster. Various preconditioners can be applied to matrix  $A$  to improve its condition number and to speed convergence of the conjugate gradient (CG) solution. An advantage of the preconditioned conjugate gradient method as applied to finite element problems is that all of the matrix operations, including preconditioning, can be performed at the element level, so there is no need to form and store the whole global stiffness matrix (as direct solution methods require). The ability to do computations on an *element-by-element* basis rather than globally is the key to the storage savings associated with PCG. A related advantage is that there is no need to minimize the matrix bandwidth in the element-by-element method.

NIKE3D includes both an efficient direct solver (called FISSLE) and a preconditioned conjugate gradient solver with various preconditioning options. Use of the PCG solver in NIKE3D is somewhat restricted. Models involving beam or truss elements, or discrete springs or dampers, are not supported by the PCG solver. Since the material type 17 foundation boundary spring is essentially a system of discrete springs placed at boundary nodes, it is also not supported by the PCG solver.

The finite element model discussed in this section was formulated to be compatible with the NIKE3D PCG solver. Hence it does not include beams or discrete springs (except for the Winkler foundation option). NIKE3D allows the user the option of storing element and conjugate gradient data in core memory (the option recommended by the NIKE3D originators) or on disk in temporary storage files (necessary for very large models). Using an SGI work station with 128 megabytes of RAM, models of up to 100,000 degrees of freedom generated by the automatic procedure discussed in the following section have been successfully executed in core.

Generally, problems involving more than about 10,000 equations will be solved more quickly using a PCG solver instead of an efficient direct solver. However, due to the nature of the iterative process, the exact solution time for a specific problem is difficult if not impossible to predict (see appendix A). In NIKE3D, the initial linear solution is iteratively improved until an equilibrium convergence criterion is satisfied. Between equilibrium iterations, internal forces are recomputed and the set of nodes in contact along the sliding interfaces may be adjusted. The total solution time therefore depends on both the conjugate gradient iterations (the inner loop) and the number of iterations to achieve equilibrium convergence (the outer loop).

#### AUTOMATIC FINITE ELEMENT MESH GENERATION

Automated data preparation is an important part of a successful finite element implementation. Before any finite element computations can take place, a large amount of numerical data is needed to describe the mesh geometry, loading parameters, boundary conditions, material properties, etc. For a typical three-dimensional mesh the number of nodes and elements can run into the tens of thousands. Also, the specific form of the mesh is problem dependent, influenced by such factors as number of wheels and wheel arrangement, load magnitude, load case (i.e., edge loading or interior loading), symmetry, and pavement layer design. Clearly, the task of organizing the data and generating a usable input file is best done by computer.

NIKE3D has a companion preprocessor program (INGRID) that generates three-dimensional meshes in a format readable by NIKE3D. Like NIKE3D and DYNA3D, INGRID is a Fortran 77 program that can be compiled to operate on a workstation in a UNIX environment. No personal computer version is currently available. In contrast to many commercial preprocessors, INGRID has very limited interactive capabilities. The user is required to prepare an ASCII input file containing specific meshing instructions for INGRID. Instruction files may run to hundreds of lines of code and must be written in a complex programming language that can be difficult to master. The language and commands are documented in the INGRID User Manual. [3]

In order to simplify mesh generation for the user, a Windows-based front-end program for INGRID was written in the Visual Basic language. The front-end program (called PreGrid) accepts input from the user and then automatically generates the instruction file for INGRID based on the user-provided information. The PreGrid interface is interactive and user-friendly. There is no need for the user to learn the INGRID programming code.

At the current stage of development, 3 steps are required to generate the NIKE3D input file. First, the INGRID instruction file is generated on a personal computer (PC) running Windows 95 or higher using PreGrid. The generated instruction file is then transferred to the UNIX workstation or other computer running INGRID. Second, INGRID is run using the PreGrid-generated instruction file as input. This step produces a valid NIKE3D input file, but one that lacks information about gear loads and certain nodal constraint and control data. Third, the intermediate NIKE3D input file is automatically modified, adding the missing data, using ReGrid. ReGrid was written in Fortran with a Visual Basic front end. Specific modifications to the NIKE3D input file performed by the ReGrid program are the following:

1. The NIKE3D input file format is changed from Version 2.0 of NIKE3D to Version 3.0.
2. Information about nodal loads is added to the input file.
3. Boundary and symmetry conditions (if applicable) are added to the file.
4. Constrained node pairs are defined for the joint elements. It is necessary to constrain the movement of pairs of nodes in the joint elements to force the joint to deform in shear and prevent rotation of the joint about its longitudinal axis. The continuous linear joint model is described in detail under "Joint Models" in a previous section of this report.
5. Nodal coordinates are scaled to conform to slab dimensions selected by the user. Joint stiffnesses are automatically recalculated to agree with the scaled gap width. Thus the joint stiffness  $k_{joint}$  input by the user is not affected by the scaling operation (see Model Scaling).
6. Data for numerical integration through the shell element thickness by Lobatto's rule is added (see appendix B).
7. Foundation boundary spring (NIKE3D material No. 17) cards are defined. One additional material card is defined for each numerical value of spring stiffness assigned to a node on the foundation. Foundation Node Boundary Condition cards are appended to the end of the file when Material No. 17 is defined. This applies to the Winkler Foundation option only (see Winkler Foundation Option).

The above automatic mesh generation process involves three separate programs and considerable transfer of data from computer to computer. This is necessary because the INGRID program that performs the actual meshing is not set up to run in Windows. One option under consideration is to compile the INGRID code on a PC, and then combine the three programs PreGrid, INGRID, and ReGrid into one integrated mesh generation program whose sole output would be the

NIKE3D input batch file. The effect of the integrated procedure would be to make the actual mesh generation transparent to the user.

### WINDOWS-BASED INTERACTIVE FRONT END.

The main interactive window for PreGrid is shown in figure 7. User data input for this program is limited to three general categories: aircraft data, pavement layer data, and load case. Selection of the aircraft gear is made as easy as possible. The user selects an aircraft from a pull-down menu at the left. Aircraft types are organized according to aircraft manufacturer, with a number of generic gear types included as well (e.g., single wheel, dual tandem). The list of aircraft is adopted from the list included in the Layered Elastic Design/Federal Aviation Administration (LEDFAA) pavement design standard. [9] When the user selects an aircraft, the main gear footprint appears in the large graphics window. Using the "Edit Wheels" buttons on the right, the user can add, remove, or move wheels to create a new configuration. Information about the distribution of loads to the individual wheels in the gear is shown in a table under the graphics window. The following variables are assigned default values from the aircraft library, but can be modified interactively from the PreGrid window: Gross Vehicle Weight (GVW), Percent of GVW on Main Gear, Tire Pressure. The load case (edge or interior load) is selected in the box at the lower right. For edge loading, the default orientation of the gear is parallel to the joint, but a perpendicular orientation can be selected by checking the appropriate box.

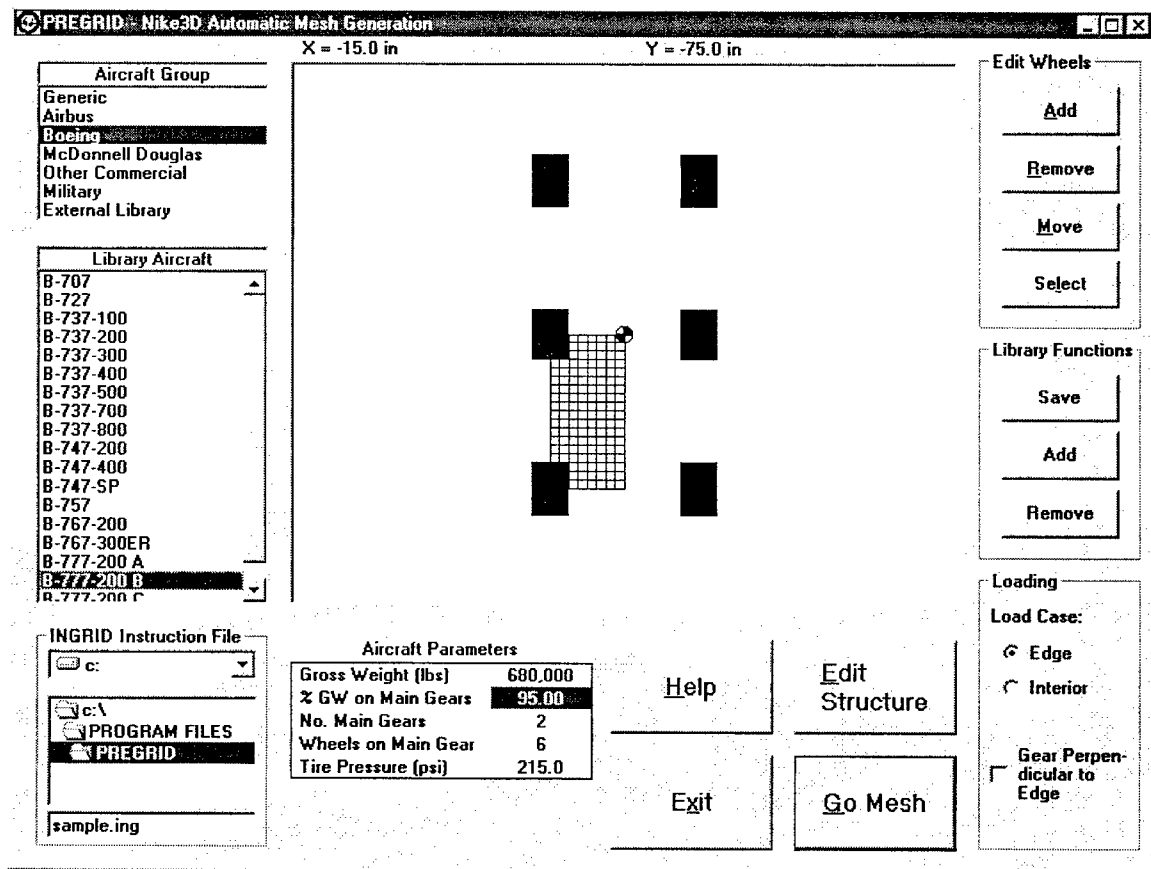


FIGURE 7. MAIN WINDOW DISPLAY FOR PreGrid

The pavement structure is entered in a separate window, the Pavement Structure window shown in figure 8. Layer thicknesses and properties can be entered or modified at any stage prior to final generation of the mesh instruction file. Properties can be entered for four layers: the PCC slab, layer 1, layer 2, and the subgrade layer. The PCC slab and layer 1 are required. In addition, either a discretized subgrade layer or a Winkler foundation must be entered. In most cases, layer 1 is the base layer and layer 2 represents a subbase. However, if no subbase is required for a particular section, then entering zero for the layer 2 thickness causes the program to skip that layer. Each active layer requires two elastic constants: Young's modulus  $E$  and Poisson's ratio  $\mu$ . For the PCC slab, these elastic constants are internally set to  $E = 4,000,000$  psi and  $\mu = 0.15$ .

**PAVEMENT STRUCTURE**

<b>Slab</b> Thickness: 14 Young's Modulus E: 4,000,000 psi Poisson's ratio: 0.15 Joint Spring Constant: 100000	<b>Slab Dimensions</b> X Dimension: 25 Y Dimension: 25
<b>Layer 1</b> Thickness: 8 Young's Modulus E: 75000 Poisson's ratio: 0.35	<b>Cracked Base</b> <input type="checkbox"/> Base Layer Cracked
<b>Layer 2</b> Thickness: 8 Young's Modulus E: 75000 Poisson's ratio: 0.35	<input type="button" value="OK"/>
<b>Subgrade Layer</b> Young's Modulus E: 15000 Poisson's ratio: 0.4	<b>Foundation Options</b> <input checked="" type="radio"/> Subgrade Layer <input type="radio"/> Winkler Foundation

FIGURE 8. PAVEMENT STRUCTURE EDIT WINDOW FOR PreGrid

By default, the program generates a three-dimensional subgrade mesh with elastic properties as assigned in the Pavement Structure window. An option allows the user to substitute a dense liquid (Winkler) foundation for the discretized subgrade layer. If the Winkler Foundation option in figure 8 is selected, no subgrade mesh is generated. The Winkler option, and certain limits on

its use, are discussed below. A second option, Base Layer Cracked, generates a mesh with a discontinuity in the base layer at the location of the joint. The discontinuity is modeled as a fully unbonded, vertical type 2 sliding interface. This option is particularly useful for analyzing the effect of cracks in high-stiffness stabilized base layers that frequently form at the joint location. The cracked-base option is selected by checking Base Layer Cracked in the Pavement Structure window (figure 8).

As discussed in reference 8, the program PreGrid actually produces two ASCII text files. The first, given a file name with an extension .ing, is the actual INGRID instruction file. The second file, given the same base file name but with the extension .rgd, is a file containing data for the load geometry used later by the program ReGrid. Once all data entry is complete, the user clicks on Go Mesh (figure 7) to generate the files.

#### MESH GENERATION USING INGRID.

INGRID produces models by generating parts and combining them into larger assemblages via a nodal merging process. Controlling the merging process can be the most difficult aspect of using INGRID, which is why the PreGrid program was developed under this research effort to automate the process and make it transparent to the end users. Three types of parts are available. "Standard" parts are used for generating three-dimensional meshes. "MAZE" parts are used for generating two-dimensional elements (e.g., shells) and can also be stacked to form regular three-dimensional meshes. Transition elements can be used to provide 3:1 or 2:1 transitions in mesh density between adjacent MAZE parts. The third type of part, one-dimensional beam parts, is not used in the final model.

In the final model, all three-dimensional mesh regions (base, subgrade, joints) use standard parts, while the two-dimensional slab region is meshed using MAZE parts.

#### SYMMETRY CONSIDERATIONS.

PreGrid automatically checks the mesh and the loading to ascertain whether symmetry exists. If symmetry exists, then the appropriate symmetry planes (one or two) are formed in the model. For interior loading, either one or two planes of symmetry may exist, depending on the gear geometry. For edge loading, only one plane of symmetry (the  $x$ - $z$  plane) is possible. Symmetry planes are formed by imposing appropriate displacement or rotational constraints on nodes on the plane of symmetry. By taking advantage of symmetry, the size of the finite element problem that needs to be solved is substantially reduced. As an option, NIKE3D allows symmetry planes to be defined based on a penalty formulation similar to the sliding interfaces. However, this NIKE3D feature was not used in the current model.

#### BASE AND SUBGRADE LAYER MESH.

Figures 9 and 10 show typical three-dimensional meshes for the base and subgrade region. In figure 9, circular and spherical mesh patterns were used to transition from a fine mesh in the vicinity of the load to a coarse mesh in the far field. A reasonable element aspect ratio was



maintained throughout all parts of the three-dimensional mesh. The maximum element side length used for three-dimensional elements in the vicinity of the load is 5 inches.

Rigid Airport Pavement  
INGRID Display of Master Slide Surface

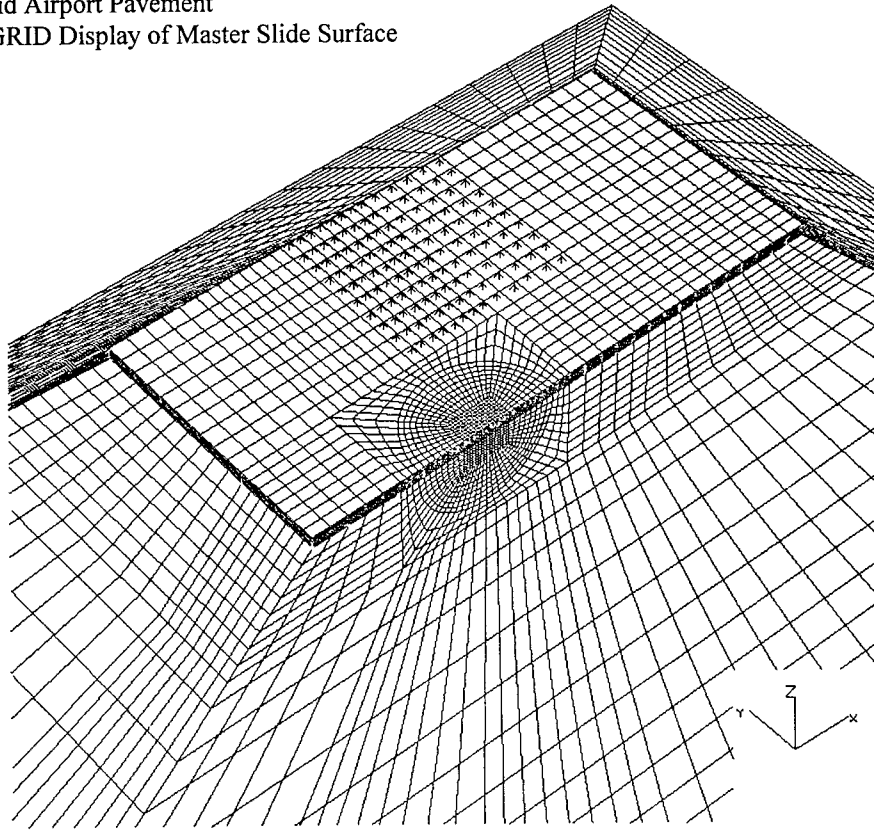


FIGURE 9. THREE-DIMENSIONAL MESH FOR BASE AND SUBGRADE LAYERS  
(EDGE LOAD CASE)

The “truncated pyramid” shape of the subgrade meshes shown in figures 9 and 10 is influenced by two principles. The zone of influence of the applied vertical load tends to expand with greater depth below the slab, so a larger area must be meshed at greater subgrade depths. At the same time, the effect of the applied load diminishes as the distance from the point of load application increases, justifying a coarser mesh density in the parts of the mesh far from the load. The horizontal ( $x$  and  $y$ ) coordinates of the nodes are scaled linearly with depth, resulting in a pyramidal shaped mesh whose nodal density gradually decreases in all directions away from the load, as shown in figures 9 and 10. The horizontal scale factors are set so that the nodes on the side boundaries of the mesh slope at a 45-degree angle to the vertical, while nodes on vertical planes of symmetry remain vertical.

The mesh in figure 9 was generated assuming edge loading of the center slab by a B-777 main gear (see figure 7). For this type of problem there is one plane of symmetry (the  $x$ - $z$  plane). The PreGrid program detected the single plane of symmetry and consequently instructed INGRID to produce a mesh for only one-half of the problem domain. For interior loading problems where two planes of symmetry are detected, one-quarter of the problem domain is meshed (figure 10).

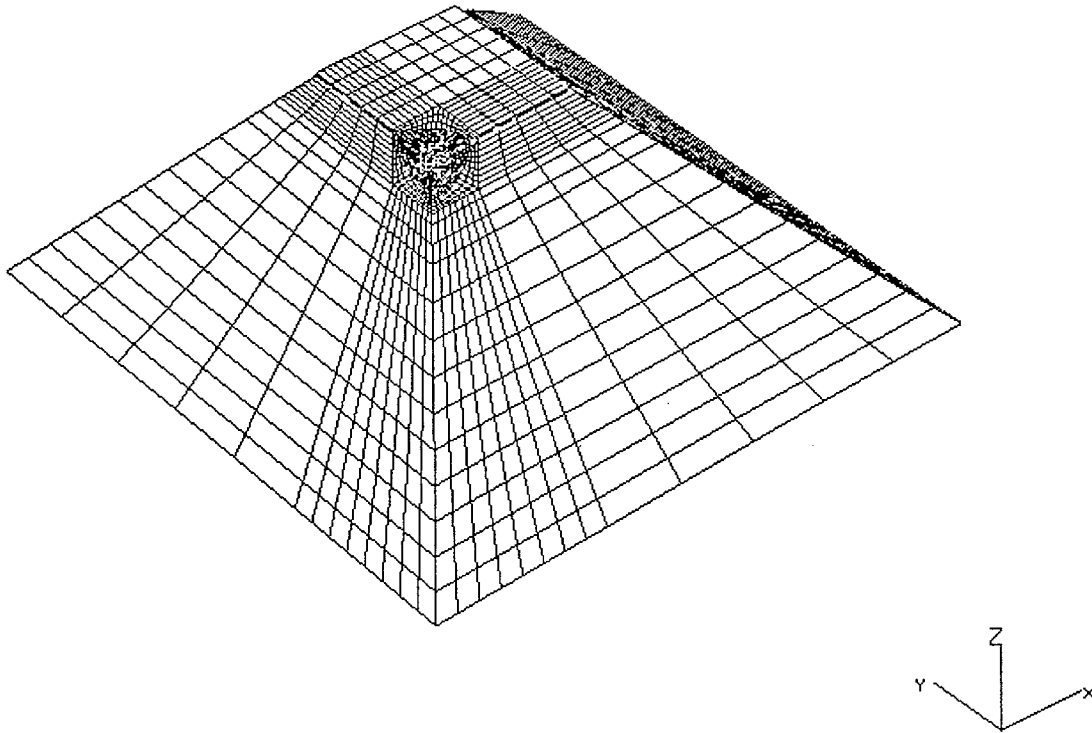


FIGURE 10. THREE-DIMENSIONAL MESH FOR BASE AND SUBGRADE LAYERS  
(INTERIOR LOAD CASE)

The upward-pointing arrows in figure 9 indicate an area where a sliding interface is defined. The interface area is the contact surface between the top of base layer and the base of one of the 25-by 25-foot slabs. The base layer surface is defined as a master surface and the slab surface (see figure 11) as a slave surface, but this is a purely arbitrary designation, as Type 3 slide surfaces in NIKE3D are symmetrical with respect to master/slave designation. In the edge-loading model shown (figures 9 and 11) there are a total of six defined slide surfaces, one surface corresponding to each of the slabs in the model.

#### SLAB LAYER MESH.

Figure 11 shows a top view of a mesh produced by INGRID for the slab layer. The problem is the same as in figure 9, edge loading by a B-777 main gear. The slabs are separated by gaps of 1 inch thickness at the joints to allow room for the joint elements. A detail of the fine mesh area with the B-777 load is shown in figure 12.

Figures 11 and 12 illustrate the mesh pattern used for 3:1 and 2:1 transitioning in two dimensions. Typical element side lengths in the coarse mesh region are 12.5 inches. By the use of a row of 3:1 transitioning elements and then a row of 2:1 transitioning elements, the element length in the fine mesh region is 2.083 inches.

Rigid Airport Pavement  
INGRID Display of Slave Slide Surface

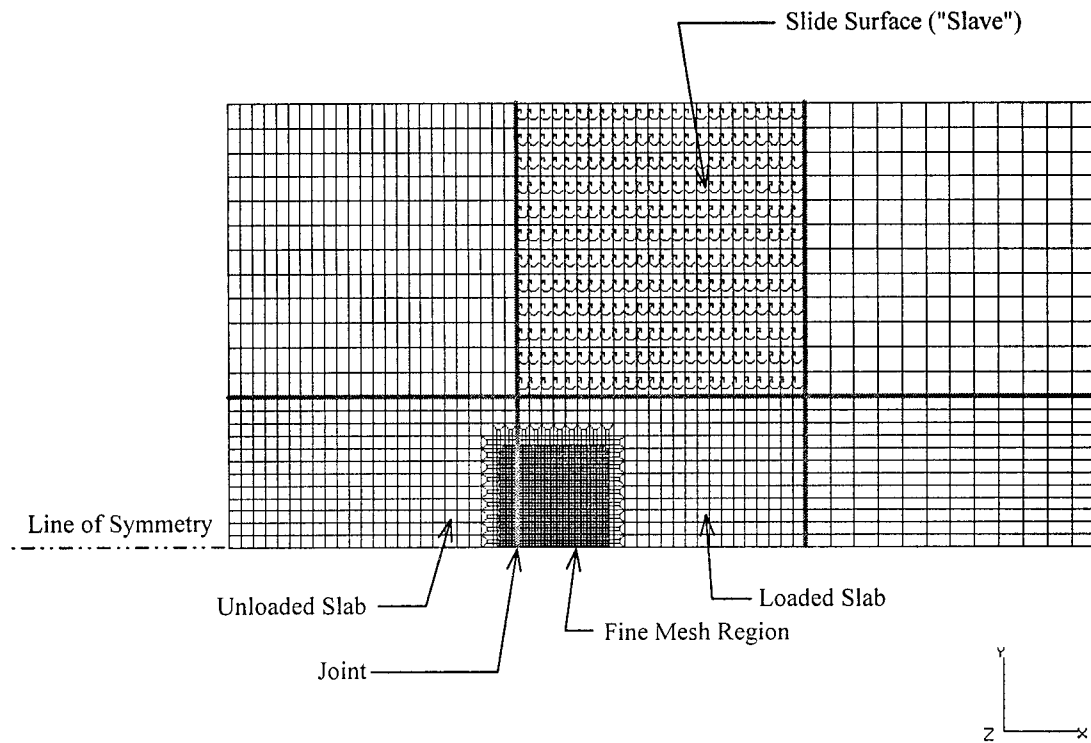


FIGURE 11. TWO-DIMENSIONAL MESH FOR SLAB LAYER (EDGE LOAD CASE)

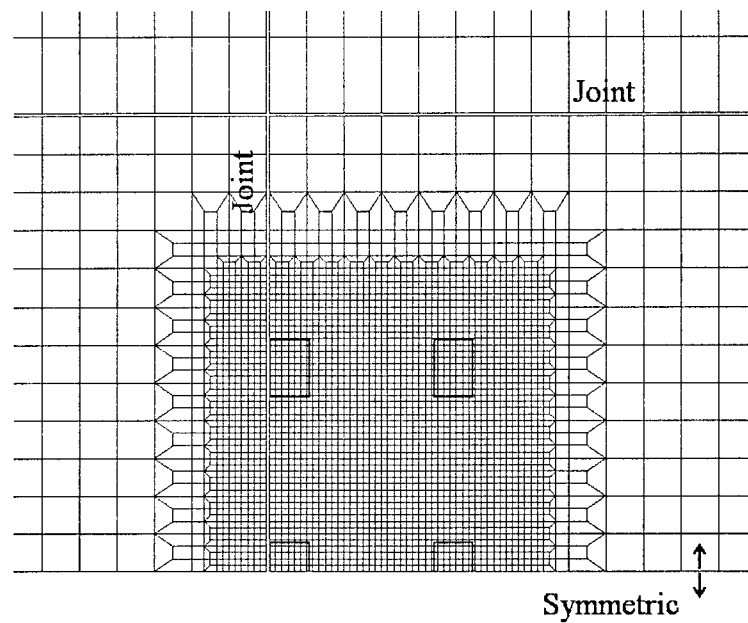


FIGURE 12. DETAIL OF SLAB MESH WITH B-777 MAIN GEAR LOAD

The slave slide surface in figure 11 corresponding to the master slide surface in figure 9 is shown by the curved arrows. By the right hand convention, the arrows point downward, indicating that the surface faces the top of the base course. The reference plane for shell elements coincides with the slab/base interface in all cases.

## MODELING THE AIRCRAFT GEAR LOADS.

DETERMINATION OF THE NODAL LOADS. Figure 12 shows the main gear footprint for the B-777 aircraft superimposed on the surface mesh. Due to single-plane symmetry, only four of the six wheels comprising the gear appear in the figure. Wheel loads are applied to the surface mesh by a tributary area method according to the following rules:

1. The wheel load is assumed to be uniformly distributed on a rectangular loading patch. The shape of the load patch is the equivalent rectangular load patch developed for rigid pavement design by the Portland Cement Association (PCA). The dimensions of the rectangle are  $0.8712 \times L$  by  $0.6 \times L$ , where  $L$  is given by the formula

$$L = \sqrt{\frac{A_c}{0.5227}}$$

and  $A_c$  is the nominal tire contact area obtained by dividing the tire load by the nominal contact pressure. The PCA load patch is described in references 10 and 11.

2. Nodal loads are computed by a tributary area method, with the tributary area for each node computed following the diagram in figure 13. The nodal load is the product of the tributary area and the nominal contact pressure for the gear.
3. The center-to-center dimensions of the load patches are equal to the actual center-to-center dimensions of the wheels comprising the aircraft gear.
4. For the edge loading case, the edge of the slab lines up with the long side of the rectangular load patch. For the interior load case, the geometrical center of the gear coincides with the center of the slab.

TIRE PRESSURE DISTRIBUTION. A preliminary study was conducted to evaluate the possibility of using nonuniform tire pressures or nonrectangular tire load patches in the finite element model. For comparison with the uniform distribution, an idealized nonuniform tire pressure distribution based on the work of Tielking [12] was assumed (see figure 14). The following conclusions were made from this study:

1. A relatively high nodal density in the tire contact region is needed to capture the nonuniform pressure variation within the tire contact region.

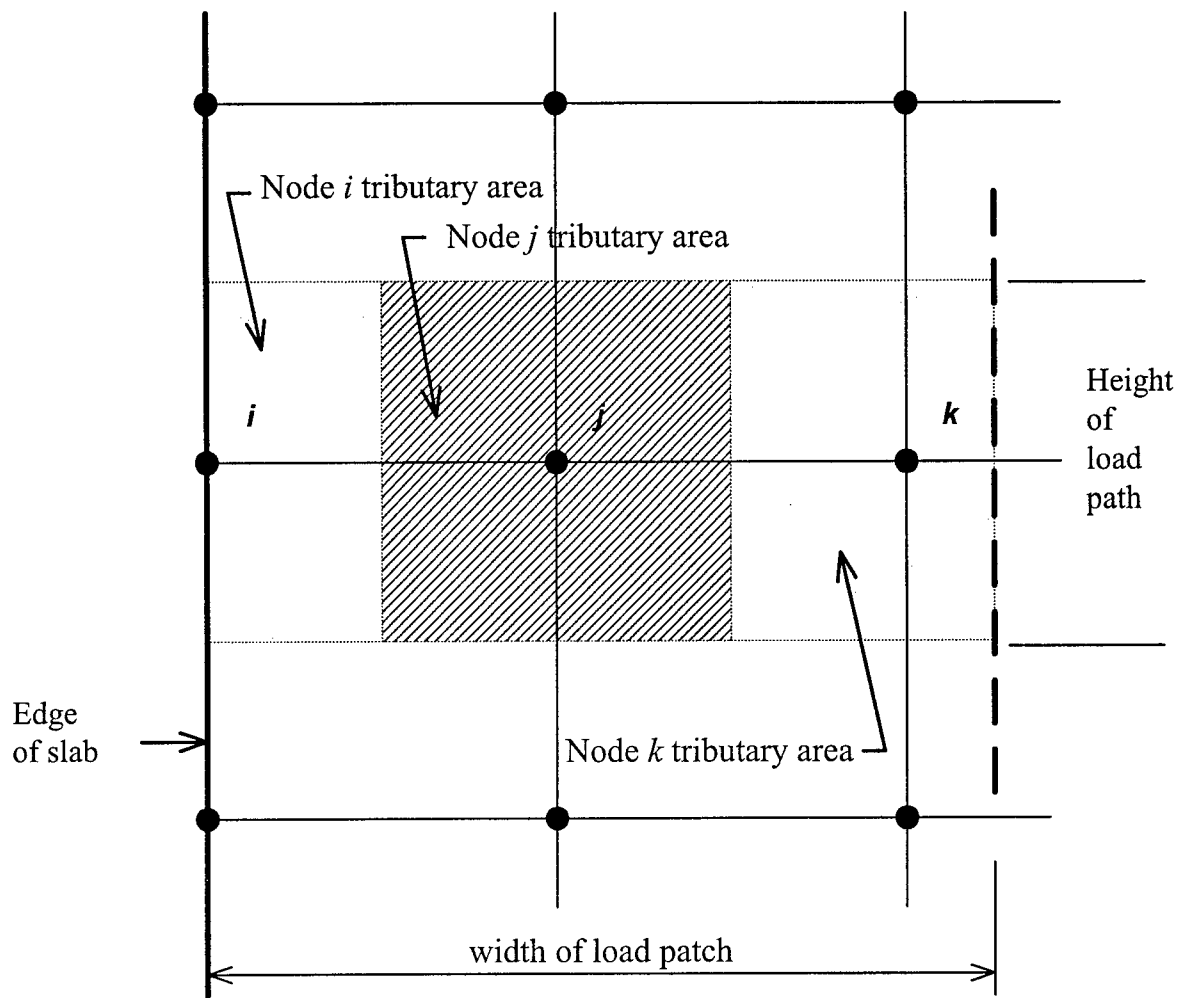
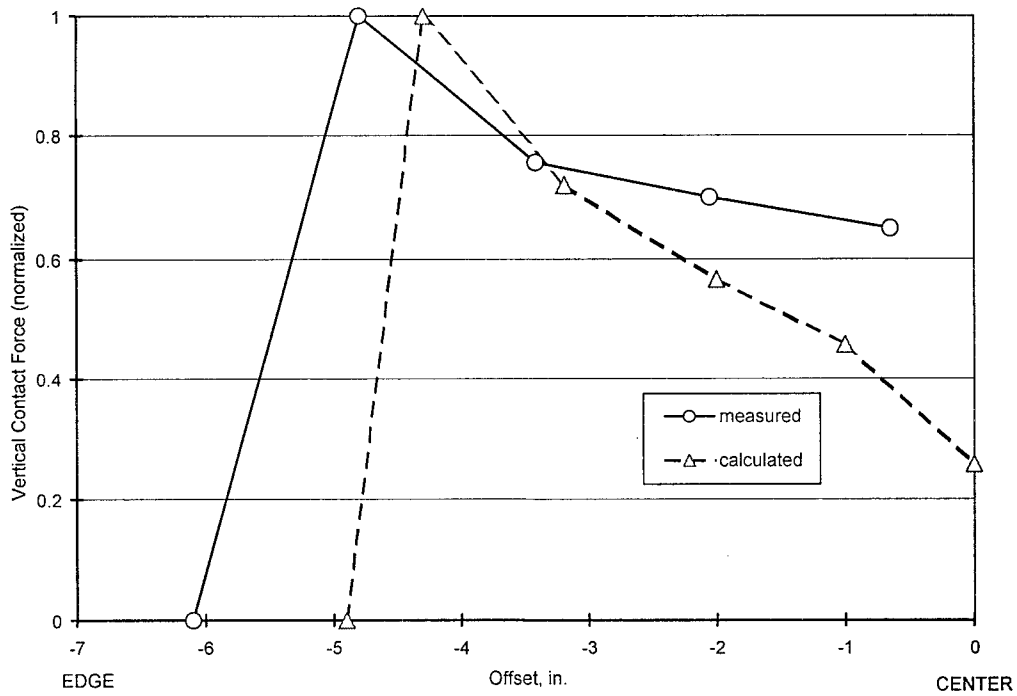
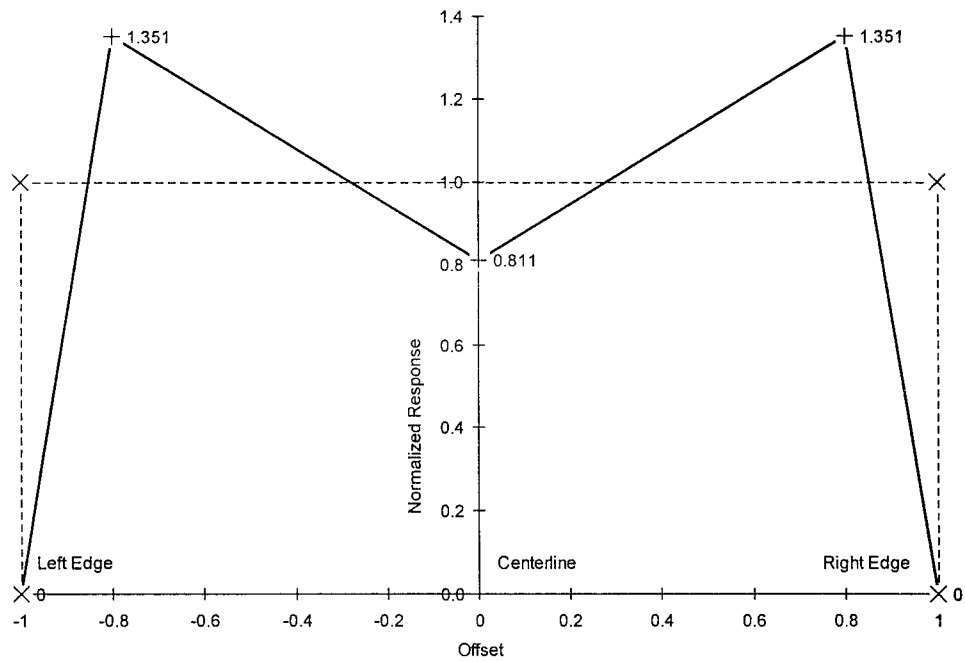


FIGURE 13. NODAL LOAD DISTRIBUTION BY TRIBUTARY AREA METHOD

2. Data collected by Tielking [12] indicates that several factors affect actual pressure distributions in aircraft tires, including tire inflation pressure and tire design (bias versus radial, etc.). As a result, distributions for different aircraft may not be similar. Tielking compared measured pressure distributions for a B-737 tire to predictions from a finite element model (see figure 14). His results suggest that tire pressure variability is mainly in the lateral direction, with the longitudinal pressure distribution close to uniform.
3. For the rigid pavement case, critical stresses predicted by assuming a nonuniform tire pressure distribution did not vary significantly from critical stresses predicted for a uniform distribution. Likewise, stresses for the nonrectangular PCA load patch did not vary significantly from those for the rectangular PCA load patch.



(a) Transverse Distribution of Tire Footprint Forces for B-737 Aircraft Tire (After Tielking, 1990)



(b) Assumed Nonuniform Distribution of Tire Contact Pressures (Normalized to Equivalent Uniform Pressure)

FIGURE 14. NONUNIFORM TIRE CONTACT PRESSURE DISTRIBUTION

Table 2 contains stress comparisons for nonuniform versus uniform pressure distributions and nonrectangular versus rectangular load patches. Stresses in table 2 were computed for the case of Boeing B-737 single tire (edge stress) using the finite element program KENSLABS. [11] The critical stress is the maximum bending stress computed in the base of the slab. Assumptions are as listed in table 2.

TABLE 2. EFFECT OF NONUNIFORM TIRE PRESSURE DISTRIBUTION AND LOAD PATCH SHAPE ON FINITE ELEMENT COMPUTED CRITICAL STRESS FOR B-737 SINGLE-WHEEL LOAD

Description of Load	Critical Stress, Base of Slab (psi)	Percent Variation
Uniform pressure distribution, PCA rectangular load patch	495.37	N.A.
Nonuniform distribution in the lateral direction, PCA rectangular load patch	494.86	0.103%
Uniform pressure distribution, PCA oval load patch	494.88	0.99%
Assumptions: 1. Slab size 120 x 90 x 12 in (15 x 10 x 1 ft) 2. Edge loading on long edge of slab 3. Winkler foundation, $k = 200$ pci 4. Concrete properties: $E = 4 \times 10^6$ psi, $\mu = 0.15$ 5. Loading: B-737 single wheel, Total load = 30,000 lbs., Contact pressure = 155 psi 6. Uniform pressure distribution in longitudinal direction 7. Nonuniform pressure distribution in lateral direction, see figure 10.		

Based on the study, the use of nonuniform pressure distributions or nonrectangular load patches was not justified in the present model.

#### CONTROLLING THE MESH DESIGN.

In the finite element method the optimal mesh design gives the required level of accuracy using the fewest elements. One way to control the number of elements in the mesh is to limit the size of the fine mesh region relative to the rest of the model. Another way is to limit the mesh density. Because establishing appropriate mesh dimensions for a given class of problems is largely a trial and error process, the automatic mesh generation program was designed to allow modifications to the basic mesh to be made easily by changing one or more internally set control parameters.

The automatic mesh generation program creates a mesh for the slab layer consisting of two-dimensional shell elements as shown in figures 11 and 12. The fine mesh region may be larger or smaller as needed, depending on the main gear characteristics of the aircraft type selected. For example, multiple-wheel gears such as the B-777 will require a more extensive fine mesh region,

hence more nodes in the mesh, than single-wheel gears. To handle this meshing requirement, the automatic mesh generation program assigns different values to the control dimensions shown in the diagram in figure 15. The distances shown as  $c$ ,  $c'$ , and  $e$  define the limits of the fine mesh area. Similarly,  $a$ ,  $a'$ , and  $b$  are parameters that define the limits of the transition mesh area.

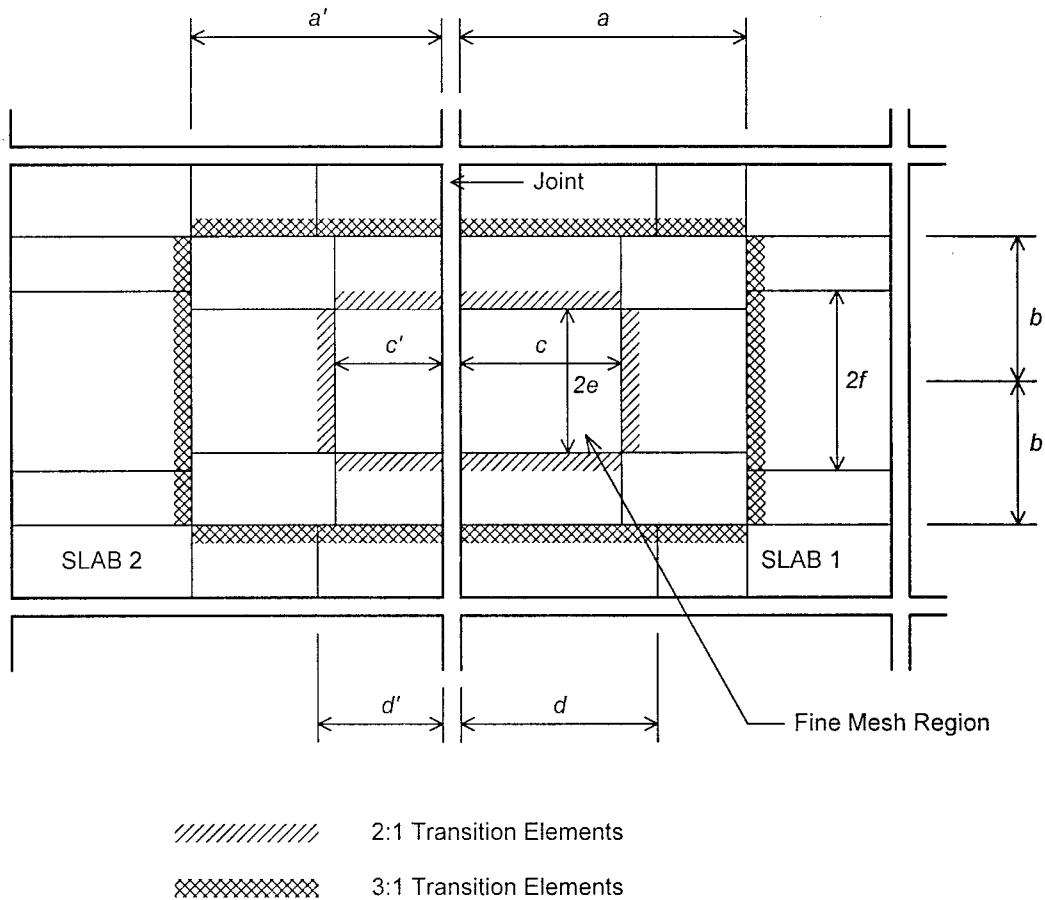


FIGURE 15. CONTROL DIMENSIONS FOR SLAB MESH (EDGE LOAD)

In the framework of figure 15, fine mesh density is related to coarse mesh density in the slab by a 6:1 ratio defined by the two layers of transition elements. Layer 1 consists of 2:1 transition elements in the region defined by  $2f-2e$  and  $(d+d')-(c+c')$ . Layer 2 is a 3:1 transition element region immediately adjacent to the coarse element region. Practically, the fine mesh can take on only discrete values related to the slab dimensions. For example, if the length of the side of slab 1 is taken as 300 inches (the default value) and the coarse mesh spacing is 12.5 inches (i.e., 24 elements equally spaced along the slab side), then the side of an element in the coarse mesh region is 12.5 inches divided by 6, or 2.083 inches. If the coarse mesh spacing were changed to 20 inches (15 elements along the slab side), then a fine mesh spacing of 3.33 inches would result, and so forth, always in a 6:1 ratio. In this way, the fine mesh density is controlled as well as the extent of the fine mesh region. The effect on model response of altering the fine mesh density is discussed in the section "Model Sensitivity Analysis."



Care must be taken to choose combinations of parameters that result in a proper and valid mesh when processed by INGRID. For example,  $c$  and  $c'$  in figure 12 must be chosen as even multiples of  $2\Delta_f$ , where  $\Delta_f$  is the fine mesh element side length (i.e.,  $8\Delta_f$ ,  $12\Delta_f$ , etc.). Otherwise, an invalid mesh (that is, invalid for NIKE3D) may result, as shown in figure 16. In order to avoid the type of meshing error shown in figure 16, the control dimensions for a given gear geometry are determined from the flowchart shown in figure 17.

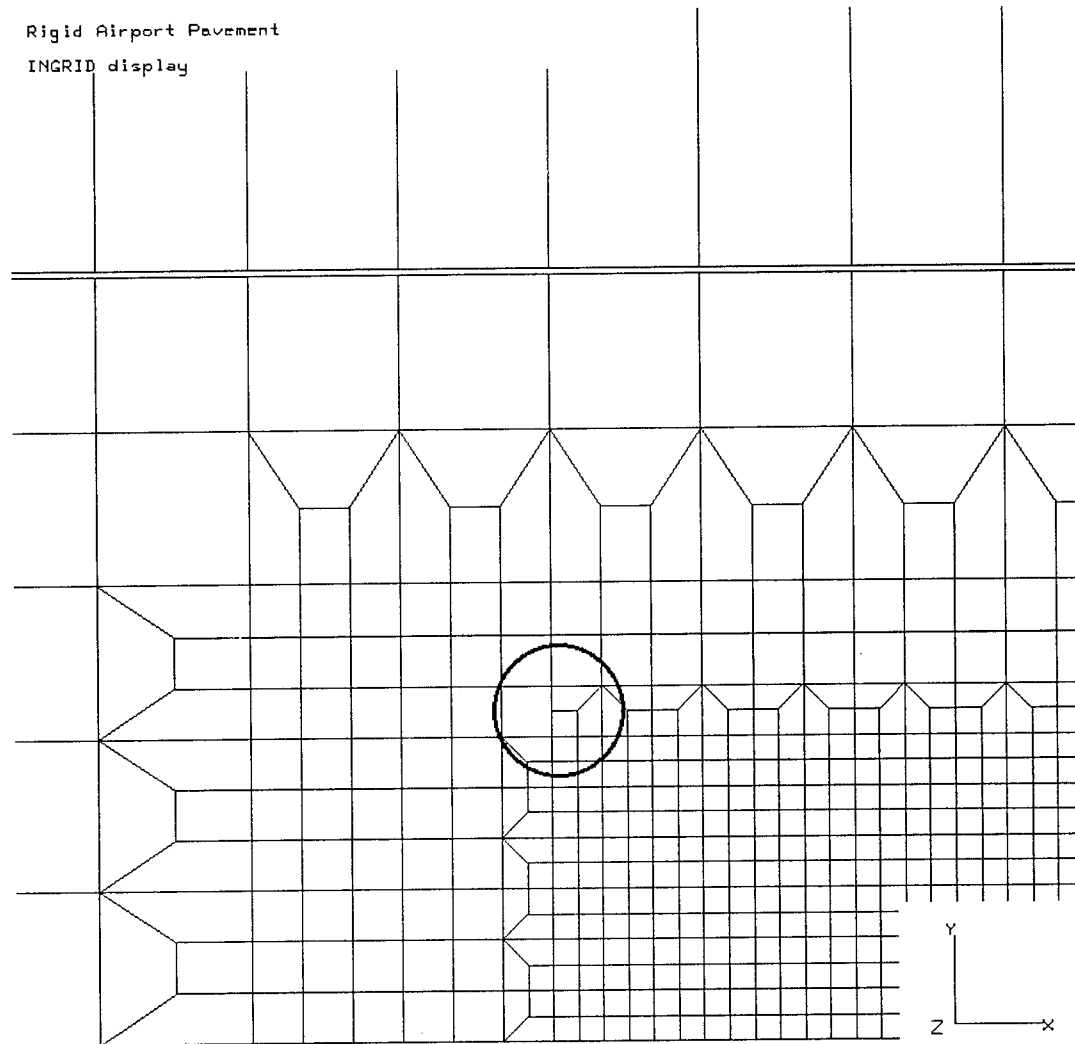


FIGURE 16. DETAIL OF INVALID SLAB MESH RESULTING FROM INCORRECTLY CHOSEN PARAMETERS

The method for assigning nodal loads based on tributary areas requires that the entire gear footprint be located within the regular fine mesh area, and that none of the wheels be located in the transition area. The flowchart procedure (figure 17) results in a valid NIKE3D mesh for arbitrarily configured aircraft gears and a fine mesh region that extends beyond the gear footprint area by a minimum of 30 inches on all sides. The 30-inch overlap ensures that plots of computed bending stress and deflection created using the mesh are visually smooth.

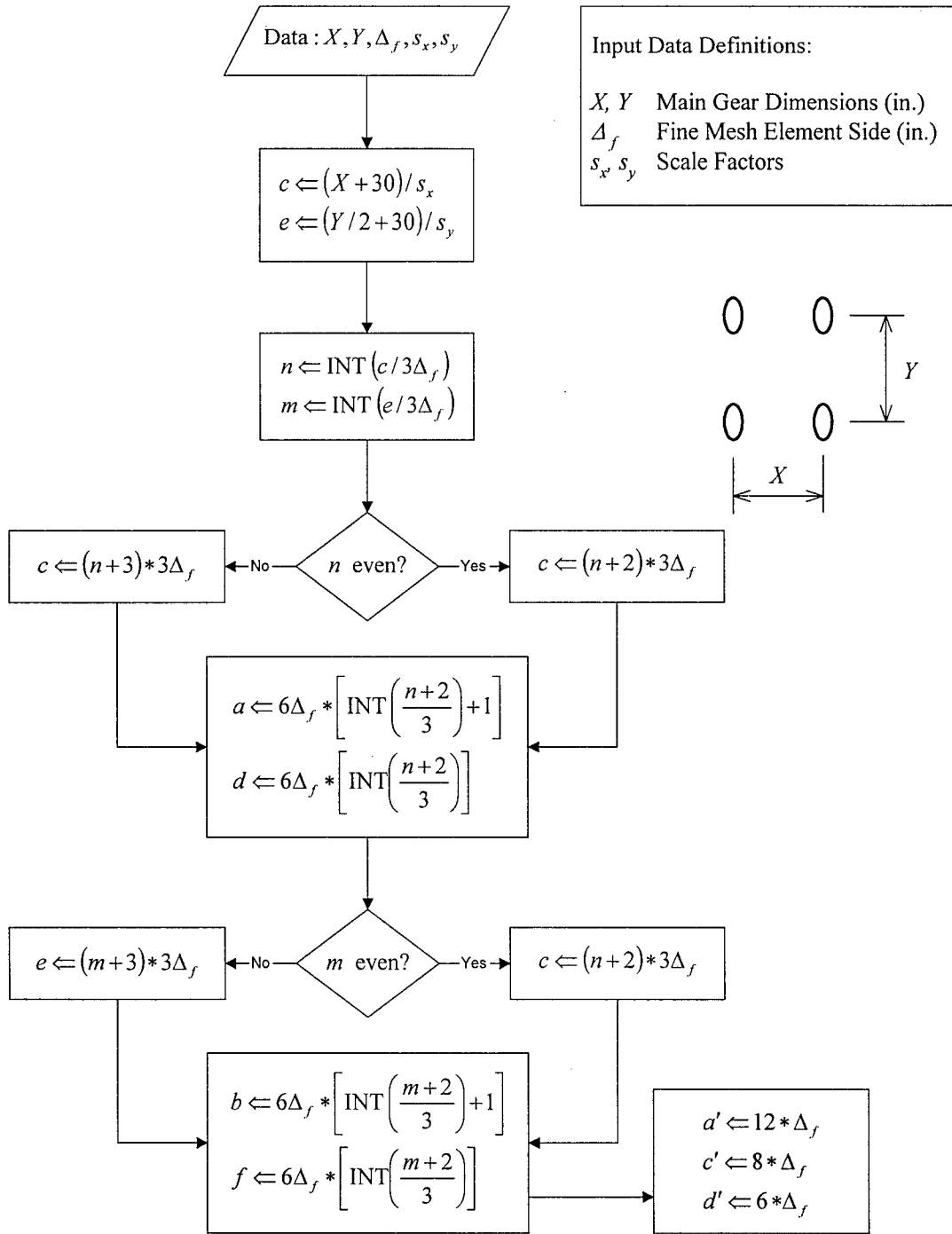


FIGURE 17. FLOWCHART FOR COMPUTING CONTROL DIMENSIONS IN AUTOMATIC MESH GENERATION PROGRAM (EDGE LOAD)

#### NODAL MERGING.

Each of the large two-dimensional areas created by the divisions in figure 15 constitutes a separate INGRID part. [3] Likewise, the three-dimensional mesh shown in figures 10 and 11

consists of multiple three-dimensional parts. When initially created, these parts are disjoint (unconnected). Prior to execution of the finite element program the disjoint parts must be merged via a process that eliminates redundant nodes. The nodes are merged by sending a “part tolerancing” instruction to INGRID where the tolerance is the specified distance between adjacent nodes in excess of which the nodes will not be merged. The current model specifies a tolerance of 0.01 inch. Since the assigned width of 3D joint elements is 1 inch, nodes opposing each other across a slab joint will not merge. The horizontal plane coinciding with the sliding interface between the slab layer and the base layer is assigned a z-coordinate of zero. In order that nodes on opposite sides of the sliding interface not merge during the part tolerancing process, a “NOMERGE” instruction is issued to INGRID for each defined slide surface. The NOMERGE instruction applies only to nodes on opposite sides of the sliding interface that would otherwise meet the geometric merging criterion.

### MODEL SCALING.

The default slab size for the automatic mesh generation program is 25 by 25 feet. This size conforms to the preliminary model specification. However, if the actual slab under consideration has different dimensions, it is possible to scale the model to conform to the required dimensions. The slab dimensions are entered in the program PreGrid in the Pavement Structure window (figure 8), but the actual scaling of nodal coordinates is performed within the program ReGrid as a modification of the intermediate mesh generated by INGRID. The entered slab dimensions define scale factors  $s_x$  and  $s_y$  as ratios of the actual to the default slab size, i.e.,

$$s_x = L_x/300$$

$$s_y = L_y/300$$

where  $L_x$  and  $L_y$  are the entered slab dimensions in the  $x$  and  $y$  directions respectively, in inches. The scale factors  $s_x$  and  $s_y$  are applied to the  $x$  and  $y$  nodal coordinates respectively, allowing the  $x$  and  $y$  slab dimensions to be independently varied. Vertical nodal coordinates ( $z$  coordinates) are not affected by the scaling operation. Default values of both  $s_x$  and  $s_y$  are 1.0.

### CRACKED-BASE OPTION.

High-stiffness base and subbase layers may develop vertical cracks, particularly at joint locations. In order to model this cracked-base condition, the automatic mesh generation program contains an option for generating the mesh with a discontinuity in the base and subbase layer mesh. The discontinuity is located under the principal joint as shown in figure 18.

Selecting the “Cracked-Base” option in figure 8 suppresses nodal merging between layer 1 and layer 2 mesh parts located on opposite sides of the assumed crack line in figure 18. Instead, a double row of nodes is created at the crack location (figure 19) and PreGrid instructs INGRID to define a Type 2 (sliding only) sliding interface there. With the Type 2 sliding interface, opposing surfaces are maintained in contact, but shear forces are prevented from developing across the interface.

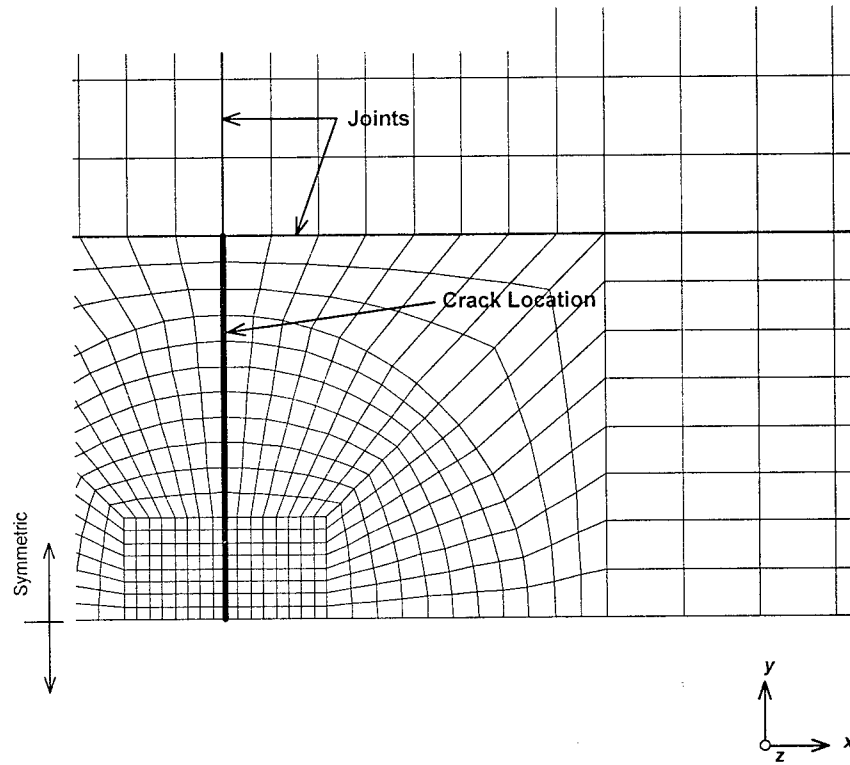


FIGURE 18. CRACK LOCATION FOR CRACKED-BASE MODEL

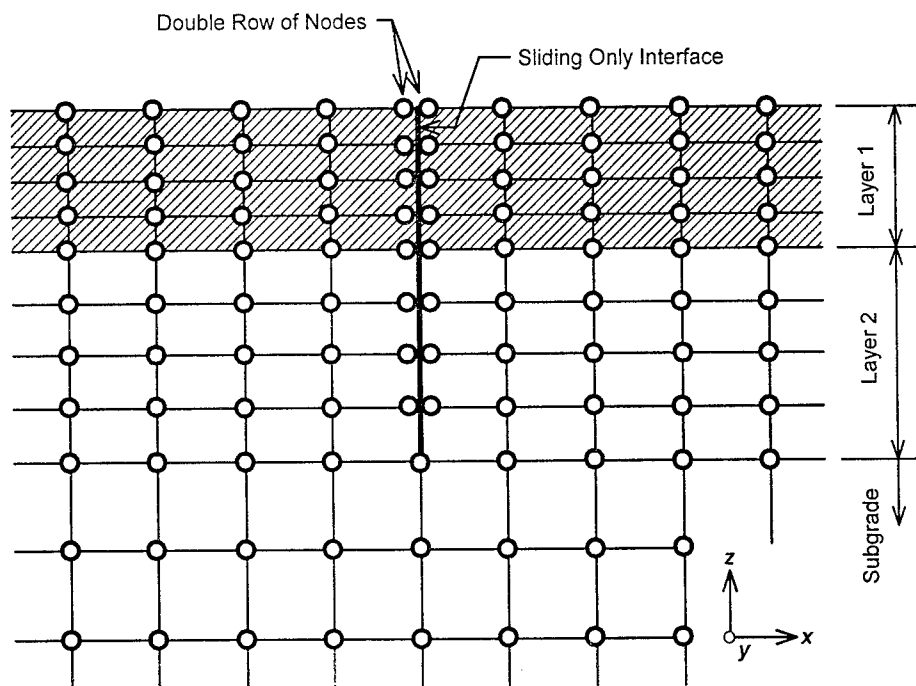


FIGURE 19. NODAL ARRANGEMENT FOR CRACKED-BASE OPTION

## WINKLER FOUNDATION OPTION.

Selecting the Winkler Foundation option in figure 8 replaces the discretized subgrade mesh by a numerical approximation of the Winkler support condition. The Winkler model assumes that the rigid slab is supported on a dense liquid foundation characterized by a modulus of subgrade reaction  $k$ . The modulus of subgrade reaction has units of force per unit length per unit area and represents a foundation spring stiffness associated with a unit area of the supported slab.

The Winkler foundation can also be conceptualized as a bed of vertical springs supporting the bottom of the slab. In the finite element model, the Winkler foundation is approximated by discrete springs as shown in figure 20. One end of the spring is connected to a foundation node and the other end is fixed on a horizontal plane. The spring constant is the product of the assumed  $k$  value and the tributary area for the foundation node (figure 20). The finite element model with a Winkler foundation differs from Westergaard's idealization of a slab supported by a dense liquid in that the base layer (and subbase, if present) are modeled using discrete three-dimensional elements, and only the subgrade is represented by a spring foundation.

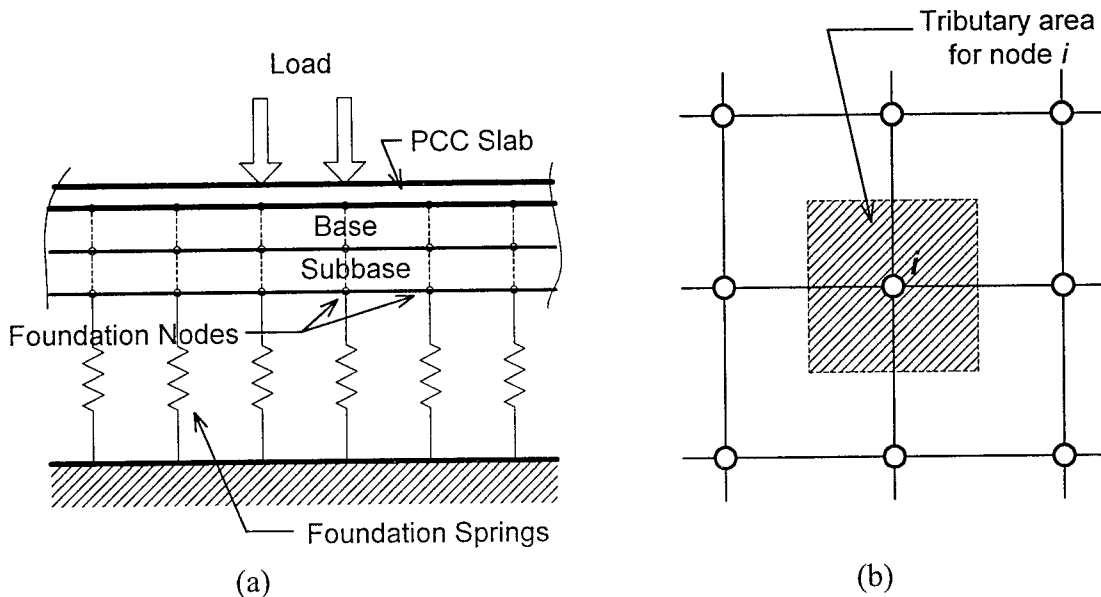


FIGURE 20. SCHEMATIC OF WINKLER FOUNDATION SHOWING (a) FOUNDATION NODES AND SPRINGS AND (b) NODAL TRIBUTARY AREA

NIKE3D supports the spring foundation concept. NIKE3D material type 17 (Foundation Boundary Spring) is used in the current model to define a Winkler-type spring mat foundation. Material type 17 is not a true material but rather a matrix of spring constants defining a three-dimensional spring. (The spring constants are given in appendix C.) Each designated foundation node is associated with a single material definition. Since the spring constants are fixed, the number of required material definitions is equal to the number of designated foundation nodes having distinct tributary areas. The program ReGrid contains a routine for evaluating the tributary areas and determining the required number of material type 17 definitions and associated spring constants. In order to avoid unnecessary proliferation of material definitions,

two designated foundation nodes are assigned the same foundation spring stiffnesses if their tributary areas do not differ by more than 1.0 in<sup>2</sup>.

The Winkler Foundation option always results in a model with fewer equations to solve than the equivalent model with a fully discretized subgrade. However, because the Winkler model involves discrete springs (the foundation springs), it is not possible to use the PCG solver to solve the model in NIKE3D. Models created using the Winkler Foundation option must be solved in NIKE3D with the direct solver (see Linear Solvers). Selecting the Winkler Foundation option in the automatic mesh generation program automatically causes the NIKE3D direct solver FISSLE to be invoked at execution time. If the Winkler Foundation option is not selected, then the PCG solver is automatically invoked at execution time.

### SAMPLE FINITE ELEMENT RESULTS

This section presents some typical results from the three-dimensional finite element rigid pavement model. All of the solutions presented in the following section were computed on a Silicon Graphics SGI Indigo<sup>2</sup> work station with 128 megabytes of RAM and 4.5 gigabyte hard disk storage capacity. Solutions were computed in core memory using NIKE3D's Preconditioned Conjugate Gradient (PCG) solver with block diagonal preconditioning. [2] Graphical results were prepared using TAURUS, a postprocessing program developed by the Lawrence Livermore National Laboratory for use with NIKE3D and DYNA3D.

#### ANALYSIS OF B-777 EDGE LOADING.

Edge loading of the six-wheel B-777 main gear was analyzed for the following case: 14-inch PCC slab (25- by 25-ft. slab dimensions), 8-inch stabilized base ( $E = 500,000$  psi), and infinite subgrade ( $E = 15,000$  psi). The pavement used in the analysis is summarized below in table 3. The base layer was assumed continuous (no crack assumed). The load data is given in table 4.

TABLE 3. LAYER PROPERTIES FOR B-777 AND B-727 EDGE LOAD ANALYSES

Variable	PCC Slab	Base Layer (Layer 1)	Subgrade
Young's modulus $E$	$4.0 \cdot 10^6$ psi	$5.0 \cdot 10^5$ psi	$1.5 \cdot 10^4$ psi
Poisson's ratio $\mu$	0.15	0.20	0.40
Thickness	14 in.	8 in.	N.A.
Cutoff depth	N.A.	N.A.	1500 in.
Joint stiffness	100,000 lb./in./in.	N.A.	N.A.

TABLE 4. LOAD DATA FOR SAMPLE FINITE ELEMENT ANALYSES

Aircraft	Gross Weight, lbs.	Percent of Gross Weight on Main Gear	Number of Wheels in Gear	Individual Wheel Load, lbs.	Contact Pressure, psi
B-777	680,000	95	6	53,833	215
B-727	172,000	95	2	40,850	160

The finite element mesh for the B-777 problem was prepared using the automatic mesh generation program described in the previous section. The mesh data are summarized in table 5.

TABLE 5. MESH DATA FOR B-777 EDGE LOAD PROBLEM

Number of Nodes	29,150
Number of Shell Elements	21,982
Number of Solid Elements	4,264
Number of Linear Equations	92,177
Number of Slide Surfaces	6

Run data are reported in appendix A as Test Run No. 30. The solution for this run was found after six equilibrium iterations (i.e., six calls to the PCG solver), and the average number of iterations required for convergence of the PCG phase was 1,450. Hence, the total number of iterations in the solution (number of PCG calls times average iterations per PCG call) was 8,700. Total solution time for this run (CPU plus system time) was 34,346 s (9.5 hours), of which 94.9 percent, or 32,609 s (9.1 hours), was spent in the linear equation solver.

Figure 21 shows the computed deflection basin for the B-777 load. In the figure, the six arrows depict the locations of wheel loads for a B-777 landing gear, which is applied to one slab next to the joint shown. Although the solution was computed assuming symmetry on the  $x$ - $z$  plane, the full domain is shown in figure 21 for clarity. As expected, the maximum deflection occurs at the edge of the loaded slab under the center wheel of the tridem arrangement. The maximum deflection predicted by the model for this load case is 0.111 inch. The maximum deflection on the unloaded slab is 0.108 inch. Hence the computed ratio of deflection on the unloaded side of the joint to deflection on the loaded side of the joint ( $\delta_U/\delta_L$ ) is 0.97.

For design purposes, the quantity of greatest interest is the maximum tensile stress occurring on the bottom surface of the PCC slab. Figure 22 is a plot of the principal bending stress in the base of the slab for the B-777 analysis. Distinct stress peaks corresponding to the individual wheels in the gear can be observed clearly in the plot. The maximum principal stress for this case is 428.7 psi, which occurs under the center wheel closest to the edge. The plot confirms that peak stress does not occur directly on the edge of the slab adjacent to the joint. Rather, it occurs at an offset from the edge, in this case approximately 6 inches toward the center of the load patch. The computed maximum stress on the edge, which is less than the peak stress, is 411.1 psi. The maximum stress on the unloaded slab, which does occur at the edge, is 231.0 psi. The computed ratio of maximum stress on the unloaded side of the joint to maximum stress on the loaded side of the joint ( $\sigma_U/\sigma_L$ ) is 0.54.

The above stresses were computed by NIKE3D directly at integration points in the shell elements. NIKE3D returns bending stresses at points on the bottom of the PCC slab directly, based on the Lobatto integration scheme discussed above in the section "Element Types." NIKE3D also computes bending moment resultants for each shell element. The bending moment

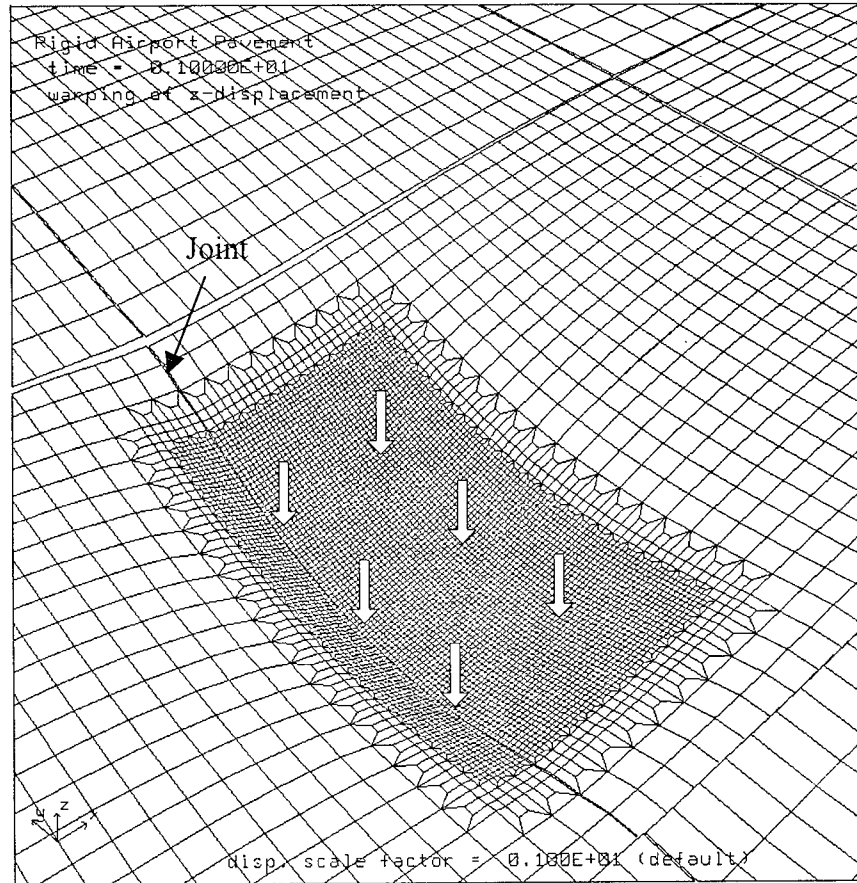


FIGURE 21. VERTICAL DEFLECTION OF PCC SLAB (B-777 EDGE LOAD)

resultants can be used to evaluate the stresses in each element at the extreme fibers in accordance with thin plate theory

$$\sigma_x = \frac{N_x}{t} + \frac{6M_x}{t^2} \quad \sigma_y = \frac{N_y}{t} + \frac{6M_y}{t^2}$$

where  $N_x$ ,  $N_y$  are the normal resultants,  $M_x$ ,  $M_y$  are the bending moment resultants, and  $t$  is the plate thickness. Normally, the element stresses computed from moment resultants will be close to the stresses computed directly at the Lobatto integration points. However, they will not agree exactly due to the fact that the NIKE3D shell element does not assume a linear variation of stress through the shell thickness, as implied by the above plate bending equations. As an illustration, the maximum bending stress on the bottom surface of the PCC slab computed from the moment resultants is 434.3 psi, compared to 428.7 psi computed directly at the integration point (a difference of 1.3 percent). Stress plots drawn by the TAURUS program (e.g., figure 22) are based on the moment resultants.



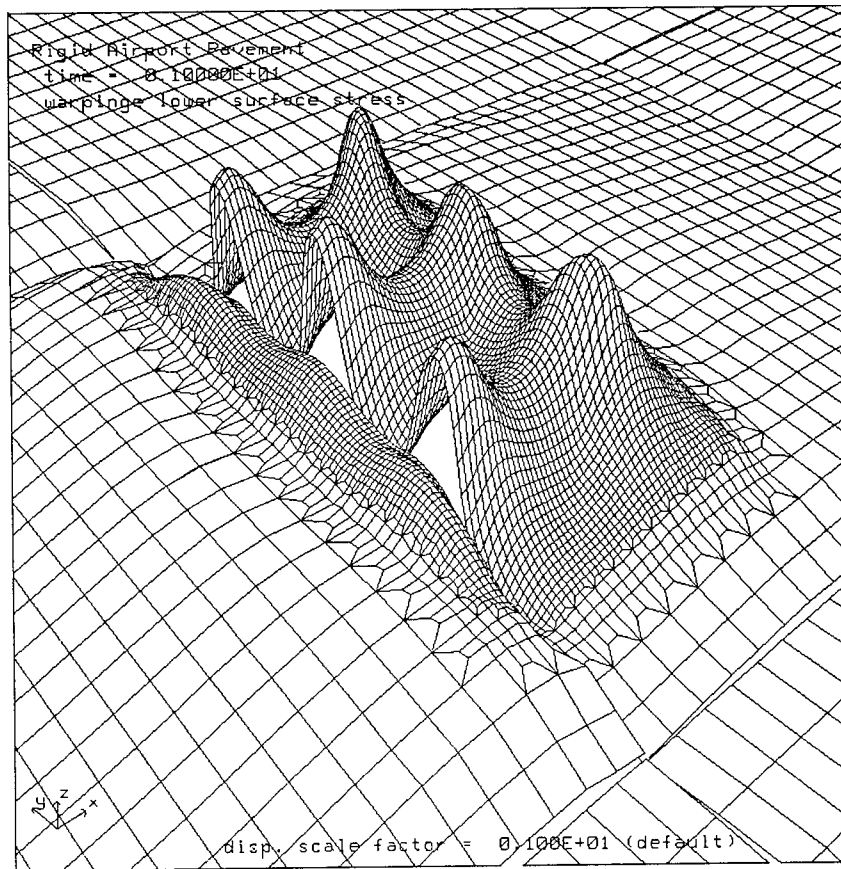


FIGURE 22. PRINCIPAL BENDING STRESS IN BOTTOM OF PCC SLAB  
(B-777 EDGE LOAD)

For edge loading, the principal bending stress coincides with the stress in the direction parallel to the joint ( $\sigma_y$  in this analysis). The bending stress normal to the joint ( $\sigma_x$ ) is theoretically zero at the edge of the slab, since the joints are not designed to transmit any moments. At points away from the joint,  $\sigma_{xx}$  is not zero in general, so the principal stress has to be computed for those points.

Figure 23 shows the distribution of principal strain in the bottom of the PCC slab. The distribution is similar to that for principal stress (figure 22), but while the stress is fairly evenly distributed among all six wheels, a greater distribution of strain to the three wheels along the slab edge is noted. As is the case with the stress, the maximum principal strain does not occur immediately at the slab edge but closer to the center of the wheel.

Figure 24 shows the distribution of vertical stress in the top of the subgrade layer. As expected, the vertical stress is concentrated under the joint. Numerical results for the B-777 finite element analysis are summarized in table 6.

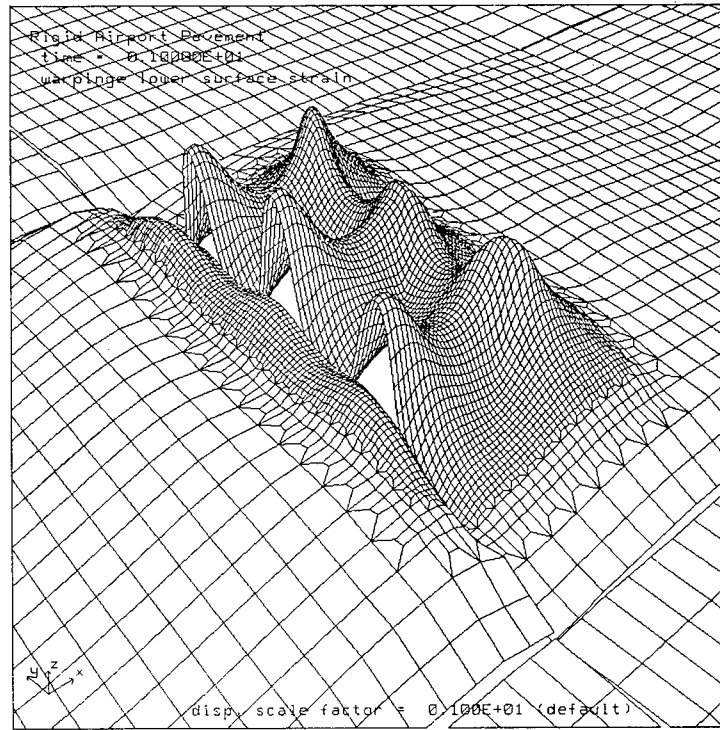


FIGURE 23. PRINCIPAL STRAIN IN BOTTOM OF PCC SLAB (B-777 EDGE LOAD)

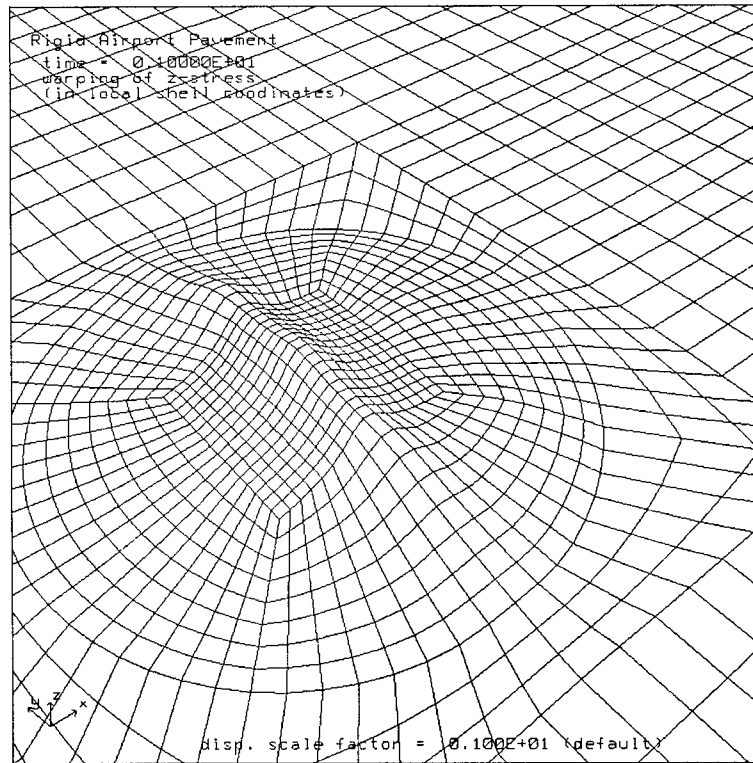


FIGURE 24. VERTICAL STRESS IN TOP OF SUBGRADE LAYER (B-777 EDGE LOAD)

TABLE 6. SUMMARY OF RESULTS OF FINITE ELEMENT ANALYSIS  
(B-777 EDGE LOAD)

	Computed at Integration Points	Based on Moment Resultants
Maximum principal stress, loaded slab (psi)	428.7	434.3
Maximum edge stress, loaded slab (psi)	411.1	423.6
Maximum edge stress, unloaded slab (psi)	231.0	224.0
Maximum deflection, loaded slab (in.)	0.111	0.111
Maximum deflection, unloaded slab (in.)	0.108	0.108
$\sigma_U / \sigma_L$	0.54	0.52
$\delta_U / \delta_L$	0.97	0.97

In the above finite element analysis, only a small amount of separation was observed between the slab and base layer on the unloaded side of the joint. This is due to the relatively high stiffness of the joint ( $k_{joint} = 100,000$  lbs./in./in.). As the joint stiffness is decreased, the separation of the slab and base layer increases. Figure 25 shows in detail the separation of the unloaded slab from the base course for the case  $k_{joint} = 10,000$  lbs./in./in. The other properties are as given in table 3. For greater clarity the vertical deflection has been exaggerated by a factor of 500 and the joint elements are not shown.

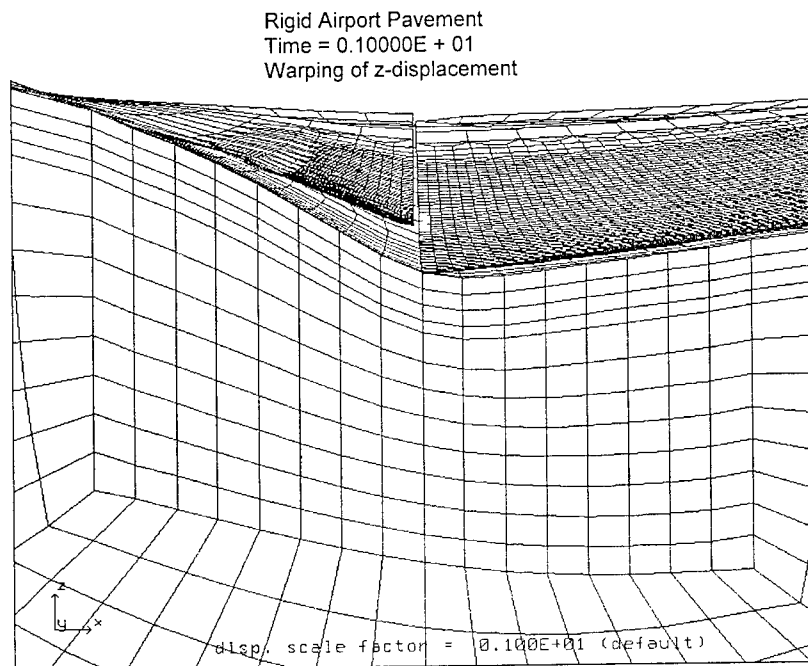


FIGURE 25. SLAB-BASE SEPARATION AT JOINT (B-777 EDGE LOAD)

## ANALYSIS OF B-727 EDGE LOADING.

A second numerical example involves edge loading by the dual-wheel B-727 main gear. The pavement properties listed in table 3 were also used in the B-727 analysis. Load data are given in table 4. The mesh data for the B-727 analysis are summarized in table 7.

TABLE 7. MESH DATA FOR B-727 EDGE LOAD PROBLEM

Number of Nodes	27,334
Number of Shell Elements	21,958
Number of Solid Elements	2,523
Number of Linear Equations	83,301
Number of Slide Surfaces	6

Run data are reported in appendix A as Test Run No. 49. The solution for this run was found after six equilibrium iterations (i.e., six calls to the PCG solver), and the average number of iterations required for convergence of the PCG phase was 1,176. Hence, the total number of iterations in the solution (number of PCG calls times average iterations per PCG call) was 7,056. Total solution time for this run (CPU plus system time) was 24,990 s (6.9 hours), of which 92.5 percent, or 23,124 s (6.4 hours), was spent in the linear equation solver. TAURUS plots of vertical deflection of the slab surface and principal bending stress in the bottom of the PCC slab due to the B-727 load are presented in figures 26 and 27. Numerical results for the B-727 finite element analysis are summarized in table 8.

TABLE 8. SUMMARY OF RESULTS OF FINITE ELEMENT ANALYSIS  
(B-727 EDGE LOAD)

	Computed at Integration Points	Based on Moment Resultants
Maximum principal stress, loaded slab (psi)	400.7	405.2
Maximum edge stress, Loaded slab (psi)	387.6	398.4
Maximum edge stress, Unloaded slab (psi)	188.2	182.0
Maximum deflection, Loaded slab (in.)	0.0386	0.111
Maximum deflection, Unloaded slab (in.)	0.0358	0.108
$\sigma_U / \sigma_L$	0.47	0.45
$\delta_U / \delta_L$	0.93	0.97

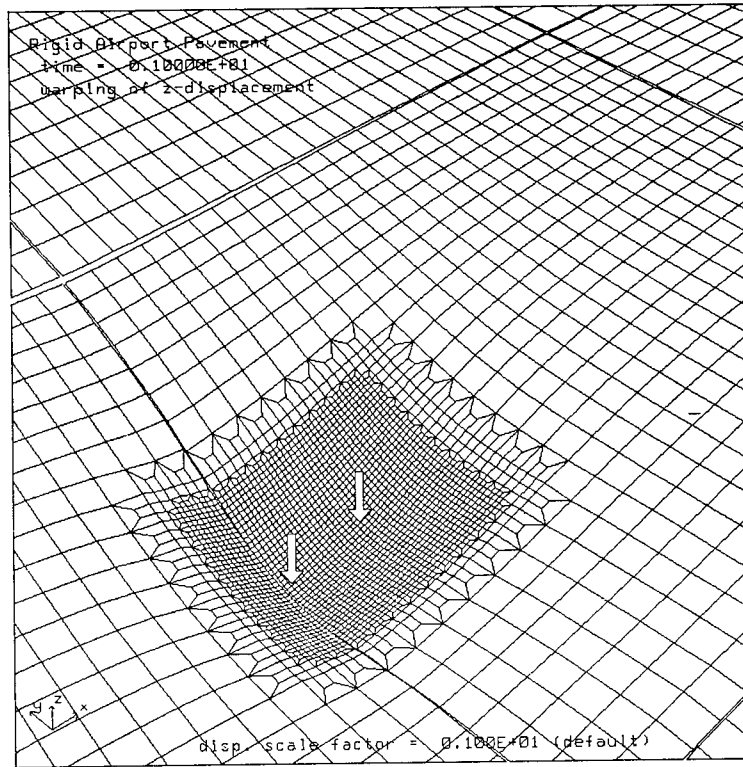


FIGURE 26. VERTICAL DEFLECTION OF PCC SLAB (B-727 EDGE LOAD)

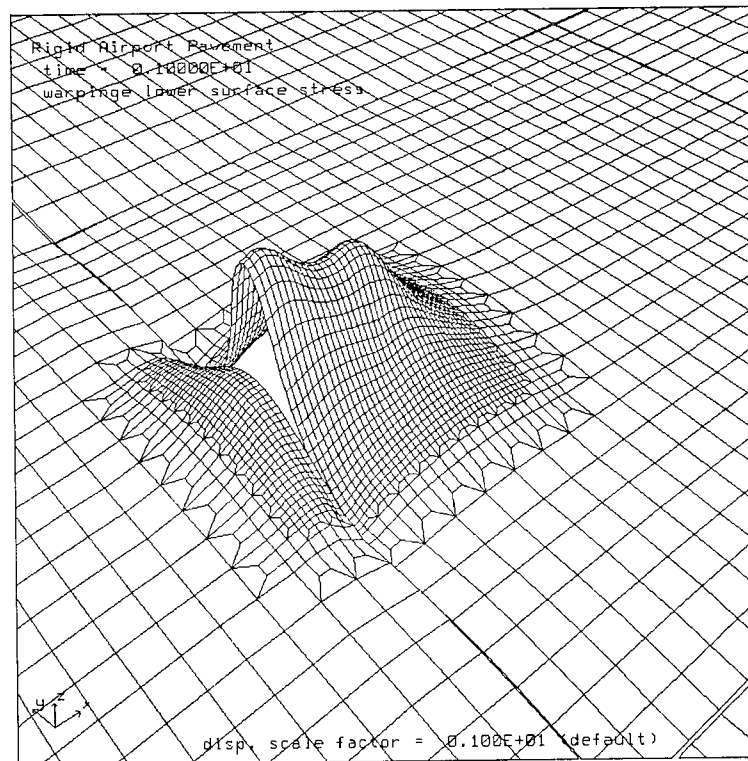


FIGURE 27. PRINCIPAL BENDING STRESS IN BOTTOM OF PCC SLAB (B-727 EDGE LOAD)

### ANALYSIS OF B-777 INTERIOR LOADING.

A third numerical example analyzes interior loading by the twin-tridem B-777 main gear. The pavement properties listed in table 3 were also used in the analysis. Load data is given in table 4. The mesh data for the B-777 interior analysis are summarized in table 9.

TABLE 9. MESH DATA FOR B-777 INTERIOR LOAD PROBLEM

Number of Nodes	10,408
Number of Shell Elements	1,998
Number of Solid Elements	7,075
Number of Linear Equations	33,316
Number of Slide Surfaces	4

Run data are reported in appendix A as Test Run No. 21. The solution for this run was found after six equilibrium iterations (i.e., six calls to the PCG solver), and the average number of iterations required for convergence of the PCG phase was 1,402. Hence, the total number of iterations in the solution (number of PCG calls times average iterations per PCG call) was 8,412. Total solution time for this run (CPU plus system time) was 12,109 s (3.4 hours), of which 95.2 percent, or 11,534 s (3.2 hours), was spent in the linear equation solver. TAURUS plots of vertical deflection of the slab surface and principal bending stress in the bottom of the PCC slab due to the B-777 load are presented in figures 28 and 29. Numerical results for the B-777 finite

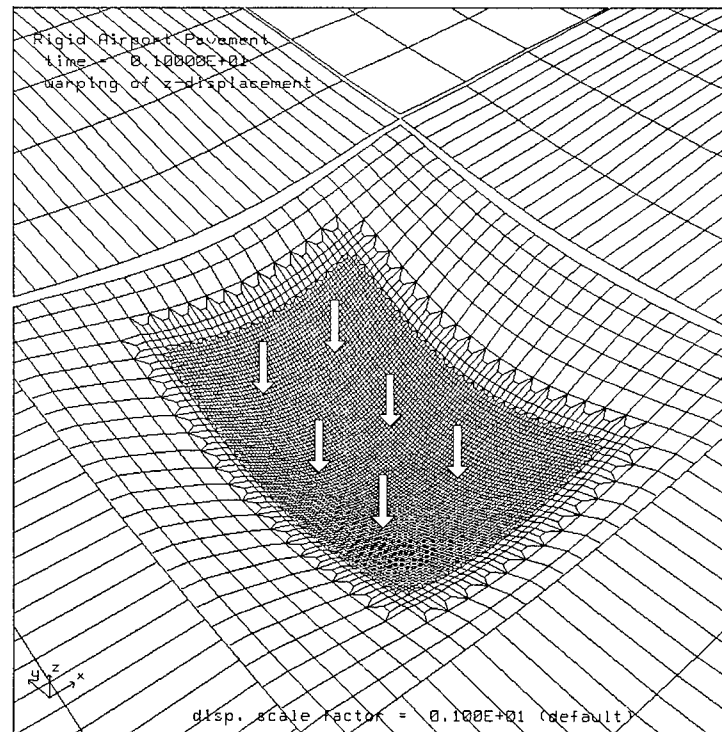


FIGURE 28. VERTICAL DEFLECTION OF PCC SLAB (B-777 INTERIOR LOAD)

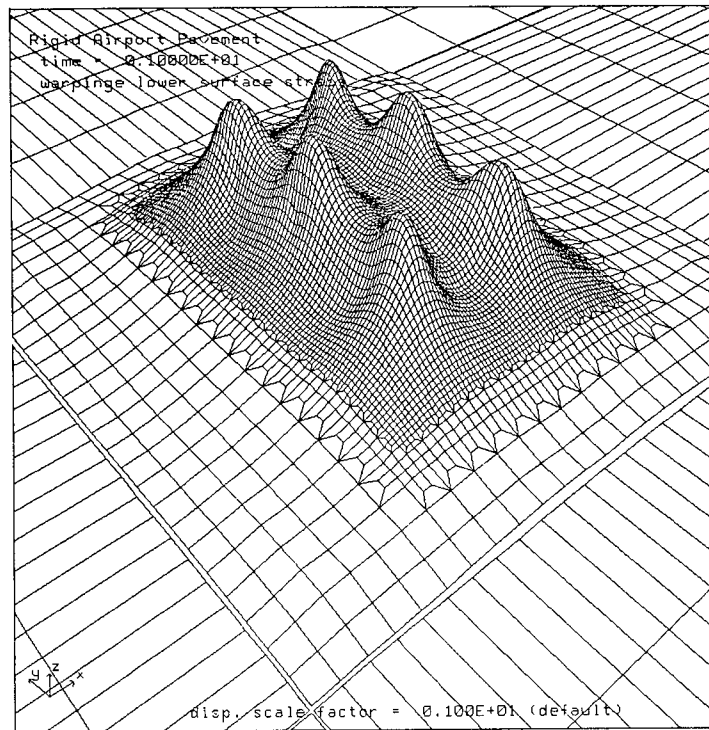


FIGURE 29. PRINCIPAL BENDING STRESS IN BOTTOM OF PCC SLAB  
(B-777 INTERIOR LOAD)

element analysis are summarized in table 10. Comparing table 10 with table 6, a significant result is that the maximum stress due to interior loading exceeds the maximum stress due to edge loading for the B-777.

TABLE 10. SUMMARY OF RESULTS OF FINITE ELEMENT ANALYSIS  
(B-777 INTERIOR LOAD)

	Computed at Integration Points	Based on Moment Resultants
Maximum principal stress (psi)	493.6	492.8
Maximum stress in x-direction (psi)	493.6	492.8
Maximum stress in y-direction (psi)	388.3	388.0
Maximum deflection (in.)	0.100	0.100

### MODEL SENSITIVITY ANALYSIS

#### IDENTIFICATION OF VARIABLES FOR SENSITIVITY ANALYSIS.

The model sensitivity analysis considered two types of variables. In the first category were variables, such as the mesh density, that affect the response of the numerical model, but do not affect the response of the idealized physical system being analyzed. The second category

contained variables, including pavement structural properties, which affect both the idealized pavement response and the numerical solution. Examples of the two types of variables are listed in table 11.

TABLE 11. VARIABLES AFFECTING MODEL RESPONSE

Type 1 Variables	Type 2 Variables
2D Mesh Density 3D Mesh Density Discretized Subgrade Cutoff Depth Boundary Constraints Interface Penalty Scale Factor	<u>Quantitative</u> Load Magnitude Slab Thickness Base Layer Thickness Base Layer Modulus Subgrade Modulus Joint Stiffness  <u>Qualitative</u> Load Geometry Presence of Subbase Layer Presence of Crack in Base Layer

In general, Type 1 variables have a computational cost associated with them. For example, increasing the subgrade cutoff depth adds additional layers of elements to the mesh, thereby increasing the solution time. The goal of the analysis was therefore to identify the minimum cutoff depth consistent with an accurate solution; i.e., a solution acceptably close to the theoretical solution for an infinitely deep subgrade. Similarly, higher mesh densities add significantly to the numerical solution time, hence an effort was made to find the minimum mesh density consistent with an accurate numerical solution.

Type 2 variables may or may not have a computational cost associated with them. However, the goal of the analysis was not to minimize the cost associated with Type 2 variables, but merely to quantify the dependence of the numerical solution on these variables. Using data from this analysis, the sensitivity of the finite element solution to a variable such as subgrade elastic modulus can be compared to the sensitivity of other methods of solution (e.g., layered elastic) to the same variable. Thus, the data collected in the sensitivity analysis phase of this project may facilitate a more general comparison between computational methods.

#### BENCHMARK RESPONSE FOR ANALYSIS.

The response of a rigid pavement to a given static loading can be measured in a number of different ways. Possible benchmark responses are the maximum deflection of the slab surface under load, the compressive stress in the subbase layers, or the bending stress in the slab. For design purposes the most useful measurement is the maximum bending stress occurring at the bottom of the slab. Therefore, the maximum (tensile) bending stress in the extreme fibers of the slab is used as the reference response for all analyses and comparisons in this report, except where otherwise noted.



### EFFECT OF FINE MESH DENSITY.

A series of test runs was performed to assess the influence of the 2D mesh density on the computed critical stress. Higher mesh densities yield more accurate numerical solutions, but solution times and storage requirements increase rapidly with the number of elements. Table 12 summarizes the test runs for 2D mesh density. Based on the results in table 12, a maximum element side length of 2.083 inches in the fine mesh region was used since it yields the computed critical stress with acceptable numerical accuracy of less than 0.4%.

TABLE 12. EFFECT OF FINITE ELEMENT MESH DENSITY (SLAB MESH)

Element Side Length, in.	Number of 2D Elements	Run Time, hrs.	Critical Stress, psi
4.167	343	0.5	94.450
2.778	510	0.9	95.906
2.083	781	1.1	97.218
1.667	1110	1.3	97.596
Layer Properties: 14-in. PCC Slab, $E = 4,000,000$ psi, $\mu = 0.15$ No Base Layer Infinite Subgrade, $E = 15,000$ psi, $\mu = 0.15$		Load: Single-Wheel Load (Interior Load) Gross Weight = 30,000 lbs. Wheel Load = 14,250 lbs. Tire Pressure = 75 psi	

### EFFECT OF SUBGRADE CUTOFF DEPTH.

The assumption that for design purposes the rigid pavement subgrade extends to infinity presents a special problem for the finite element analysis. While in theory the subgrade layer can be extended to any arbitrary (finite) depth in order to approximate the infinite case, in practice it is desirable to limit the number of 3D elements by minimizing the depth of the subgrade layer included in the computational domain. The target cutoff depth is thus the minimum subgrade layer depth for which the computed response is virtually equal to the response for the infinite subgrade case. "Virtually equal" means that very small errors, say less than one tenth of one percent of the computed stress, are neglected.

The target cutoff depth was established for a range of load types and pavement sections. The procedure was to perform repeated finite element test runs in which the subgrade depth was varied while all other analysis variables were held constant. The minimum subgrade cutoff depth in the test runs was 300 inches. In each series of test runs the cutoff depth was first increased to 420 inches then increased in subsequent runs by increments of 360 inches until further increases did not yield significant changes in the computed value of the critical stress. The final value thus obtained was taken as the value for the infinite subgrade case.

Results of the test runs are shown in figure 30, and the properties for the test series are shown in table 13. For each series of test runs, the normalized response was obtained by dividing the computed stress for a particular run by the stress for the infinite subgrade case (i.e., the stress for

the final run in the series). From figure 30 it is apparent that the load case (edge versus interior) has a relatively minor influence on the required cutoff depth, while the effect of other factors, such as the gear type and the subgrade modulus, is more significant. Comparing series D and E, it is seen that the higher subgrade modulus results in the higher normalized stress, for the same cutoff depth (cf. Series D and E). Likewise, the heavier aircraft gear produces the lower normalized stress for the same cutoff depth (cf. Series A and C). It was also found that the presence of a high-stiffness base layer did not significantly affect the cutoff depth (cf. series A and B).

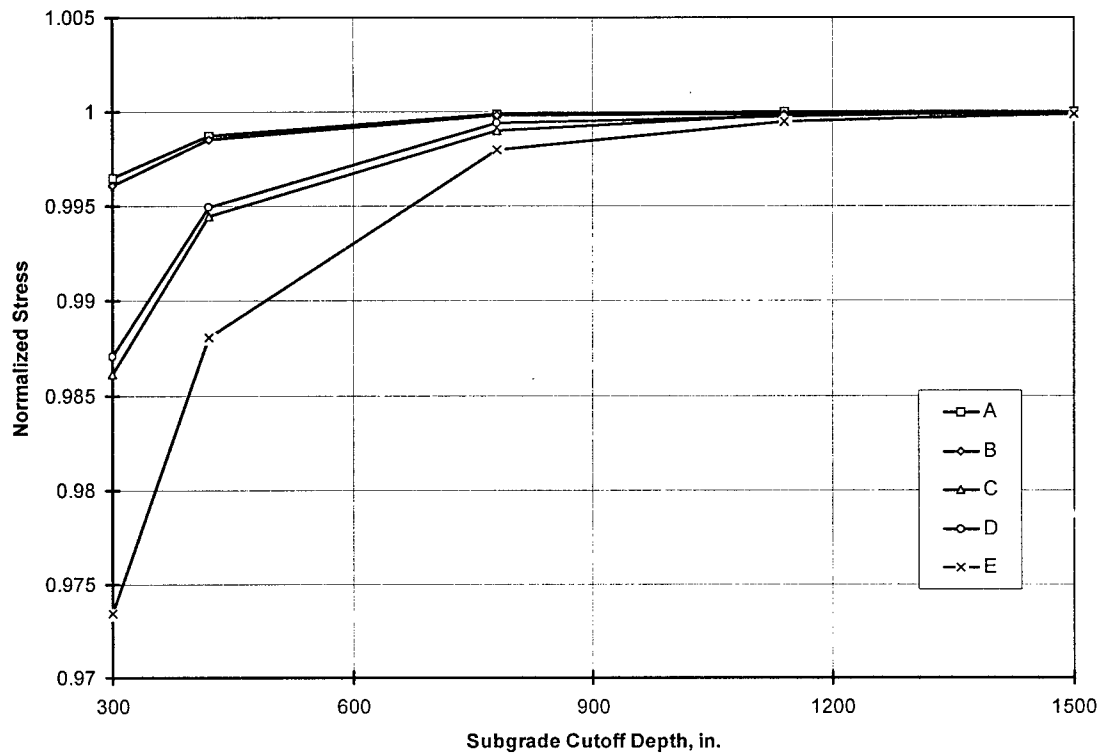


FIGURE 30. COMPUTED CRITICAL STRESS (NORMALIZED) AS A FUNCTION OF SUBGRADE CUTOFF DEPTH

TABLE 13. PROPERTIES FOR TEST SERIES IN FIGURE 30

Series	Aircraft-GVW	Load Case	PCC Slab	Stabilized Base	Subgrade
A	SWL-30	Interior	14 inches	none	15000 psi
B	SWL-30	Interior	14 inches	8 inches	15000 psi
C	B-777-680	Interior	14 inches	none	15000 psi
D	B-777-680	Edge	14 inches	8 inches	15000 psi
E	B-777-680	Interior	16 inches	8 inches	4500 psi

Of the five series shown in figure 30, the most critical case is Series E (B-777 load and  $E_{sg} = 4500$  psi). Even for this worst case, it is seen that a subgrade cutoff depth of only 300 inches gives a value of critical stress in the slab that is greater than 97 percent of the assumed infinite subgrade case. When the subgrade cutoff depth is increased to 1140 inches, the variation from the infinite case is less than 0.1% for all the series. Based on these results, it is felt that a basic cutoff depth of 1140 inches provides sufficient accuracy for the model. Indeed, a smaller cutoff depth, say 720 inches could be justified for single-wheel aircraft loads based on figure 30. Except as otherwise noted, all of the numerical results presented in this report are based on a cutoff depth of 1500 inches, so the influence of the cutoff depth on the results presented below can be considered negligible.

### EFFECT OF BOUNDARY NODAL CONSTRAINTS.

The type of constraint imposed on the nodes along the slab edges can affect the computed response. The simplest approach is to assume that the slab edges at the boundary of the model are free of constraints. This approach is consistent with the situation at the edge of a runway, for example, where the slab edge is unconstrained and is free to rotate or translate. For a nine-slab model intended to analyze a larger continuous system of jointed slabs, where the boundary of the model does not necessarily correspond to a free edge, additional constraints can be imposed at the boundary edges to approximate the partial constraints provided by joints in the physical pavement. Provided the boundary edges are at a sufficient distance from the load, the difference in computed stress between the case with unconstrained boundaries and the constrained boundary case will be relatively small.

In the current nine-slab model, the effect of varying the nodal constraints at the boundary was analyzed by comparing the results from two similar test runs. In the first test run, all of the slab edge nodes were unconstrained. The second test run was identical to the first, except that nodes on the slab along the edges  $y = \pm 451$  in. were subject to the rotational constraint  $\theta_x = 0$  (i.e., rotations about the  $x$ -axis were suppressed). In both cases the edges at  $x = -451$  in. and  $x = 451$  in. were unconstrained. Locations of the constrained nodes are shown in figure 31. From a practical viewpoint, the no constraints case represents a lower bound, complete suppression of rotation of an upper bound, and the partial constraint is provided by real joints.

A third run was planned in which vertical translation of the edge nodes was suppressed in addition to the  $x$ -axis rotational degree of freedom. However, it was found that imposition of this constraint caused numerical problems with respect to the sliding interface between the slab and base. Specifically, if vertical movement of the slab is suppressed, this leads to singularity of the stiffness matrix. Therefore, the full fixity case was not examined.

Table 14 compares results for the two test cases. Computed peak stresses and deflections at the load are compared, as well as moment reactions at the zeroed degrees of freedom. From table 14, it is seen that the effect of the rotational edge constraint on computed critical stress is minor. There is a reduction of 1.5 percent in the computed value of critical stress for the edge case and no significant effect for the interior case.

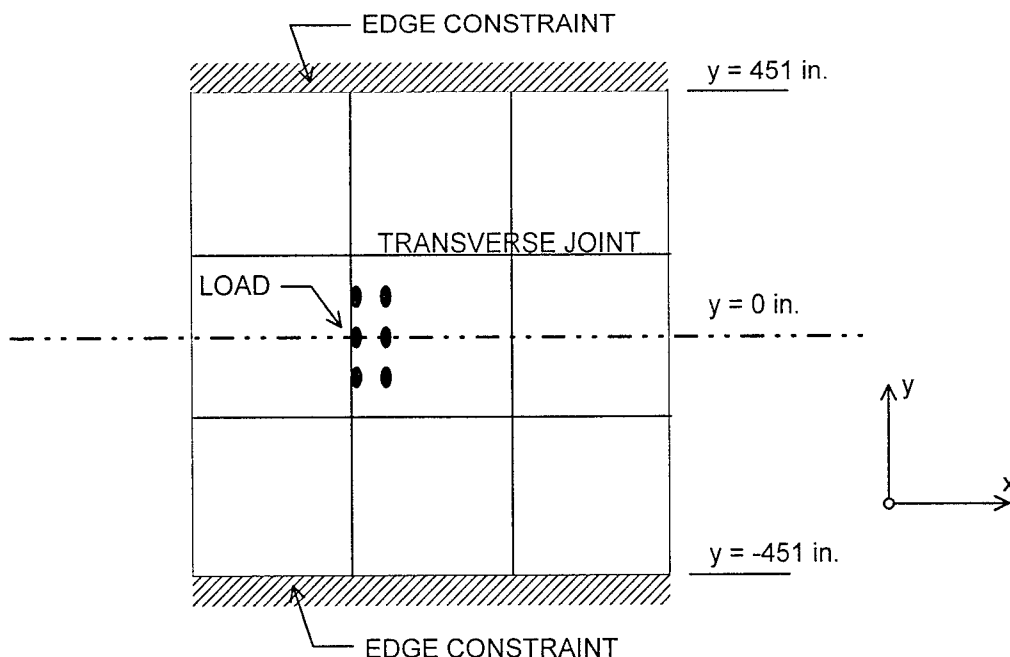


FIGURE 31. BOUNDARY CONSTRAINTS FOR TEST PROBLEM (EDGE LOAD CASE)

TABLE 14. EDGE CONSTRAINT COMPARISON

	Test Case 1 No Constraints		Test Case 2 Rotational Constraint ( $\theta_x = 0$ )	
	Edge	Interior	Edge	Interior
Maximum bending stress, bottom of slab (psi)	428.6	493.6	422.3	493.6
Maximum deflection (inches)	0.109	0.100	0.111	0.100
Total bending moment reaction (lb.-in.)	0	0	$9.70 \times 10^5$	$1.07 \times 10^6$
Properties: 14-in. PCC Slab, $E = 4,000,000$ psi, $\mu = 0.15$ 8-in. Base, $E = 500,000$ psi, $\mu = 0.20$ Infinite Subgrade, $E = 15,000$ psi, $\mu = 0.40$ Joints: $k_{joint} = 100,000$ lbs./in./in.			Load: B-777, GVW = 680,000 lbs. Wheel Load = 53,833 lbs. Tire Pressure = 215 psi	

#### JOINT STIFFNESS AND JOINT EFFICIENCY.

The efficiency of load transfer from the loaded to the unloaded slab is controlled in the 3D model by adjusting the elastic stiffness  $k_{joint}$  assigned to the joint material. Increasing the value of  $k_{joint}$  stiffens the joint and causes more of the response to be distributed to the unloaded slab, thereby decreasing the critical stress in the loaded slab.

Two common and useful ways of reporting the load transfer efficiency are as (1) the ratio of maximum stress in the unloaded slab to maximum stress in the loaded slab ( $\sigma_U/\sigma_L$ ) or (2) the ratio of maximum vertical deflection of a point in the unloaded slab to maximum vertical deflection of a point in the loaded slab ( $\delta_U/\delta_L$ ). Generally,  $\delta_U/\delta_L$  is greater than  $\sigma_U/\sigma_L$  for a given joint. Table 15 lists values of  $k_{joint}$ ,  $\sigma_U/\sigma_L$ ,  $\delta_U/\delta_L$ , and critical stress for the model where the load is a B-777 main gear (680,000 lbs. GVW) and the pavement section properties are as indicated in table 15.

TABLE 15. EFFECT OF JOINT STIFFNESS  $k_{joint}$  ON COMPUTED RESPONSE

$k_{joint}$ , lbs./in./in.	$\sigma_U/\sigma_L$	$\delta_U/\delta_L$	Critical Stress, psi	Number of CG Calls
$1 \times 10^3$	*	*	*	30
$1 \times 10^4$	0.45	0.90	445.6	21
$5 \times 10^4$	0.50	0.95	435.5	11
$7.5 \times 10^4$	0.51	0.95	434.8	7
$1 \times 10^5$	0.54	0.97	428.7	6
$2 \times 10^5$	0.61	0.98	412.2	4
Section Properties: <span style="float: right;">*Process failed to converge after 30 CG calls</span> 14-in. PCC Slab ( $E = 4,000,000$ psi, $\mu = 0.15$ ) 8-in. Base, monolithic ( $E = 500,000$ psi, $\mu = 0.20$ ) Infinite Subgrade ( $E = 15,000$ psi, $\mu = 0.40$ )				

One aspect of the data in table 15 that affects execution times for the model is that, as the joint stiffness parameter is decreased, the number of calls to the conjugate gradients within the NIKE3D solver goes up significantly. Hence the execution times for problems with low  $k_{joint}$  are significantly higher than those for problems with high  $k_{joint}$ . The explanation for this trend is that when the joint stiffness is decreased the separation between the (initially in contact) slab and base layers increases; hence, a larger number of iterations is needed to develop the final equilibrium contact surface

#### EFFECT OF BASE LAYER.

Most rigid airport pavements are constructed with a high-quality base layer under the PCC slab. The effect of the stabilized base layer on the pavement response is highly complex and not well understood. The FAA design method based on the Westergaard solution assumes that the stabilized base layer provides an increase in foundation support that is reflected in a higher  $k$  value. When a stabilized layer is present, the  $k$  value used for design is the probable  $k$  value at the top of the stabilized layer, determined from figure 3-16 of AC 150/5320-6D. The "top of subbase  $k$ " approach, although convenient, is theoretically unsatisfactory. It attributes 100% of the structural benefit from the stabilized base to higher foundation stiffness and fails to consider other possible sources of structural benefit, for example the connection between a stiffened base layer and improved joint performance.

TEST RUNS USING B-777 LOAD. Several series of test runs were performed to analyze the effect of the stabilized subbase layer on the model response. In each series of runs the value of the joint stiffness parameter  $k_{joint}$  was varied in the range 10,000-200,000 lbs./in./in while the other layer properties were unchanged. Results were analyzed for the following three series:

Series 1: 14-in. PCC slab directly on subgrade with no base.

Series 2: 14-in. PCC slab with 8" stabilized base ( $E = 500,000$  psi,  $\mu = 0.20$ ) - monolithic.

Series 3: Same as series 2, except that the stabilized base is assumed cracked under the joint.

In the last test series, the crack was assumed to be vertical and parallel to the joint and running directly beneath the joint. The crack extends through the whole depth of the base layer but does not extend into the subgrade. Furthermore, the crack plane is modeled as a shear-free sliding surface; i.e., no spring stiffness or frictional coefficient was assumed for the interface. In all three series the loading aircraft was a B-777 with a gross vehicle weight of 680,000 lbs. The properties of the subgrade were  $E = 15,000$  psi and  $\mu = 0.40$ .

The results of the analysis are shown in figures 32 through 35. In figure 32, the critical stress in the bottom of the PCC slab is plotted as a function of  $k_{joint}$  for all three cases. The critical stress is the maximum principal stress computed from moment resultants (see page 37). The joint efficiencies,  $\sigma_U/\sigma_L$  and  $\delta_U/\delta_L$ , are plotted as functions of  $k_{joint}$  in figures 33 and 34 respectively. The percentage of load transfer, plotted in figure 35 as a function of  $k_{joint}$ , is computed approximately as the ratio of  $\sigma_L$  to  $(\sigma_U + \sigma_L)$ , where the latter sum is assumed to represent the stress for a hypothetical free edge.

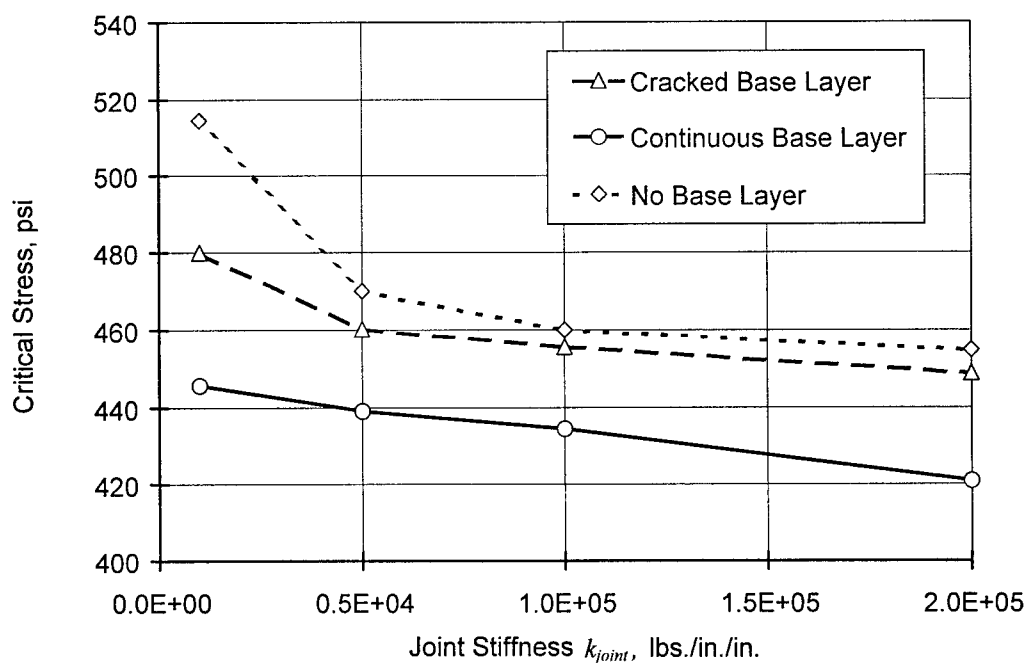


FIGURE 32. EFFECT OF STABILIZED BASE ON CRITICAL STRESS IN PCC SLAB (B-777 EDGE LOAD)

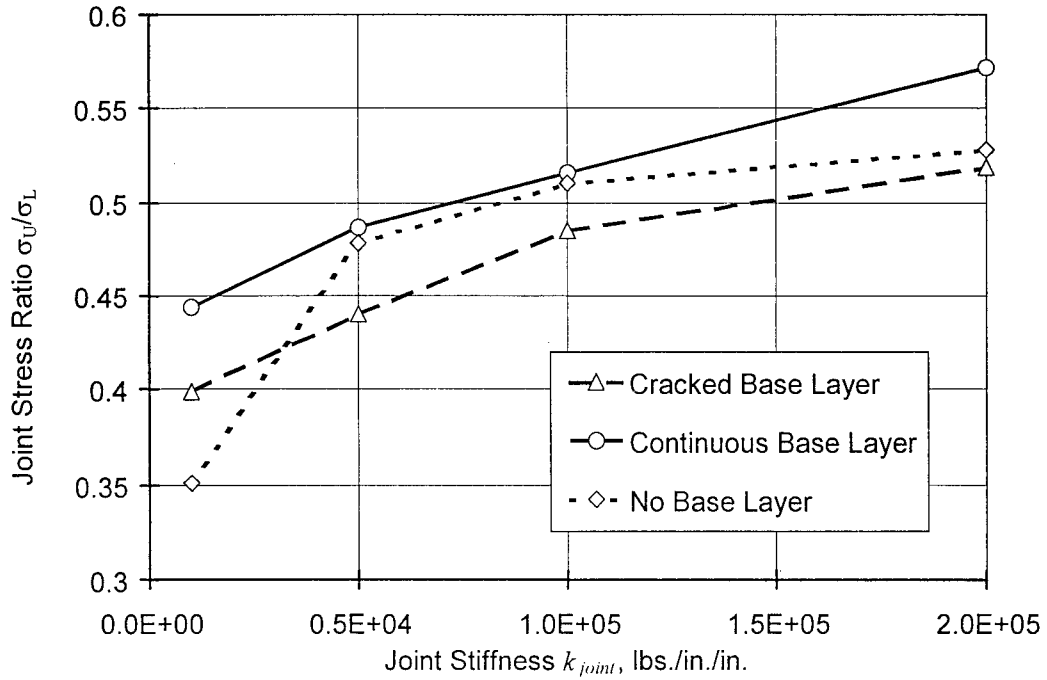


FIGURE 33. EFFECT OF STABILIZED BASE ON THE RATIO OF MAXIMUM STRESS IN THE UNLOADED SLAB TO MAXIMUM STRESS IN THE LOADED SLAB (B-777 EDGE LOAD)

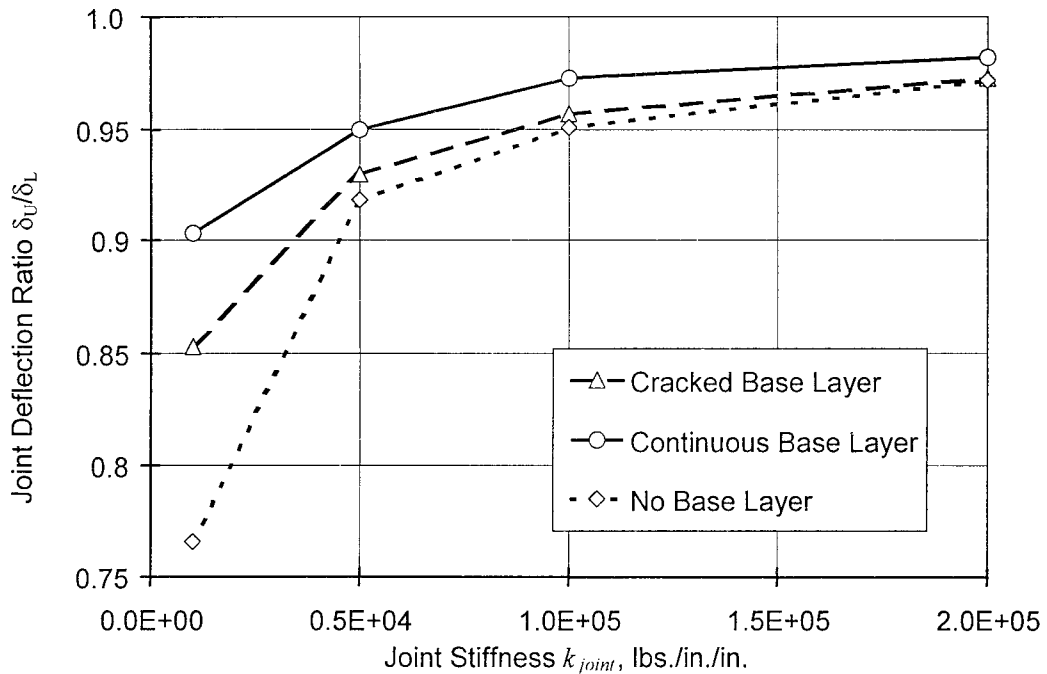


FIGURE 34. EFFECT OF STABILIZED BASE ON THE RATIO OF MAXIMUM DEFLECTION OF THE UNLOADED SLAB TO MAXIMUM DEFLECTION OF THE LOADED SLAB (B-777 EDGE LOAD)

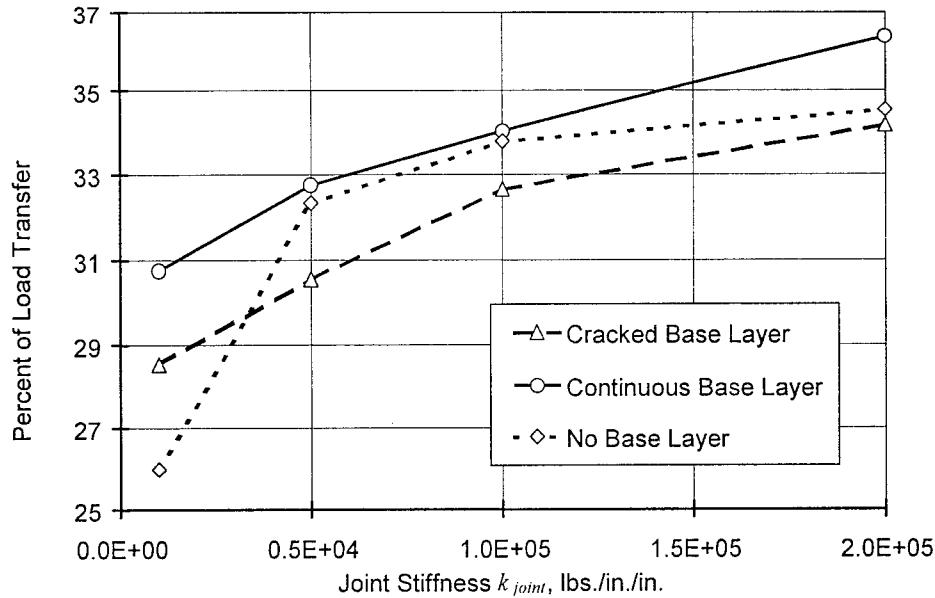


FIGURE 35. EFFECT OF STABILIZED BASE ON PERCENT OF LOAD TRANSFER (B-777 EDGE LOAD)

The results of the finite element test runs confirm that adding a thin, continuous base layer to the structure reduces the critical stress below the case of no base. For edge loading, the amount of stress reduction is substantially reduced when a crack is assumed, indicating that for the uncracked case a large part of the benefit is attributable to additional load transfer in shear through the base. Furthermore, the addition of a stabilized base layer, whether cracked or uncracked, alters the relationship between the linear elastic joint stiffness and the load transfer efficiency for a given loading.

Specific trends identified in figures 32 through 35 are as follows:

1. Critical stress, percent of load transfer,  $\sigma_U/\sigma_L$ , and  $\delta_U/\delta_L$  all depend on the value of  $k_{joint}$ , with the strength of the dependence influenced by the type of base layer. In general, a high-strength base layer causes the pavement response to be less sensitive to changes in the value of  $k_{joint}$ , compared to the case with no base layer. In addition, one effect of the high stiffness base layer is to make the relationship between  $k_{joint}$  and the load transfer more linear.
2. For high values of the assumed joint stiffness  $k_{joint}$ , the computed ratios  $\sigma_U/\sigma_L$  and  $\delta_U/\delta_L$  (figures 33 and 34) for the joint over a cracked base approach those for the case with no base. The ratios for the joint over a monolithic base are somewhat higher.
3. Similarly, for high values of the assumed joint stiffness  $k_{joint}$ , the computed load transfer percentage (figure 35) for the joint over a cracked base approaches that for the case with no base. The load transfer percentage for the joint over a monolithic base is higher.



4. Figure 34 shows that for the cracked base layer, the computed deflection ratio  $\delta_U/\delta_L$  is intermediate between the continuous base layer and no base layer. This is not the case for the stress ratio, as shown in figure 33, where the model predicts higher values of  $\sigma_U/\sigma_L$  for the case with no base layer than for the case with a cracked base layer, for values of  $k_{joint}$  above about 25,000 lbs./in./in. At very low values of  $k_{joint}$ , on the order of 10,000 lbs./in./in., the situation is reversed, with the computed ratio  $\sigma_U/\sigma_L$  higher for the cracked base layer case than for the case with no base layer. The percent of load transfer (figure 35) follows the pattern established by the stress ratio.

Detailed analysis of the finite element stress results shows that another effect of introducing the crack in the base layer is to redistribute the stress under the wheels. Figure 36 shows two distributions of bending stress at the bottom of the PCC slab, both computed for the B-777 main gear and both with identical properties except that one has a cracked base layer. Each peak corresponds to the stress under one of the wheels in the tridem. Not only are the ratios of the local peaks different for the two cases, but for the cracked base layer, the global peak has shifted from the center to the outside wheel. The joint stiffness assumed for figure 36 was  $k_{joint} = 10,000$  lbs./in./in. For higher joint stiffnesses there is less stress redistribution due to the cracked base than for lower joint stiffnesses.

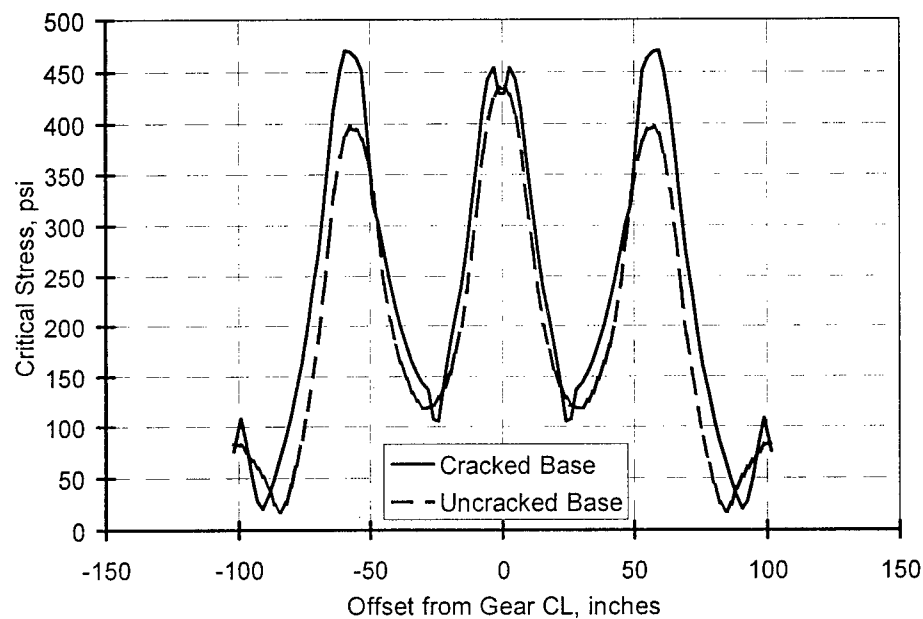


FIGURE 36. COMPARISON OF STRESS DISTRIBUTIONS ALONG SLAB EDGE FOR CRACKED AND CONTINUOUS BASE LAYERS (B-777 LOADING)

TEST RUNS USING B-727 LOAD. A second set of test runs was performed in which a joint over a continuous base layer was compared to a joint over a cracked base layer. In this set of test runs, the pavement layer properties were based on the test runway at Denver International Airport (DIA). The assumed layer properties are listed in appendix A (Layer, Properties Group H). Loading was by a B-727 aircraft (136,500 lbs. gross vehicle weight) oriented perpendicular to the

joint. In the cracked base model, the frictionless crack extended through both the 8-inch-thick cement-treated base (CTB) layer (1,200,000 psi) and the 12-inch-thick lime-stabilized subbase layer (440,000 psi). Once again, it was found that both predicted critical stress and load transfer are strongly affected by the assumed presence of a crack in the high-stiffness layers under the joint. Figure 37 compares the computed critical stress in the bottom of the loaded slab as a function of  $k_{joint}$  for the two cases. Figure 38 compares the percent of load transfer as a function of  $k_{joint}$  for the two cases (where, as for figure 35, the percent of load transfer is calculated approximately by the method above). The computed load transfers from figure 38 are significantly less than the comparable values computed in figure 35 for the B-777 loading.

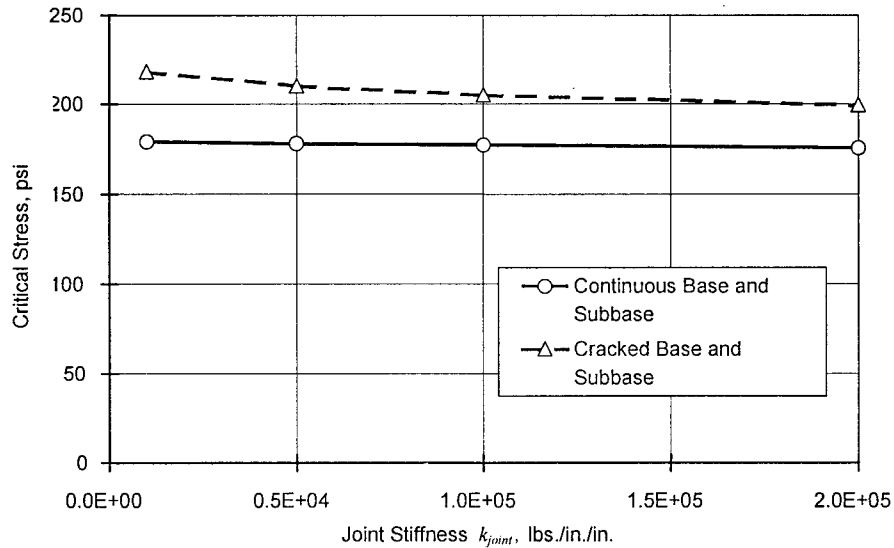


FIGURE 37. EFFECT OF BASE LAYER CRACKING ON CRITICAL STRESS IN PCC SLAB (DIA TEST RUNWAY, B-727 LOAD)

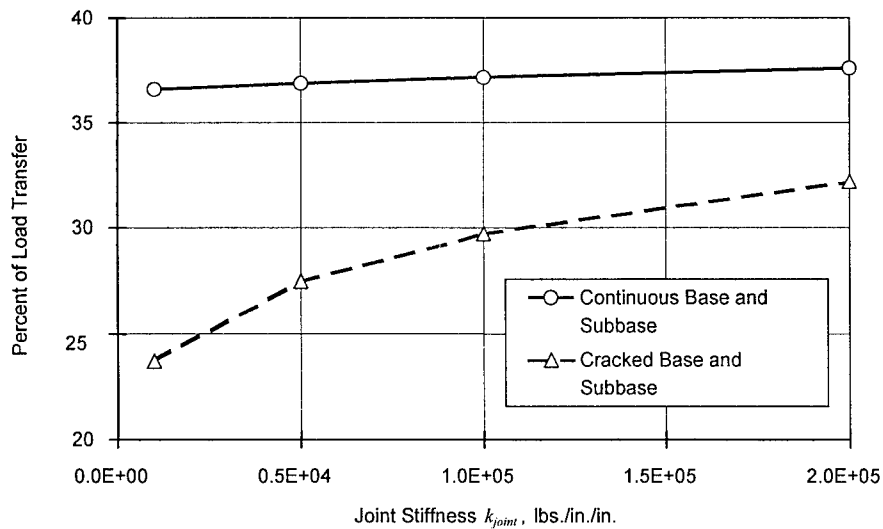


FIGURE 38. EFFECT OF BASE LAYER CRACKING ON PERCENT OF LOAD TRANSFER (DIA TEST RUNWAY, B-727 LOAD)

## EFFECT OF LOAD GEOMETRY.

Load geometry, as well as load magnitude, can influence the computed response. In particular, the computed values of joint ratios  $\sigma_U/\sigma_L$  and  $\delta_U/\delta_L$  can be quite different for loads of the same magnitude but with different numbers of wheels or wheel configurations. The effect of the wheel configuration, independent of the total gear load, is reported in table 16.

TABLE 16. COMPUTED RESPONSES FOR VARIOUS AIRCRAFT LOADS

Load Case	Load Description	Maximum Stress, Bottom of PCC Slab		Joint Efficiency	
		Loaded Slab	Unloaded Slab	Deflection Ratio $\delta_U/\delta_L$	Stress Ratio $\sigma_U/\sigma_L$
A	B-777 (680,000 lb. GVW)	428.7	231.0	0.97	0.54
B	SWL (30,000 lb. GVW)	114.8	45.6	0.90	0.40
C	SWL (680,000 lb. GVW)	2602.9	1026.6	0.90	0.39
D	B-727 (172,000 lb. GVW)	400.7	188.2	0.93	0.47
All load cases: 14-in. PCC ( $E = 4,000,000$ psi, $\mu = 0.15$ ); Slab Dimensions 25 x 25 ft; $k_{joint} = 100,000$ lb./in./in. 8-in. Treated Base Course ( $E = 500,000$ psi, $\mu = 0.20$ ) Subgrade ( $E = 15,000$ psi, $\mu = 0.40$ )					

As shown by the data in table 16, both  $\sigma_U/\sigma_L$  and  $\delta_U/\delta_L$  are significantly increased by the redistribution of the total gear load to six wheels instead of one (Case A to Case C). At the same time, a linear increase in the load magnitude of the single-wheel load (SWL) on the same load patch (Case B to Case C) results only in a proportional increase in the stress response and no significant change in the joint stress and deflection ratios (as expected for a linear elastic system). This numerical result supports the hypothesis that joint efficiency in the field is a function of the loading gear characteristics as well as the joint properties.

## MODEL VALIDATION

### VALIDATION BY COMPARISON TO OTHER COMPUTATIONAL METHODS.

One of the objectives in developing the current finite element model was to ensure that its stress predictions are generally comparable with stress predictions by other commonly used rigid pavement design methods. The other standard methods are the Westergaard method and layered elastic analysis. The Westergaard method is used to calculate design stresses for rigid pavements in FAA Advisory Circular 150/5320-6D [13], and the layered elastic analysis method (as implemented in the program JULEA) is the basis of the LEDFAA design standard. [9] The purpose of the comparisons that follow is to demonstrate that the finite element numerical solutions are reasonable in comparison with these methods, but it is not expected that the three-dimensional finite element model will exactly reproduce the results obtained by either Westergaard analysis or layered elastic analysis for a particular case. On the contrary, both

TABLE 17. COMPARISON OF ANALYSIS METHODS

	Computed Critical Stress, psi			
	(A)	(B)	(C)	(D)
	Finite Element	Finite Element w/Winkler Base	Westergaard	Linear Elastic (JULEA)
Interior Load Case				
SWL (30K GVW) No Base	97.2	100.8	102.1	96.9
SWL (30K GVW) 8-in. Treated Base	93.7	97.6	92.6*	93.3
B-777 (680K GVW) No Base	515.7	537.3	510.7	509.0
B-777 (680K GVW) 8-in. Treated Base	493.6	515.7	443.1*	490.0
* $k$ increased per figure 3-16 of AC 150/5320-6D to account for treated base				
	(A)	(B)	(C)	(D)
	Finite Element	Finite Element W/Winkler Base	Westergaard (FAA)	Linear Elastic (LEDFAA)
Edge Load Case				
SWL (30K GVW) 8-in. Treated Base	114.8	-	139.7*	157.4
B-727 (172K GVW) No Base	434.7	-	523.9	567.7
B-727 (172K GVW) 8-in. Treated Base	400.7	-	456.0*	547.7
B-777 (680K GVW) No Base	451.3	-	582.0	496.1
B-777 (680K GVW) 8-in. Treated Base	428.7	-	427.5*	477.6
All cases: 14-in. slab, $E = 4,000,000$ psi, $\mu = 0.15$ (slab size 25 x 25 ft) Subgrade $E = 15,000$ psi ( $k = 141.385$ pci) $k_{joint} = 100,000$ lbs./in./in. Treated Base: 8 in. thick, $E = 500,000$ psi, $\mu = 0.20$ * $k$ increased per figure 3-16 of AC 150/5320-6D to account for treated base				

Westergaard and LED employ numerous simplifications and assumptions that may cause their solutions to diverge significantly from the more realistic three-dimensional finite element analysis. This is particularly true for complex structures and loadings such as the B-777 edge load case.

Table 17 compares critical stresses calculated for various pavement structures and loadings by four methods. The first method (A) is the three-dimensional finite element model that is the subject of this report. The second method (B) is the alternative three-dimensional finite element model, in which the slab and base layers are discretized using linear finite elements, but the discretized subgrade has been replaced with a Winkler-type spring mat foundation. Solutions for

methods (A) and (B) were found using the NIKE3D program. The third method (C) is the Westergaard method (for interior loads) and the Westergaard/FAA method (for edge loads) as implemented in AC 150/5320-6D and explained below. Westergaard stresses were obtained from the Pickett and Ray stress charts for interior and edge loading. [14] The fourth method (D) is the layered elastic method as implemented by the program LEDFAA. Stresses are computed in LEDFAA using the layered elastic program JULEA.

In the Westergaard method it is assumed that the slab is either infinite (interior load) or semi-infinite (edge load) and that it is continuously supported by a dense liquid (Winkler) foundation. The Winkler foundation is characterized by a single property  $k$ , called the modulus of subgrade reaction. The modulus of subgrade reaction is commonly related to the subgrade Young's modulus  $E_{sg}$  by the following empirical correlation [1, 9]

$$k = \left( \frac{E_{sg}}{26} \right)^{0.7788}$$

Based on the above formula, equivalent values of  $k$  were used in this report for Westergaard stress calculations. The equivalent values used are listed in table 18.

TABLE 18. EQUIVALENT MODULUS OF SUBGRADE REACTION

Subgrade Young's Modulus ( $E_{sg}$ ), psi	Equivalent Modulus of Subgrade Reaction ( $k$ ), pci
4500	55.3
15000	141.4
22500	193.9

Westergaard edge stress analysis yields a value of stress for the free edge case. In order to account for the effects of load transfer, it is necessary to reduce the free edge stress by an amount equal to the stress distributed to the unloaded slab via load transfer devices. Advisory Circular 150/5320-6D specifies the percentage of load transfer as 25 percent. FAA critical edge stresses in table 17 were obtained by reducing the computed Westergaard free edge stress by 25 percent, in accordance with the Advisory Circular.

The FAA design standard specifies that the modulus of subgrade reaction  $k$  should be increased to account for the presence of a strengthened base layer. The amount of the increase is determined by figure 3-16 in AC 150/5320-6D. For the comparisons in table 17, figure 3-16 of AC 150/5320-6D was used to determine the proper value of  $k$  in cases involving a treated base layer, based on the equivalent subgrade  $k$  from table 18.

#### MODEL VALIDATION WITH INSTRUMENTED RUNWAY DATA.

As part of a major FAA-sponsored research project to collect in-service rigid pavement data, an instrumented test pavement was constructed in a section of runway at the Denver International Airport (DIA). A total of 460 sensors were installed to record in situ strains and deflections

caused by commercial aircraft traffic. Operation of the test pavement began in 1996 and is expected to last for 10 years. During that period the DIA will be the primary source of in situ field data for comparison to pavement structural models. The collected data will be stored in a database and made available to the public via the Internet.

An objective of the current project is to compare numerical predictions by the three-dimensional pavement model with the response data collected by the DIA sensors for actual aircraft arrivals and departures. To compare to the finite element model for a given arrival or departure record, three types of information must be known:

1. Wheel path. The track of the aircraft can usually be determined fairly accurately by the response of position strain gauges located near the beginning and end of the test runway section.
2. Aircraft type. The aircraft type can be determined by computing the wheelbase from sensor data.
3. Aircraft gross weight. The gross weight of the aircraft must be known from independent sources. In some cases the gross weights of departing aircraft are known from airline schedules.

PEAK STRAIN COMPARISONS. Initially, strain recorded at the Denver International Airport (DIA) site was compared to strain predicted by the three-dimensional computational model using properties appropriate for the DIA test pavement (table 19).

TABLE 19. DENVER INTERNATIONAL AIRPORT TEST RUNWAY—  
PROPERTIES FOR FINITE ELEMENT ANALYSIS

Property	Value	Source
PCC Slab:		
Young's Modulus $E$	4,410,000 psi	Laboratory Test (6 in. PCC core)
Poisson's Ratio $\mu$	0.22	Laboratory Test (6 in. PCC core)
8-in. Cement-Treated Base (CTB):		
Young's Modulus $E$	1,200,000 psi	HWD Analysis
Poisson's Ratio $\mu$	0.20	Assumed for HWD
12-in. Lime-Stabilized Subbase:		
Young's Modulus $E$	440,000 psi	HWD Analysis
Poisson's Ratio $\mu$	0.25	Assumed for HWD
Silty-Clay Subgrade:		
Young's Modulus $E$	15,000 psi	Lab. Resilient Modulus ( $M_R$ )
Poisson's Ratio $\mu$	0.40	Assumed

To compare the computed strains to the measured strains, the following steps were used:

1. An aircraft departure record was identified for which the above three types of information could be determined.
2. Based on position gauge response data, the approximate track of the aircraft was determined. Then the track of the aircraft was plotted on a map showing the locations of H-Bar strain gauges in the slabs (figure 39). From this plot the approximate offset from the gauges to the wheel centerline could be scaled.
3. For the departure record under consideration, up to ten H-bar strain gauge responses with the highest signal-to-noise ratio were identified. The signals were analyzed automatically using a filtering program. Each of the selected strain gauges was categorized as an edge or an interior gauge and as a top or bottom gauge (near the top or bottom of the PCC slab).
4. Edge and interior finite element analyses were performed using the known gross weight of the aircraft from airline schedules. Analyses were performed using the estimated properties for the DIA pavement shown in table 19. As shown in figure 39, the slab dimensions for the DIA test pavement are 20 by 18.75 feet. For edge load analyses, the orientation of the gear was determined by the type of joint. For transverse joints, the orientation of the gear was perpendicular to the joint. For longitudinal joints, a parallel orientation was used.
5. From the finite element analyses performed in step 4, the distributions of principal strain were computed in the slab on a plane corresponding to the depth of embedment of the H-bar strain gauges. (The depth of embedment of each gauge is known from measurements made at the time of construction. Generally, gauges at the bottom of slabs were placed such that the center of the gauge is located 1 inch from the plane of the bottom of the slab.) Contour plots of computed principal strain in the slab were produced.
6. Using the offsets from the wheel path centerline calculated in step 2, the strain gauges were superimposed on the contour plots produced in step 5. In drawing the strain gauges to scale, it was assumed that they are 6 inches long. The interpolated strain values at each end of the gauge then provided a range of computed strains to be compared with the peak value measured by the strain gauge.

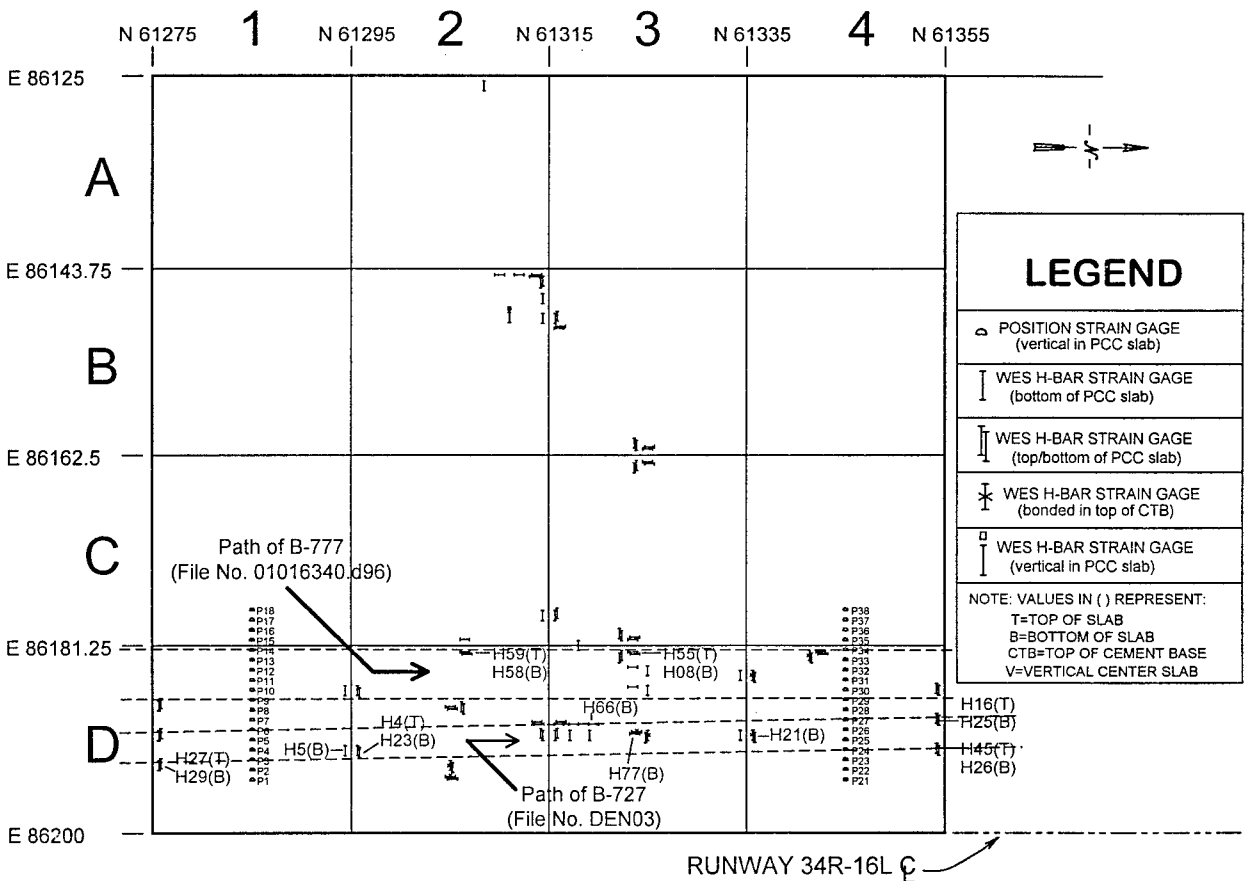


FIGURE 39. STRAIN GAUGE LAYOUT AT DIA TEST RUNWAY

An example of a contour plot of computed strain, with H-bar strain gauges superimposed on it for comparison, is shown in figure 40. The aircraft is a B-777 (data file no. 05617181.d96). Because of current FAA interest in the Boeing B-777, it was decided that some of the initial comparisons would involve that model. To date, only a few comparisons have been made for the B-777 due to the limited availability of aircraft gross weight data. In general, the comparisons made so far indicate good agreement between the recorded and predicted pavement responses. Comparisons also were made for the FAA's B-727 test aircraft, and these likewise indicated good agreement. Table 20 summarizes the peak strain comparisons made to date for B-727 and B-777 aircraft. Table 20 includes strains computed assuming both cracked and continuous base layers, with the assumed joint stiffness  $k_{joint}$  equal to 100,000 lbs./in./in. in all cases. All of the gauges listed in table 20 are located near the slab bottom. Although data file 01016340.d96 in particular indicates some significant discrepancies between measured and predicted values, the discrepancies could be caused by uncertainty as to the exact track of the aircraft gear. (Although the gear was assumed to track straight along the longitudinal joint as shown in figure 39, there may have been some wander.)



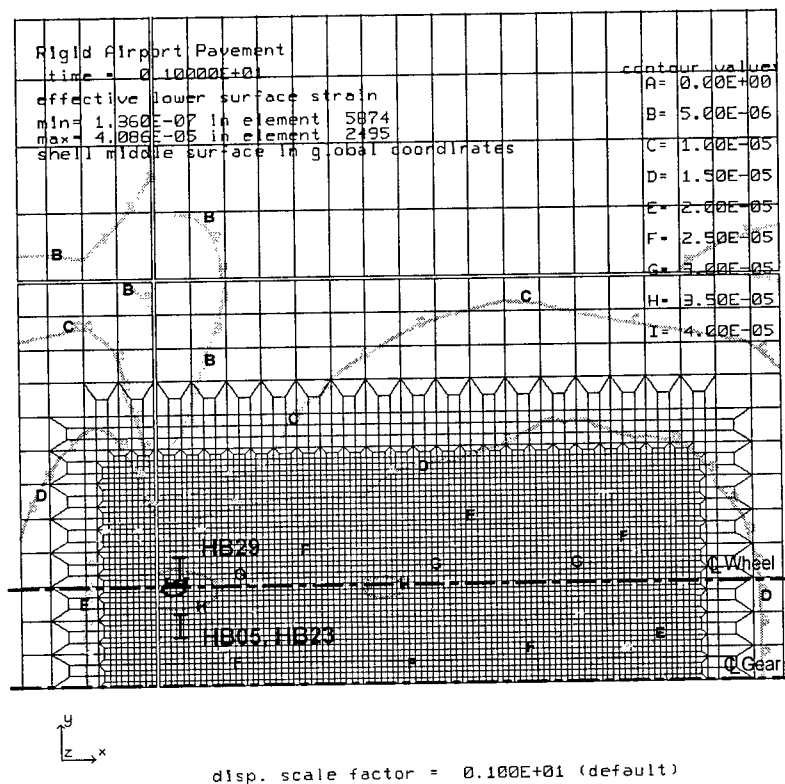


FIGURE 40. DENVER INTERNATIONAL AIRPORT TEST RUNWAY—CONTOURS OF COMPUTED STRAIN IN PCC SLAB AT 1-INCH EMBEDMENT DEPTH (B-777 EDGE LOAD)

TABLE 20. DENVER INTERNATIONAL AIRPORT TEST RUNWAY—STRAIN DUE TO AIRCRAFT LOAD AS RECORDED IN SITU AND AS PREDICTED BY THE THREE-DIMENSIONAL FINITE ELEMENT MODEL

Data File (Aircraft/ Gross Weight)	Sensor	Edge or Interior.	Peak Strain, Microstrains (Sensor Reading)	Predicted Strain Range, Microstrains (3D Finite Element Model)	
				Base Cracked	Base Continuous
DEN03 (B-727/ 136,500 lbs.)	HB05	E	21.89	26.1 – 33.6	21.0 – 25.8
	HB21	E	12.99	20.0 – 23.2	19.1 – 19.8
	HB25	E	22.44	36.3 – 38.6	31.4 – 33.1
	HB26	E	19.51	36.3 – 38.6	31.4 – 33.1
	HB29	E	10.39	36.3 – 38.6	31.4 – 33.1
	HB66	I	14.96	-	29.9 – 30.3
	HB77	I	15.88	-	28.7 – 29.2
05617181.d96 (B-777/ 371,424 lbs.)	HB05	E	32.11	28.4 – 32.6	22.8 – 27.6
	HB23	E	32.59	28.4 – 32.6	22.8 – 27.6
	HB29	E	30.53	24.8 – 25.0	20.2 – 20.3
01016340.d96 (B-777/ 428,351 lbs.)	HB08	E	15.93	-	40.3 – 41.3
	HB58	E	17.41	-	40.3 – 41.3
	-	-	-	-	-

Two additional comparisons were made for the strain distributions in the PCC slab and the deflections at the joint. For strain distribution comparisons it was assumed that the time history of strain provided by the dynamic sensor is approximately analogous to the static distribution of strain in the PCC slab. Thus, by knowing the vehicle speed, the shape of the strain gauge record can be compared to the computed static distribution of strain obtained from the 3D finite element model. However, the assumption that the influence of a moving load on strain at a point is similar to the static strain distribution is theoretically valid only for continuous, linear elastic pavements where the dynamic effects are not dominant. For rigid pavements, where the slabs are separated by non-moment-resisting joints, the dynamic record of strain would not necessarily give a true picture of the static strain distribution. In addition, such phenomena as gapping under the slab, slab uplift ahead of the load, and asymmetric joint response could affect the dynamic strain and cause it to depart from the predicted static distribution.

**STRAIN DISTRIBUTION COMPARISONS.** Figures 41 and 42 compare the computed static distribution of strain along the longitudinal loaded slab edge to the strain recorded at H-bar strain gauges HB08 and HB58, respectively, for data file 01016340.d96 (see figure 39). The computer plot of strain is presented for the case where all layers are assumed monolithic (continuous under the joint). The figures were produced by multiplying the time scale of the dynamic gauges by the vehicle speed evaluated as the gear crosses the gauge to obtain the equivalent distance scale. All strains have been normalized to the peak strain at the center wheel. From figures 41 and 42, the

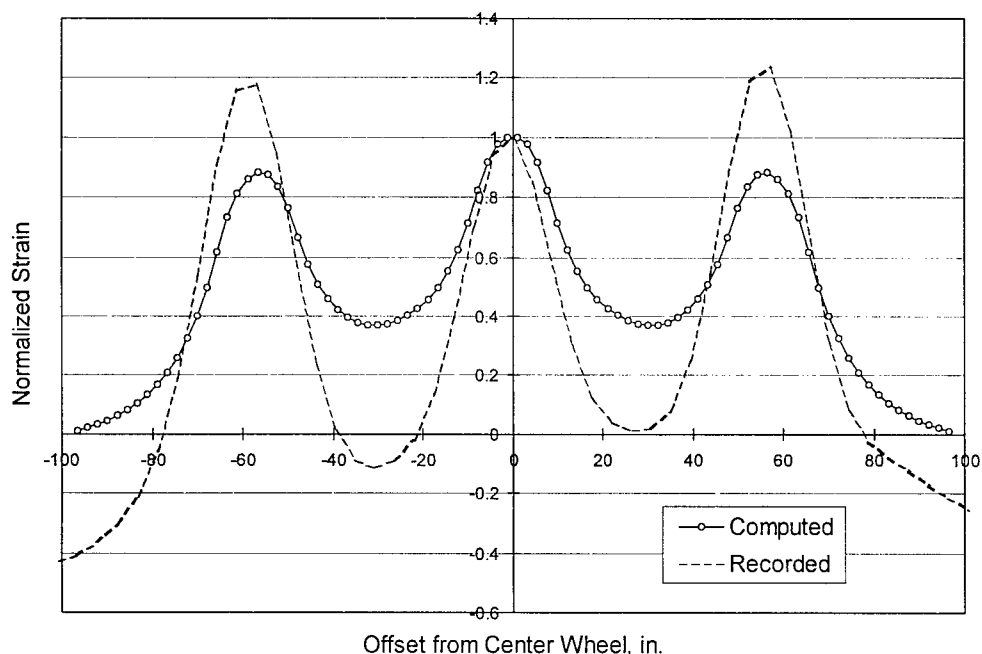


FIGURE 41. DISTRIBUTION OF STRAIN AS COMPUTED BY FINITE ELEMENT MODEL AND AS RECORDED AT STRAIN GAUGE HB08 (B-777 EDGE LOAD)

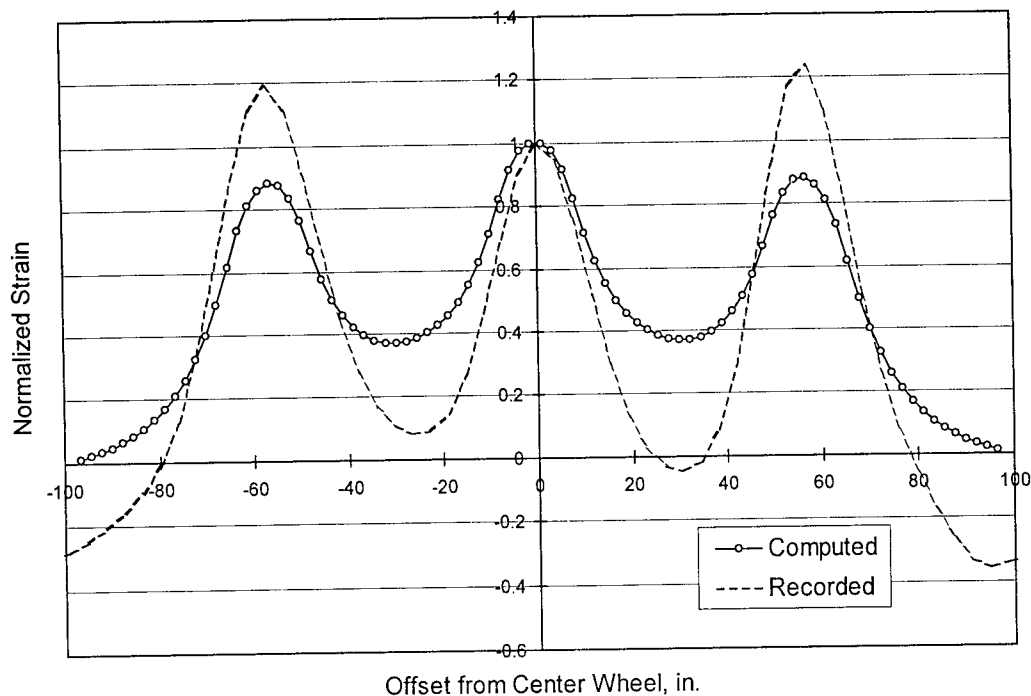


FIGURE 42. DISTRIBUTION OF STRAIN AS COMPUTED BY THREE-DIMENSIONAL FINITE ELEMENT MODEL AND AS RECORDED AT STRAIN GAUGE HB58 (B-777 EDGE LOAD)

similarities and differences between measured and computed distributions of strain may be summarized as follows:

1. Both the finite element model and the recorded data show three distinct strain peaks corresponding to the three wheels in the B-777 tridem.
2. In neither the finite element solution nor the recorded data is there significant strain reversal observed between the peaks.
3. Both strain gauges, HB08 and HB58, indicate that the maximum peak is under the leading wheel in the tridem; whereas, the finite element model predicts the maximum strain under the center wheel.
4. Strain gauges record significant strain reversal before and after the event. This phenomenon is not reproduced by the static finite element model.
5. The finite element model predicts a smaller peak-to-trough ratio than the strain gauge data.

SLAB DEFLECTION COMPARISONS. Slab deflections computed by the finite element method can be compared to measurements of the linear variable differential transformers (LVDT's) installed in the DIA test pavement. The locations of LVDT's are shown in figure 43.

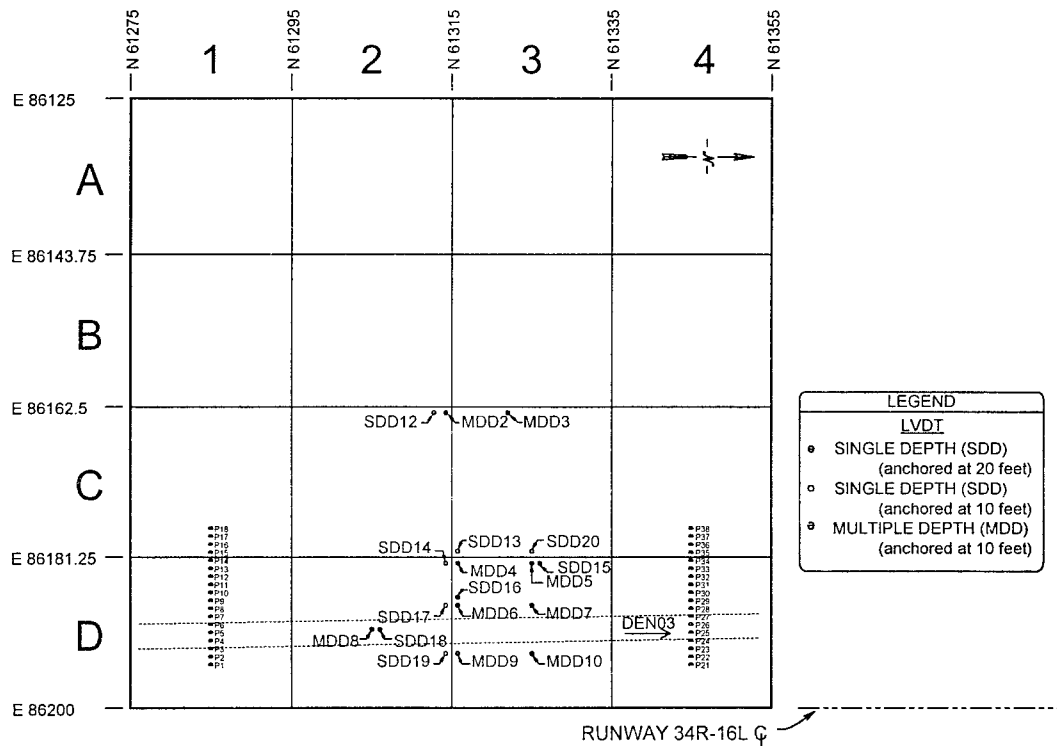


FIGURE 43. SINGLE- AND MULTIPLE-DEPTH DEFLECTOMETER LOCATIONS AT DIA TEST RUNWAY

Two types of gauges are used: single-depth deflectometers (SDD) contain one LVDT located at mid-depth of the PCC slab, and multiple-depth deflectometers (MDD) contain four LVDT's, one of which is located at mid-depth of the PCC slab. Deflection gauges are anchored at either 10 or 20 feet below grade as indicated in figure 43.

Figure 44 shows deflection gauge readings for gauges SDD17 and MDD6 (Gauge 1), located at mid-depth of the PCC slab, on opposite sides of a transverse joint as shown in figure 43. The loading aircraft is a Boeing B-727 (file DEN03) whose track is also shown in figure 43. Since gauges SDD17 and MDD6 are situated on opposite sides of the joint, they can be used to evaluate the in situ performance of the joint. Joint efficiency (i.e., the ratio of deflection of the unloaded slab edge to deflection of the loaded slab edge) is computed from the curves in figure 44 as the ratio of *C* to *A* in the forward direction, or as *B* to *D* in the backward direction. The measurements *C* and *A* are the measured responses of gauge MDD6 on the unloaded slab and gauge SDD17 on the loaded, respectively, at the time before the wheel was moving across the joint. Similarly, the measurements *B* and *D* represent the measured responses after the wheel had gone over the joint.

Table 21 compares the gauge deflections from figure 44 to the equivalent computed slab deflections from the finite element model. Gauge readings for both the loaded and unloaded side of the transverse joint are reported, and the deflection ratio for the transverse joint is computed

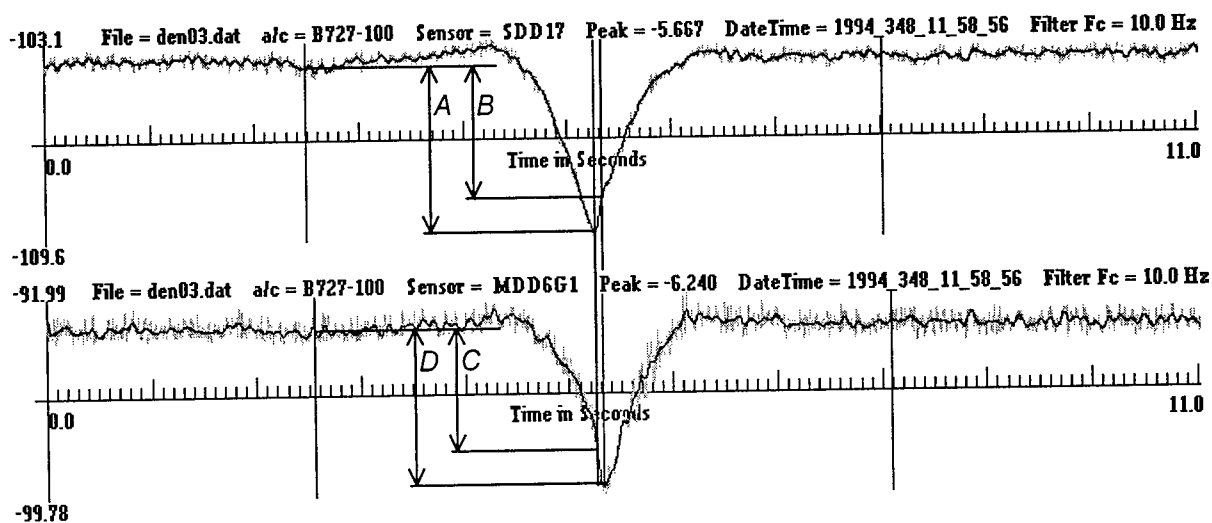


FIGURE 44. DENVER INTERNATIONAL AIRPORT TEST PAVEMENT—RECORDED SLAB DEFLECTIONS ON OPPOSITE SIDES OF A TRANSVERSE JOINT (B-727 LOAD)

TABLE 21. SLAB DEFLECTIONS AS MEASURED BY LVDT GAUGES AND AS PREDICTED BY THE THREE-DIMENSIONAL FINITE ELEMENT MODEL

	Measured (LVDT)		Predicted (3D Finite Element)	
	Forward	Backward	Base Cracked	Base Continuous
Deflection (in.), Loaded Slab	0.00624	0.00567	0.02111	0.01988
Deflection (in.), Unloaded Slab	0.00472	0.00469	0.01991	0.01933
Joint efficiency $\delta_U / \delta_L$	0.76	0.83	0.94	0.97

for both the forward and reverse directions. Computed values of slab deflection are given for both the cracked and uncracked (continuous) base layer under the joint. For both cases (base layer cracked and base layer continuous) the value of joint stiffness used was  $k_{joint} = 100,000$  lbs./in./in. In contrast to the case with strain, where the recorded values were close to the computed values, the computed values of slab deflection are significantly higher than the gauge readings. This discrepancy is possibly explained by the fact that both MDD and SDD displacement gauges are anchored at 10 or 20 feet as noted above. At this depth it is reasonable to assume that there is significant movement of the anchorage, which would have the effect of reducing the recorded deflections below their absolute values. Therefore, the gauge readings should probably be adjusted upward to account for estimated anchorage movement.

#### MODEL VALIDATION WITH FULL-SCALE AIRPORT PAVEMENT TEST MACHINE.

Three-dimensional finite element model predictions will be validated using data from the full-scale airport pavement test machine currently under construction at the William J. Hughes

Technical Center, Atlantic City International Airport, New Jersey. Initially, the test machine will have nine test items of which three will be rigid pavement test items. During the first year of test machine operation, two series of tests will be conducted. Response tests will measure the pavement response to static and moving loads, while traffic tests will measure the number of load repetitions required to cause failure of the test items under controlled conditions. For purposes of finite element model validation, the response tests are of greatest interest. Table 22 lists input data required for each rigid pavement test item constructed for validation of the three-dimensional model.

TABLE 22. AIRPORT PAVEMENT TEST MACHINE INPUT DATA FOR THREE-DIMENSIONAL MODEL VALIDATION

Data Description	Test, Procedure, or Standard
PCC Slab:	
Slab Thickness	Nominal
Young's Modulus $E$	ASTM C-649
Poisson's Ratio $\mu$	Standard value 0.15
Treated Base Layer:	
Layer Thickness	Nominal
Young's Modulus $E$	Core Sample
Poisson's Ratio $\mu$	Core Sample
Unbound Aggregate Base Layer:	
Layer Thickness	Nominal
Young's Modulus $E$	Resilient Modulus Test (AASHTO T-294-94)
Poisson's Ratio $\mu$	Standard Value 0.35
Subgrade	
Young's Modulus $E$	Resilient Modulus Test (AASHTO T-294-94)
Poisson's Ratio $\mu$	Standard value 0.40
Joints (Longitudinal)	
Load Transfer Efficiency (LTE)	Falling Weight Deflectometer
Joints (Transverse)	
Load Transfer Efficiency (LTE)	Falling Weight Deflectometer

The model will be validated by comparing model predictions of strains, deflections, and joint efficiencies with the corresponding measurements from the in-service test item during response tests. Strains will be used for the comparison rather than stresses since strains, unlike stresses, are a directly measured quantity. In order to obtain a valid comparison, the following quantities,

at a minimum, should be recorded by instrumentation in the rigid pavement test items: horizontal strain in the top and bottom of the slab at critical locations, vertical deflection of the center plane of the slab at critical locations, vertical deflection of the top of the base layer at critical locations, and differential movement between adjacent slabs (joint deflections). The critical locations for strain measurement are adjacent to the longitudinal and transverse joints and at the center of loaded slabs. Strain gauges located in the interiors of slabs should be oriented in both principal directions, while a single strain gauge oriented parallel to the joint is sufficient at slab edges. For deflection measurements the critical locations are the slab edges and corners. Where possible, multiple-depth deflectometers (MDD's) should be placed in pairs on opposite sides of a joint, in order to observe the relative slab movement. Joint displacement gauges should also be placed strategically for measurement of differential joint movement.

## SUMMARY AND CONCLUSION

A three-dimensional finite element model for linear elastic, static analysis of rigid airport pavements was developed and implemented. The model has the following features:

1. Multiple slabs of variable dimensions.
2. Multiple elastic layers.
3. Linear elastic joints.
4. Sliding and separation between the PCC slab and base layer.
5. Explicit modeling of individual wheels in multiple-wheel aircraft gears.
6. Edge or interior aircraft loading.
7. Base layer crack modeling under joints.

The finite element model employs a combination of shell and solid elements. Four-node shell elements are used for the PCC slab and eight-node solid elements for other pavement components, including the subgrade. The infinite subgrade is modeled as a discretized solid with a fixed base. An analysis of possible alternatives to this subgrade model was conducted considering boundary element/finite element hybrids, infinite element formulations, and various compliant foundation models. Based on this analysis, it was concluded that the discretized subgrade model was the easiest to implement with available software but that the compliant foundation approach promised considerable execution time savings. The final developed model provides a Winkler Foundation option that allows a spring foundation to be substituted for the default discretized subgrade layer.

Sample numerical computations were performed using the public domain program NIKE3D with a Preconditioned Conjugate Gradient (PCG) linear equation solver. Computations were performed on a SGI Indigo<sup>2</sup> UNIX-based workstation. Typical problem solution times on the workstation were in the range of 1 to 36 hours, depending on the size of the problem and on other factors, including the assumed joint stiffness. A drawback of the NIKE3D program is that in its current version it does not allow spring foundation models to be solved except by the direct (Gaussian) solver, which is more time consuming for large problems.

Three-dimensional finite element meshes were generated by computer using automatic mesh generation software specially developed for that purpose. The automatic mesh generation program incorporates the public-domain program INGRID as a meshing engine. Using the mesh generation program, finite element meshes for NIKE3D can be produced rapidly for any combination of rigid pavement properties and aircraft loadings. Aircraft gear properties may be taken from an existing library of standard gears and modified as required.

A sensitivity analysis was conducted to identify variables affecting the model response and to refine the mesh. Some of the conclusions of the sensitivity analysis are as follows:

1. A mesh density of approximately 2 by 2 inches for shell elements in the load region is sufficient for the desired accuracy.
2. A discretized subgrade cutoff depth of 1,140 inches is sufficient to simulate the infinite subgrade condition. A smaller cutoff depth may be justifiable for some load types. A smaller cutoff depth is desirable since fewer elements translate into shorter run times. The minimum cutoff depth is not significantly affected whether by the load case is interior or edge loading.
3. The computed load transfer is affected by a number of input variables including aircraft gear geometry, elastic joint stiffness, the presence or absence of a high-stiffness base layer, and the presence or absence of a crack in the base layer at the joint location. The percentage of load transfer is not significantly affected by the load magnitude when load magnitude is considered independently of the wheel geometry.
4. Computed load transfer for multiple-wheel gears was higher than for single-wheel gears. For the B-777 gear, the computed load transfer was higher than the 25 percent assumed by the FAA standard.
5. A high-stiffness base layer has the effect of making the critical stress response less sensitive to changes in the joint stiffness.
6. Introducing a crack in the base layer under the joint, in addition to increasing the critical response, may influence the distribution of stress in the PCC slab.

Numerical solutions obtained using the three-dimensional finite element model were compared to other solutions found using the Westergaard-based FAA design method and the LEDFAA method (layered elastic analysis). Comparisons were made for various load types and bases. The point of comparison in all cases was the maximum tensile stress in the bottom of the PCC slab. The finite element solutions were found to be in reasonable agreement with the standard methods for the cases studied. In most cases, the critical edge stress predicted by the three-dimensional finite element model was less than the corresponding FAA edge stress when a linear elastic joint stiffness of 100,000 lbs./in. per linear inch of joint was assumed for the finite element model. Comparisons were also made between the finite element model and gauge readings from the DIA instrumented runway project. Peak strains, strain distributions, and slab deflections due to aircraft loading were compared. Peak values of strain recorded at several gauges were found to



be within the range of strains predicted by the three-dimensional finite element model for the DIA runway properties and loadings.

It is expected that additional validation of the model performance will come from the National Airport Pavement Test Machine currently under construction at the William J. Hughes Technical Center.

In conclusion, the three-dimensional finite element method provides a practical method of computing rigid pavement stresses due to aircraft loading, taking into account such factors as multiple-wheel interaction, finite slab size, multiple-layer construction, and variable joint stiffness.

## REFERENCES

1. Parker, F., Jr., Barker, W.R., Gunkel, R.C., and Odom, E.C., "Development of a Structural Design Procedure for Rigid Airport Pavements," Federal Aviation Administration Report No. FAA-RD-77-81 and WES Report No. WES TR-GL-79-4, U.S. Army Engineer Waterways Experiment Station, Vicksburg, Mississippi, April 1979.
2. Maker, B.M., "NIKE3D - A Nonlinear, Implicit, Three-Dimensional Finite Element Code for Solid and Structural Mechanics - User's Manual," Report No. UCRL-MA-105268 Rev. 1, Lawrence Livermore National Laboratory, Livermore, California, April 1995.
3. Christon, M.A. and Dovey, D., "INGRID—A 3D Mesh Generator for Modeling Nonlinear Systems," Report No. UCRL-MA-109790 (Draft), Lawrence Livermore National Laboratory, Livermore, California, September 1992.
4. Balas, J., Sládek, J., and Sládek, V., Stress Analysis by Boundary Element Methods, translation of Analýza napětí metodou hranicných integrálních rovnic, Elsevier, Amsterdam and New York, 1989.
5. Golub, G.H. and Van Loan, C.F., Matrix Computations, second edition, The Johns Hopkins University Press, Baltimore, Maryland, 1989.
6. Atkinson, K.E., An Introduction to Numerical Analysis, second edition, Wiley, New York, 1989.
7. Hughes, T.J.R. and Belytschko, T., Course Notes for Nonlinear Finite Element Analysis, July 18-22, 1994, Palo Alto, California.
8. U.S. Department of Transportation, Federal Aviation Administration, "Airport Pavement Design for the Boeing 777 Airplane," Advisory Circular 150/5320-16, 1995.
9. Portland Cement Association, Design of Concrete Airport Pavement, 1955.
10. Huang, Y.H., Pavement Analysis and Design, Prentice-Hall, Englewood Cliffs, New Jersey, 1993.

11. Tielking, J.T., "Aircraft Tire/Pavement Pressure Distributions in Aircraft Landing Gear Systems," J.A. Tanner, editor, Society of Automotive Engineers, Warrendale, Pennsylvania, 1990.
12. U.S. Department of Transportation, Federal Aviation Administration, "Airport Pavement Design and Evaluation," Advisory Circular 150/5320-6D, 1995.
13. Pickett, G. and Ray, G.K., "Influence Charts for Rigid Pavements," ASCE Transactions, 1951.

# APPENDIX A—SUMMARY OF TEST RUN DATA

## TABLE A-1. INPUT DATA AND RUN TIMES

No.	Load			Pavement			No. of Linear Equations	Run Time, hrs.	Notes
	Aircraft	Weight, lbs.·10 <sup>3</sup>	Load Case	Prop. Group	Cutoff Depth, in.	$k_{joint}$ , lbs./in/in			
1	SWL	30	Int.	A	300	100,000	21,614	0.8	
2	SWL	30	Int.	A	420	100,000	22,174	0.9	
3	B-777	680	Edge	B	2220	100,000	104,609	8.5	
4	SWL	30	Int.	A	780	100,000	23,854	1.0	
5	SWL	30	Int.	A	1140	100,000	25,534	1.1	
6	SWL	30	Int.	B	300	100,000	21,614	1.0	
7	SWL	30	Int.	B	420	100,000	22,174	1.6	
8	SWL	30	Int.	B	780	100,000	23,854	2.3	
9	B-777	680	Edge	B	300	100,000	71,457	6.5	
10	SWL	30	Int.	B	1140	100,000	25,534	2.7	
11	B-777	680	Int.	A	300	100,000	27,716	1.4	
12	B-777	680	Int.	A	420	100,000	28,276	1.5	
13	SWL	30	Int.	A	1140	100,000	23,218	0.5	1
14	B-777	680	Edge	B	420	100,000	73,529	7.1	
15	B-777	680	Int.	A	780	100,000	29,956	1.9	
16	B-777	680	Int.	A	1140	100,000	31,636	1.7	
17	B-777	680	Int.	A	1500	100,000	33,316	1.8	
18	SWL	30	Int.	A	1140	100,000	24,115	0.9	2
19	B-777	680	Edge	B	780	100,000	79,745	8.4	
20	SWL	30	Int.	A	1140	100,000	27,243	1.3	3
21	B-777	680	Int.	B	1500	100,000	33,316	3.4	
22	B-777	680	Int.	C	-	100,000	15,868	0.6	4
23	B-777	680	Int.	D	-	100,000	15,868	1.1	4
24	B-777	680	Edge	B	1140	100,000	85,961	9.4	
25	SWL	30	Int.	D	-	100,000	9,766	0.3	4
26	SWL	30	Int.	C	-	100,000	9,766	0.2	4
27	B-777	680	Edge	A	1500	100,000	92,177	18.6	
28	B-777	680	Edge	B	1500	100,000	92,177	6.9	5
29	B-777	680	Int.	B	1500	100,000	33,316	3.4	5
30	B-777	680	Edge	B	1500	100,000	92,177	9.5	
31	SWL	30	Edge	B	1500	100,000	81,489	11.8	
32	SWL	680	Edge	B	1500	100,000	81,849	12.8	6
33	B-777	680	Edge	B	1500	1,000	92,177	77.8	7
34	B-777	680	Edge	B	1500	10,000	92,177	36.9	
35	B-777	680	Edge	B	1500	50,000	92,177	15.9	
36	B-777	680	Edge	B	1500	200,000	92,177	7.1	

TABLE A-1. INPUT DATA AND RUN TIMES (CONTINUED)

No.	Load			Pavement			No. of Linear Equations	Run Time, hrs.	Notes
	Aircraft	Weight, lbs.·10 <sup>3</sup>	Load Case	Prop. Group	Cutoff Depth, in.	$k_{joints}$ lbs./in/in			
37	B-777	680	Edge	B	1500	75,000	92,177	10.8	
38	B-777	680	Edge	B	1500	10,000	92,458	23.3	8
39	B-777	680	Edge	B	1500	100,000	92,458	9.4	8
40	B-777	680	Int.	E	300	100,000	27,716	3.4	
41	B-777	680	Int.	E	420	100,000	28,276	4.8	
42	B-777	680	Edge	B	1500	50,000	92,458	10.8	8
43	B-777	680	Edge	B	1500	200,000	92,458	9.5	8
44	B-777	680	Int.	E	780	100,000	29,956	5.6	
45	B-777	680	Edge	A	1500	50,000	92,177	35.0	
46	B-777	680	Int.	E	1500	100,000	33,316	6.6	
47	B-777	680	Edge	A	1500	10,000	92,177	32.3	
48	B-777	680	Edge	A	1500	200,000	92,177	11.0	
49	B-727	172	Edge	B	1500	100,000	83,301	6.8	
50	B-727	172	Edge	A	1500	100,000	83,301	9.2	
51	B-777	680	Int.	E	1140	100,000	31,636	6.1	
52	SWL	30	Int.	A	1500	100,000	27,214	1.1	
53	SWL	30	Int.	B	1500	100,000	27,214	2.9	
54	B-777	680	Edge	B	1860	100,000	98,393	8.0	
55	SWL	30	Int.	B	1860	100,000	28,994	2.4	
56	B-777	680	Int.	A	1860	100,000	34,996	1.9	
57	B-777	680	Edge	E	1500	100,000	92,177	17.6	
58	B-777	680	Int.	E	1860	100,000	34,996	6.9	
59	B-777	680	Int.	F	2220	100,000	36,676	6.2	
60	B-777	680	Int.	E	2220	100,000	36,676	7.2	
61	B-777	680	Int.	G	-	100,000	15,868	1.1	4
62	B-777	680	Int.	E	2580	100,000	38,356	7.5	
63	B-777	680	Edge	B	300	100,000	71,457	68.1	9
64	B-727	136.5	Edge	H	1500	100,000	95,277	10.3	10,11
65	B-727	136.5	Edge	H	1500	10,000	95,277	10.9	10,11
66	B-727	136.5	Edge	H	1500	50,000	95,277	10.6	10,11
67	B-727	136.5	Edge	H	1500	200,000	95,277	10.4	10,11
68	B-727	136.5	Edge	H	1500	100,000	98,167	16.6	8,10,11
69	B-727	136.5	Edge	H	1500	10,000	98,167	26.6	8,10,11
70	B-727	136.5	Edge	H	1500	50,000	98,167	15.3	8,10,11
71	B-727	136.5	Edge	H	1500	200,000	98,167	13.3	8,10,11
72	B-727	136.5	Int.	I	1500	100,000	34,279	3.7	10
73	B-777	371.4	Edge	I	1140	100,000	106,698	19.0	10,11,12
74	B-777	371.4	Edge	I	1140	100,000	106,545	17.2	10,11

TABLE A-1. INPUT DATA AND RUN TIMES (CONTINUED)

No.	Load			Pavement			No. of Linear Equations	Run Time, hrs.	Notes
	Aircraft	Weight, lbs.·10 <sup>3</sup>	Load Case	Prop. Group	Cutoff Depth, in.	$k_{joint}$ , lbs./in/in			
75	B-777	371.4	Edge	I	1140	100,000	107,062	16.2	8,10,11
76	B-777	428.4	Edge	I	1500	100,000	100,041	17.5	2,10
77	B-777	428.4	Edge	I	1500	100,000	100,558	15.9	2,8,10
78	B-777	428.4	Edge	I	1500	100,000	100,041	16.7	2,10,13

TABLE A-2. SUMMARY OF COMPUTED RESPONSES

No.	Maximum Bending Stress, Bottom of PCC Slab (psi)				Slab Deflection (in.)	
	Loaded Slab		Unloaded Slab		Loaded Slab	Unloaded Slab
	IP	MR	IP	MR		
1	96.875	96.610	N.A.	N.A.	0.00555	N.A.
2	97.093	96.824	N.A.	N.A.	0.00587	N.A.
3	424.666	429.791	243.937	237.652	0.17043	0.16828
4	97.203	96.935	N.A.	N.A.	0.00628	N.A.
5	97.218	96.950	N.A.	N.A.	0.00643	N.A.
6	93.309	93.020	N.A.	N.A.	0.00527	N.A.
7	93.535	93.252	N.A.	N.A.	0.00560	N.A.
8	93.654	93.374	N.A.	N.A.	0.00601	N.A.
9	423.181	428.657	223.655	216.334	0.08921	0.08614
10	93.664	93.386	N.A.	N.A.	0.00616	N.A.
11	508.505	507.983	N.A.	N.A.	0.08357	N.A.
12	512.829	512.276	N.A.	N.A.	0.09055	N.A.
13	94.450	93.477	N.A.	N.A.	0.00642	N.A.
14	426.553	432.071	228.057	220.861	0.09656	0.09352
15	515.179	514.663	N.A.	N.A.	0.09958	N.A.
16	515.579	515.029	N.A.	N.A.	0.10310	N.A.
17	515.679	515.097	N.A.	N.A.	0.10498	N.A.
18	95.906	95.431	N.A.	N.A.	0.00642	N.A.
19	428.476	434.015	230.709	223.590	0.10573	0.10272
20	97.596	97.435	N.A.	N.A.	0.00642	N.A.
21	493.640	492.815	N.A.	N.A.	0.10019	N.A.
22	537.258	536.575	N.A.	N.A.	0.07606	N.A.
23	515.703	514.823	N.A.	N.A.	0.07130	N.A.
24	428.625	434.237	230.909	223.959	0.10922	0.10620
25	97.587	97.310	N.A.	N.A.	0.00507	N.A.
26	100.827	100.568	N.A.	N.A.	0.00534	N.A.
27	451.312	459.977	244.685	234.574	0.12153	0.11556
IP = computed directly at Lobatto integration points    MR = computed from moment resultants						

TABLE A-2. SUMMARY OF COMPUTED RESPONSES (CONTINUED)

No.	Maximum Bending Stress, Bottom of PCC Slab (psi)				Slab Deflection (in.)	
	Loaded Slab		Unloaded Slab		Loaded Slab	Unloaded Slab
	IP	MR	IP	MR		
28	422.345	427.251	239.422	233.014	0.11076	0.10811
29	493.616	492.814	N.A.	N.A.	0.10010	N.A.
30	428.725	434.317	231.009	224.025	0.11108	0.10807
31	114.751	116.037	45.575	44.132	0.00843	0.00756
32	2603.944	2631.965	1026.569	997.229	0.19113	0.17125
33	*	*	*	*	*	*
34	445.573	445.539	199.668	197.910	0.11352	0.10253
35	435.474	438.897	218.594	213.597	0.11175	0.10617
36	412.167	420.869	250.360	240.654	0.11055	0.10851
37	434.819	439.223	223.301	217.403	0.11135	0.10576
38	473.655	480.155	194.475	191.821	0.11854	0.10111
39	400.524	455.520	226.412	220.773	0.11331	0.10846
40	635.110	634.123	N.A.	N.A.	0.16123	N.A.
41	644.660	643.649	N.A.	N.A.	0.18139	N.A.
42	405.895	460.145	208.779	202.375	0.11490	0.10690
43	394.390	448.667	238.531	232.797	0.11240	0.10942
44	651.160	650.127	N.A.	N.A.	0.20922	N.A.
45	462.144	469.948	231.855	224.422	0.12356	0.11342
46	652.360	651.227	N.A.	N.A.	0.22622	N.A.
47	509.751	514.379	182.847	180.704	0.13264	0.10166
48	441.274	454.754	256.024	240.119	0.12041	0.11704
49	400.651	405.199	188.204	181.958	0.03860	0.03584
50	434.684	440.355	187.364	178.593	0.04266	0.03830
51	652.110	651.065	N.A.	N.A.	0.22024	N.A.
52	97.218	96.953	N.A.	N.A.	0.00652	N.A.
53	93.674	93.392	N.A.	N.A.	0.00624	N.A.
54	422.195	427.101	239.423	233.037	0.11202	0.10937
55	93.648	93.362	N.A.	N.A.	0.00628	N.A.
56	515.679	515.125	N.A.	N.A.	0.10617	N.A.
57	598.184	604.935	435.007	428.217	0.26883	0.26571
58	652.410	651.369	N.A.	N.A.	0.23006	N.A.
59	610.316	609.627	N.A.	N.A.	0.22201	N.A.
60	652.460	651.393	N.A.	N.A.	0.23277	N.A.
61	589.110	588.612	N.A.	N.A.	0.11269	N.A.
62	652.460	651.393	N.A.	N.A.	0.23478	N.A.
63	424.375	430.980	218.079	213.436	0.09011	0.08577
64	177.146	177.161	105.668	104.947	0.02283	0.02217
IP = computed directly at Lobatto integration points    MR = computed from moment resultants						

TABLE A-2. SUMMARY OF COMPUTED RESPONSES (CONTINUED)

No.	Maximum Bending Stress, Bottom of PCC Slab (psi)				Slab Deflection (in.)	
	Loaded Slab		Unloaded Slab		Loaded Slab	Unloaded Slab
	IP	MR	IP	MR		
65	180.172	179.051	103.078	103.183	0.02294	0.02202
66	178.655	178.112	104.373	104.098	0.02288	0.02210
67	174.990	175.805	107.261	106.125	0.02277	0.02227
68	197.978	204.980	88.999	86.653	0.02451	0.02251
69	213.467	218.336	68.646	67.863	0.02567	0.02112
70	200.392	209.963	81.669	79.685	0.02489	0.02210
71	200.053	199.312	96.104	94.498	0.02407	0.02282
72	186.905	187.082	N.A.	N.A.	0.01876	N.A.
73	215.106	215.788	115.575	111.803	0.04093	0.04014
74	215.979	216.905	115.674	111.602	0.04304	0.04024
75	212.436	240.199	103.130	100.232	0.04170	0.03991
76	213.647	215.717	121.141	120.705	0.05515	0.05396
77	199.726	242.330	112.582	108.925	0.05666	0.05399
78	211.971	217.423	121.322	120.932	0.05514	0.05397
IP = computed directly at Lobatto integration points    MR = computed from moment resultants						

Notes:

1. Minimum side length for 2D slab elements: 4.167 inches.
2. Minimum side length for 2D slab elements: 2.778 inches.
3. Minimum side length for 2D slab elements: 1.667 inches.
4. Winkler base (Direct solution method used).
5. Slab edge rotational degrees of freedom constrained.
6. Load patch dimensions same as No. 31 (Single-Wheel Load).
7. Failed to converge after 30 calls to conjugate gradients – aborted.
8. Base layer cracked under joint.
9. Similar to No. 9, except that the joint gap width  $\delta$  was reduced from 1.0 to 0.1 inch.
10. Model of DIA test runway.
11. Aircraft gear oriented perpendicular to joint.
12. Longitudinal and transverse slab dimensions reversed.
13. PCG with Gauss-Seidel EBE method.

Layer Property Groups for Test Runs:

- A. 14-in. PCC Slab ( $E = 4,000,000$  psi,  $\mu = 0.15$ )  
 No Base  
 Infinite Subgrade ( $E = 15,000$  psi,  $\mu = 0.40$ )

- B. 14-in. PCC Slab ( $E = 4,000,000$  psi,  $\mu = 0.15$ )  
8-in. Stabilized Base ( $E = 500,000$  psi,  $\mu = 0.20$ )  
Infinite Subgrade ( $E = 15,000$  psi,  $\mu = 0.40$ )
- C. 14-in. PCC Slab ( $E = 4,000,000$  psi,  $\mu = 0.15$ )  
No Base  
Infinite Subgrade ( $k = 141.4$  pci)
- D. 14-in. PCC Slab ( $E = 4,000,000$  psi,  $\mu = 0.15$ )  
8-in. Stabilized Base ( $E = 500,000$  psi,  $\mu = 0.20$ )  
Infinite Subgrade ( $k = 141.4$  pci)
- E. 16-in. PCC Slab ( $E = 4,000,000$  psi,  $\mu = 0.15$ )  
8-in. Stabilized Base ( $E = 500,000$  psi,  $\mu = 0.20$ )  
Infinite Subgrade ( $E = 4,500$  psi,  $\mu = 0.40$ )
- F. 17-in. PCC Slab ( $E = 4,000,000$  psi,  $\mu = 0.15$ )  
8-in. Stabilized Base ( $E = 500,000$  psi,  $\mu = 0.20$ )  
Infinite Subgrade ( $E = 4,500$  psi,  $\mu = 0.40$ )
- G. 16-in. PCC Slab ( $E = 4,000,000$  psi,  $\mu = 0.15$ )  
8-in. Stabilized Base ( $E = 500,000$  psi,  $\mu = 0.20$ )  
Infinite Subgrade ( $k = 55.4$  pci)
- H. 17.3-in. PCC Slab ( $E = 4,410,000$  psi,  $\mu = 0.22$ )  
Slab Dimensions: 20 ft. (long.) by 18.75 ft. (trans.)  
8-in. Cement-Treated Base ( $E = 1,200,000$  psi,  $\mu = 0.20$ )  
12-in. Lime-Stabilized Subbase ( $E = 440,000$  psi,  $\mu = 0.25$ )  
Infinite Subgrade ( $E = 15,000$  psi,  $\mu = 0.40$ )  
(DIA Test Runway Section)
- I. 17.8-in. PCC Slab ( $E = 4,410,000$  psi,  $\mu = 0.22$ )  
Slab Dimensions: 20 ft. (long.) by 18.75 ft. (trans.)  
8-in. Cement-Treated Base ( $E = 1,200,000$  psi,  $\mu = 0.20$ )  
12-in. Lime-Stabilized Subbase ( $E = 440,000$  psi,  $\mu = 0.25$ )  
Infinite Subgrade ( $E = 15,000$  psi,  $\mu = 0.40$ )  
(DIA Test Runway Section)



# APPENDIX B—FORMULAS FOR LOBATTO INTEGRATION

Lobatto's formula for numerical integration is

$$\int_{-1}^{+1} f(x) dx \approx w_1 f(-1) + \sum_{i=2}^{n-1} w_i f(x_i) + w_n f(1)$$

where the numerical values of abscissas  $x_i$  and weights  $w_i$  for various  $n$  are given in the table below.

TABLE B-1. ABSCISSAS AND WEIGHTS FOR LOBATTO INTEGRATION

$n$	$\pm x_i$	$w_i$
3	1.00000 000	0.33333 333
	0.00000 000	1.33333 333
4	1.00000 000	0.16666 667
	0.44721 360	0.83333 333
5	1.00000 000	0.10000 000
	0.65465 367	0.54444 444
	0.00000 000	0.71111 111
6	1.00000 000	0.06666 667
	0.76505 532	0.37847 496
	0.28523 152	0.55485 838
7	1.00000 000	0.04761 904
	0.83022 390	0.27682 604
	0.46884 879	0.43174 538
	0.00000 000	0.48761 904



## APPENDIX C—CONSTANTS FOR NIKE3D MATERIAL TYPE 17

NIKE3D Material Type 17 (Foundation Boundary Spring) is defined by the following 6 x 6 symmetric matrix of spring constants [2]

$$\mathbf{K} = \begin{bmatrix} K_{11} & K_{12} & K_{13} & K_{14} & K_{15} & K_{16} \\ & K_{22} & K_{23} & K_{24} & K_{25} & K_{26} \\ & & K_{33} & K_{34} & K_{35} & K_{36} \\ & & & K_{44} & K_{45} & K_{46} \\ & & & & K_{55} & K_{56} \\ & & & & & K_{66} \end{bmatrix}$$

The constants  $K_{ij}$  relate nodal forces and moments  $\mathbf{F}$  to nodal displacements and rotations  $\mathbf{x}$

$$\mathbf{F} = \mathbf{kx}$$

$$\mathbf{F} = \begin{bmatrix} f_x & f_y & f_z & m_x & m_y & m_z \end{bmatrix}^T$$

$$\mathbf{x} = \begin{bmatrix} u_x & u_y & u_z & \theta_x & \theta_y & \theta_z \end{bmatrix}^T$$

In the current model of the Winkler foundation, all constants  $K_{ij}$  are set equal to zero except

$$K_{33} = k A_{trib}$$

where  $k$  is the modulus of subgrade reaction and  $A_{trib}$  is the tributary area for the foundation node.



## APPENDIX D—NIKE3D CONTROL CARD SETTINGS

NIKE3D execution is controlled by ten control cards, which appear as the first ten executable lines in the NIKE3D input file. The control deck structure is discussed in reference 2. The first five cards contain information about the specific mesh being analyzed (e.g., number of nodes, number of slide surfaces to be defined) and about the load (number of load curves, etc.). Cards 5 through 10 contain data governing the finite element analysis. The control card entries for control cards 5–10 used in the three-dimensional finite element analysis are listed below. Control card fields not listed are assigned the NIKE3D default values (indicated by a zero entry in the field). The default values are given in reference 2.

### CARD 5

Output Printing Interval	1
--------------------------	---

### CARD 6

Nonlinear Equilibrium Solution Method (BFGS)	1
Bandwidth Minimization Flag	3

### CARD 7

(All default settings)

### CARD 8

Element data buffer size (bytes)	30000000
Direct linear equation solver (FISSLE)	1
BFGS update vector storage option	1
Brick element formulation (B-Bar)	1
Shell element formulation (Hughes-Liu)	1

### CARD 9

Number of user-specified integration rules for shells	1
Maximum number of user-specified integration points	5

### CARD 10

Linear equation solver option (default – PCG)	1
(For Winkler Foundation option)	0
Iteration limit for linear solver	9999
Iterative solver data storage option (in-core storage)	1

